2018

MORPHOLOGICAL AND ENERGETIC EFFECTS ON CHARGE TRANSPORT IN CONJUGATED POLYMERS AND POLYMER-NANOWIRE COMPOSITES

Zhiming Liang
University of Kentucky, leungchiminh@gmail.com

Digital Object Identifier: https://doi.org/10.13023/etd.2018.254

Recommended Citation

Liang, Zhiming, "MORPHOLOGICAL AND ENERGETIC EFFECTS ON CHARGE TRANSPORT IN CONJUGATED POLYMERS AND POLYMER-NANOWIRE COMPOSITES" (2018). *Theses and Dissertations--Chemistry*. 99.
https://uknowledge.uky.edu/chemistry_etds/99

STUDENT AGREEMENT:

I represent that my thesis or dissertation and abstract are my original work. Proper attribution has been given to all outside sources. I understand that I am solely responsible for obtaining any needed copyright permissions. I have obtained needed written permission statement(s) from the owner(s) of each third-party copyrighted matter to be included in my work, allowing electronic distribution (if such use is not permitted by the fair use doctrine) which will be submitted to UKnowledge as Additional File.

I hereby grant to The University of Kentucky and its agents the irrevocable, non-exclusive, and royalty-free license to archive and make accessible my work in whole or in part in all forms of media, now or hereafter known. I agree that the document mentioned above may be made available immediately for worldwide access unless an embargo applies.

I retain all other ownership rights to the copyright of my work. I also retain the right to use in future works (such as articles or books) all or part of my work. I understand that I am free to register the copyright to my work.

REVIEW, APPROVAL AND ACCEPTANCE

The document mentioned above has been reviewed and accepted by the student’s advisor, on behalf of the advisory committee, and by the Director of Graduate Studies (DGS), on behalf of the program; we verify that this is the final, approved version of the student’s thesis including all changes required by the advisory committee. The undersigned agree to abide by the statements above.

Zhiming Liang, Student

Dr. Kenneth R. Graham, Major Professor

Dr. Mark A. Lovell, Director of Graduate Studies

MORPHOLOGICAL AND ENERGETIC EFFECTS ON CHARGE TRANSPORT IN CONJUGATED POLYMERS AND POLYMER-NANOWIRE COMPOSITES

DISSERTATION

A dissertation submitted in partial fulfillment of the requirements for
the degree of Doctor of Philosophy in the College of Arts and Sciences
at the University of Kentucky

By
Zhiming Liang
Lexington, Kentucky

Director: Dr. Kenneth R. Graham, Professor of Chemistry

Lexington, Kentucky

2018

ABSTRACT OF DISSERTATION

MORPHOLOGICAL AND ENERGETIC EFFECTS ON CHARGE TRANSPORT IN CONJUGATED POLYMERS AND POLYMER-NANOWIRE COMPOSITES

Organic semiconductors have wide applications in organic-based light-emitting diodes, field-effect transistors, and thermoelectrics due to the easily modified electrical and optical properties, excellent mechanical flexibility, and solution processability. To fabricate high performance devices, it is important to understand charge transport mechanisms, which are mainly affected by material energetics and material morphology. Currently it is difficult to control the charge transport properties of new organic semiconductors and organic-inorganic nanocomposites due to our incomplete understanding of the large number of influential variables. Molecular doping of π-conjugated polymers and surface modification of nanowires are two means through which charge transport can be manipulated. In molecular doping, both the energetics and microstructures of polymer films can be changed by controlling the degree of oxidation of the conjugated polymer backbone. For surface modification of inorganic nanowires, the energetics and morphology can be influenced by the properties of the surface modifiers. Meanwhile, the energy band alignment, which can be controlled by surface modification and molecular doping, may also alter the charge transport due to the variation in energetic barriers between the transport states in the organic and inorganic components.

To reveal the effects of morphology and energetics on charge transport in conjugated polymers and organic-inorganic nanocomposites, the influence of surface modifier on the electrical and morphological properties of nanocomposites was first probed. Silver nanowires modified with different thiols were blended with poly (3,4-ethylenedioxythiophene)-poly(styrenesulfonate)(PEDOT:PSS) to fabricate thin films.

The modified nanowires provided a means of controllably altering the nanowire dispersability and compatibility with solvents and polymers. The results also demonstrated that charge transport between the nanowires was facilitated due to low wire-to-wire junction resistance. To further figure out the charge transport mechanism in organic-inorganic nanocomposites and the potential applications, tellurium nanowires and ferric chloride doped poly (3-hexylthiophene-2,5-diyl)(P3HT) were used to characterize energy band alignment effects on charge transport, electrical conductivity, and thermoelectric properties. The results showed that charge transfer between nanowires can be mediated by the polymer and may potentially increase the electrical conductivity as compared to the pure polymer or pure nanowires; while the observed enhancement of power factor (equal to electrical conductivity times the square of Seebeck coefficient) may not be affected by the energy band alignment. It is important to investigate the change of polymer morphology caused by molecular doping and processing method to determine how the morphology will influence the electrical and thermoelectric properties. Various p-type dopants, including ferric chloride and molybdenum tris(1,2-bis(trifluoromethyl)ethane-1,2-dithiolene) (Motfd$_3$), were examined for us in P3HT and other polymers. The results showed that: i) At light doping levels, the electrical conductivity and power factor of polymers doped with the large electron affinity (EA) dopants were larger than small EA dopants; ii) At heavy doping levels, the large size dopants cannot effectively dope polymers even for the dopants with large EAs; iii) For the same dopant, as the IE of the polymer increased, the doping efficiency gradually decreased.

KEYWORDS: Polymer-nanowire composite, Surface modification, Energy filtering, Conducting polymers, Photoelectron spectroscopy, Thermoelectric.

Zhiming Liang
Author's Signature

June 30, 2018
Date

MORPHOLOGICAL AND ENERGETIC EFFECTS ON CHARGE TRANSPORT IN CONJUGATED POLYMERS AND POLYMER-NANOWIRE COMPOSITES

By

Zhiming Liang

Dr. Kenneth R. Graham

Director of Dissertation

Dr. Mark A. Lovell

Director of Graduate Studies

June 30, 2018

Date

Dedicated to my families

ACKNOWLEDGMENTS

Thanks my advisor Prof. Kenneth R. Graham for offering me the opportunity to work in his lab and give the effective instruction to my projects. He was always willing and ready to help me out when I was in trouble. He also spent lots of time to help revise this dissertation. Thanks to my committee members: Prof. John Selegue, Prof. Yinan Wei, and Prof. Yang-Tse Cheng for problems discussion, courses advice, careers suggestion and serving as my committee. Thanks my lab-mates and friends for experiment help and useful discussion (Especially for the thermoelectric setup help from Kamal, and theory discussion from Tairan Wang) (Dr. Karmal Butrouna, Tairan wang, Alex Boehm, Somin park, Ashkan Abtahi, and, Thuy Nguyen, Tuo Liu, Dr. Zhaoshuai Wang, Dr. Mathias J. Boland, Dr. Yan Zhang, Yuchen Zhang, Wenjing Cao, Dr. Ruixin Zhou, Maryam Souri, Dr. Aman Preet Kaur and Dr. Rupam Sarma).

Thanks to the collaborative laboratories that either provided or characterized our samples:

Prof. Seth Marder's group (Georgia Institute of Technology), Prof. Jianguo Mei's group (Purdue University), Prof. Ambrose Seo's group (University of Kentucky), Prof. Doo Young Kim's group (University of Kentucky), Dr. Ruipeng Li (Brookhaven National Laboratory), and Prof. Douglas R. Strachan's group (University of Kentucky)

I also thank Prof. Qiu Wei for serving as the outside examiner.

TABLE OF CONTENTS

LIST OF TABLES

LIST OF FIGURES

Chapter 1: Introduction

Energy scarcity and environmental pollution are two worldwide problems that humans must solve in the near future.[1,2] Traditional fossil fuels like oil and natural gas cannot meet our growing needs.[3] Meanwhile, these non-renewable fuels produce greenhouse gases and pollutants.[4] To deal with this potential crisis, governments are making efforts to develop renewable energy (e.g. Industry 4.0 of Germany,[5] Made in China 2025,[6] and Smart Grid of USA[7]). Currently, the contribution of renewable clean energy such as solar energy, wind, geothermal heat, and hydropower utilized in generating electricity, cooling, and heating is much lower than fossil fuels.[8] Photovoltaics and thermoelectrics, two of the renewable energy sources with a lot of potential, attract researchers' attention to the tremendous waste heat sources (e.g. more than half of the energy used in word is wasted as heat) or solar energy reserves (e.g. around 174 petawatts solar energy radiate to earth and 3,850,000 EJ is absorbed every year).[9] One of the biggest challenges to widely use solar and waste heat energy is the low conversion efficiency of the devices combined with the relatively high cost.[10] To improve device performance, researchers need to explore the mechanisms of charge transport in materials[11] (e.g., the influence of molecular structure and morphology on carrier concentration, mobility, and electrical conductivity), and synthesize new materials with high carrier mobility, high mechanical flexibility, high electrical conductivity, and high Seebeck coefficients.

This dissertation is mainly focused on understanding charge transport in organic-inorganic nanocomposites (e.g., silver and tellurium nanowires), and organic semiconductors (e.g., diketopyrrolopyrrole (DPP) derivatives, poly (3-hexylthiophene-2,5-diyl)(P3HT), and Poly(3,4-ethylenedioxythiophene)-poly (styrenesulfonate)(PEDOT:PSS)). Surface modification and molecular doping are two means through which charge transport can be manipulated in nanowires and conjugated polymers. By either changing microstructures, modifying the surface of inorganic nanowires, or oxidizing or reducing via doping, the physical and chemical properties like transmittance, electrical and thermal conductivity, flexibility, solubility, and energetics (e.g., density of states, work function, the valence band (VB) energy, conduction band (CB) energy, or the lowest unoccupied molecular orbital (LUMO) and highest occupied molecular orbital (HOMO) can be manipulated. Three projects were carried out in this dissertation. Silver nanowires functionalized with different thiols and blended with PEDOT:PSS were examined in the first project. This project mainly investigated how the surface modifiers affected the nanowires dispersability, compatibility with various solvents or polymers, and electrical properties of the nanowire-polymer composites. In the second project, tellurium nanowires and ferric chloride doped P3HT were used to characterize energy filtering effects on charge carrier transport. The effect of energy filtering to the films electrical conductivity, Seebeck coefficient, and power factor of polymer-nanowire composites were also examined. The third project further focused on charge transport in conjugated polymers doped with various p-type dopants (e.g., ferric chloride and molybdenum tris(1,2-bis(trifluoromethyl)ethane-1,2-dithiolene) (Motfd$_3$)). The effect of dopant electron affinity and size on doping efficiency, electrical conductivity, Seebeck coefficient, and power factors of doped polymers at different doping levels were investigated.

1.1 Backgrounds

1.1.1 Metals or Inorganic Semiconductors Nanowires

Nanowires, defined as nanomaterials with length-to-width ratio > 1000, have extremely small diameters (few to a hundred nanometers), good mechanical flexibility, and large surface-to-volume ratio. These excellent properties provide nanowires with large potential applications in sensors, transistors, lasers, transparent electrodes, thermoelectrics, and solar cells. The common synthesis methods of nanowires includes vapor-liquid-solid-method,[12] solution phase,[13] and no-catalytic growth methods.[14] Ran *et al.* reported a one-step silver nanowires synthesis and they yielded a silver nanowire aspect ratio over 1000.[15] Yang *et al.* tried to effectively use silver nanowires as electrodes to fabricate flexible organic solar cells.[16] Meanwhile, the physical properties of nanowires such as electrical conductivity, thermal conductivity, and yield strength are significantly different from the bulk materials. Li *et al.* fabricated conducting films with purified silver nanowires and they obtained 99% transmittance at 130 ohm/square, which were even better than commercial indium tin oxide (ITO).[17] Furthermore, the dispersability of nanowires in different solvents was also controllable by utilizing either hydrophilic or hydrophobic molecules as surface modifiers. Surface modifiers not only change nanowire chemical properties but also affect their energetics (e.g., the work function, the valence band and conduction band energies). The change in energetics further influenced the charges transport in nanowire blends. For instance, Brown *et al.* reported that the work function of PbS nano-rods can vary from 3.6 to 4.9 eV when different ligands are used.[18]

1.1.2 Doped Organic Conjugated Polymers

Organic conjugated polymers have wide applications in organic-based light-emitting diodes,[19,20] field-effect transistors,[21,22] and thermoelectrics[23,24] due to the controllable electrical and optical properties,[25] excellent mechanical flexibility,[26] and solution processability[27] compared with traditional inorganic semiconductors. It is still difficult to control the electrical conductivity that is a function of carrier concentration and mobility. Molecular doping is one major method to manipulate these properties. By controlling the oxidation degree of conjugated polymers (e.g., removing electrons (p-type doping) or donating electrons (n-type doping)), the electrical conductivity and Seebeck coefficient can be dramatically changed. Taking p-type doped conjugated polymers for example, the electrical conductivity and Seebeck coefficient of 1% wt. $FeCl_3$ doped P3HT is *ca.* 3 S/m and 450 μV/K. However, as $FeCl_3$ wt. increases to 32%, the electrical conductivity and Seebeck coefficient of doped P3HT change to *ca*. 1800 S/m and 40 μV/K.[28] In previous studies, researchers found that at the same doping ratio, the electrical conductivity of the same polymer doped with different dopants (e.g., F4TCNQ, and $FeCl_3$) can have large differences. However, it is still not clear the role of dopant size and electron affinity (p-type) on the electrical conductivity. Since the electrical properties of doped conjugated polymers are closely linked to polymers microstructure,[29] it is important to determine how the polymer's microstructure and driving force for charge transfer is affected by dopants size and electron affinity.

1.1.3 Nanowires and Organic Conjugated Polymers Composites

As mentioned in the previous section, nanowires have many excellent properties such as large charge-carrier mobility, high charge-carrier concentration, strong mechanical flexibility, and high surface-to-volume ratio. For conjugated polymers, the advantages include good solution processability, wide bandgap, and large Seebeck coefficients. To combine the benefits of the two types of materials and improve materials performance, making polymers (e.g., PEDOT:PSS and P3HT) and inorganic nanowires (e.g. AgNWs and Bi_2Te_3) blends is one of the most popular methods. The composites can be either fabricated as transparent electrodes with high transmittance or used as thermoelectric materials with high power factors. Choi *et al.* fabricated highly flexible (the sheet resistance only increased by *ca.* 5% after 200 cycles of stretching and bending) transparent electrodes and with high electrical conductivity (*ca.* 11 ohm/square at 84% transmittance) based on silver nanowire-PEDOT:PSS composites.[30] From the thermoelectric standpoint, He *et al.* reported a power factor of 13.6 mW K^{-2} m^{-1} Bi_2Te_3-P3HT nanocomposites, which is around 4 times that of pristine P3HT (3.9 mW K^{-2} m^{-1}).[28]

1.1.3.1 Silver Nanowires and PEDOT:PSS Transparent Electrodes

Silver nanowires and PEDOT:PSS are attractive materials with high electrical conductivity, high flexibility, and high visible light transmittance. These composites can be fabricated as good transparent electrodes and used for thermoelectrics. One major challenge to fabricate high-quality materials with nanowires and polymers is the compatibility issue between the nanowires and polymers. Pristine nanowires may have poor compatibility with conjugated polymers which results in inhomogeneous films. Thus, it is necessary to find ways to increase the compatibility of nanowires with polymers. In previous reports, the dispersability of modified nanoparticles were largely improved in solution.[31] Thus, to obtain better compatibility with solvents or solutions, adjusting the surface modifiers on the nanowires is an effective method. Thiols are excellent surface modifiers for use with many bulk metals and metal nanowires.[32] To test the morphology and electrical conductivity difference of AgNWs-PEDOT:PSS blends, thiols with different functional groups were used to modify silver nanowires (e.g. 1-decanethiol (hydrophobic), mercaptoethanol(hydrophilic), and sodium 3-mercapto-1-propanesulfonate (ionic)). The work function of modified silver nanowires was altered as the smodifiers changed. Tuning the work function may enable AgNWs to replace a variety of traditional electrodes that span a range of work functions, such as indium tin oxide (ITO) (4.8-5.2 eV),[33] aluminum (4.06-4.26 eV),[34] silver (4.26-4.74 eV),[35] and gold (5.10-5.47 eV).[36]

1.1.3.2 Tellurium Nanowires and Poly (3-hexylthiophene-2,5-diyl) Thermoelectrics

Traditional thermoelectric devices are made with expensive, rare and brittle materials (e.g. bismuth telluride),[37] which lead to relatively expensive costs. Nanowires and conjugated polymers are two types of potential materials that can be used to fabricate flexible devices. He *et al.* blended $FeCl_3$ doped P3HT with Bi_2Te_3 nanowires.[28] The P3HT-Bi_2Te_3 composites obtained a four times higher power factor than pure P3HT. The authors suggested this enhancement was due to energy filtering at nanowire-polymer interfaces. However, no direct evidence confirmed this hypothesis. To examine the role of energy filtering in organic-inorganic nanocomposites, we first built up a proper energy barrier at the nanowires-polymers interfaces (~0.04-0.2 eV). Tellurium nanowire is a promising inorganic nanowire, with a 4.9 eV reported work function and ~500 $cm^2V^{-1}s^{-1}$ high hole motilities in bulk Tellurium.[38,39] P3HT is the most commonly used conjugated polymer. Furthermore, the energetics of P3HT films can be controlled by the degree of oxidation of P3HT, which can be adjusted via various dopants at different concentrations (e.g. $FeCl_3$, I_2, and $HClO_4$).[40,41] As the doping ratio changes, the work function of doped P3HT can vary from 4.4 eV to 5.4 eV. Comparing with the reported 4.9 eV work function of tellurium nanowire, this range can be used to build up different energy barriers between the tellurium nanowires and P3HT to explore the role of energy filtering (Figure 1.4). Clarifying the role of energy filtering and the mechanisms of charge transport in organic-inorganic composites will help researchers to develop more efficient materials.

1.2 Definition of Energetics

Charge transport through material interfaces is vital to the performance of electronic devices. Energetics of materials is one factor that can manipulate charge transport. These energetics include the work function, the valence band (or HOMO), and the conduction band (or LUMO). Figure 1.1 shows the Fermi level of a semiconductor. At 0 K, the Fermi level is an energy level where no electrons can exist above. As temperatures above 0 K, it is defined as the energy where an electron has 50% probability to occupy. Figure 1.2 shows schematic energy diagrams of a metal and a semiconductor. Vacuum level refers to a position away from the surface where a free stationary electron has no kinetic energy. This position is usually a few nanometers from the materials surface.[42] The work function (Φ) is defined as the energy difference between the Fermi level (E_f) and the vacuum level. Ionization energy (IE) is the energy difference between the valence band (VB) (or HOMO) and the vacuum level. Electron affinity refers to the energy difference between the conduction band (CB) (LUMO) and the vacuum level.

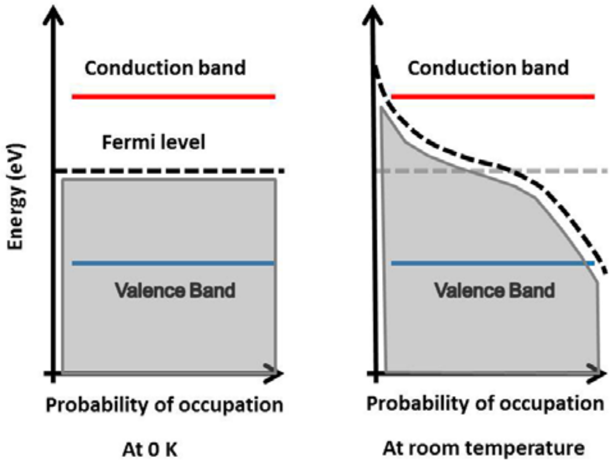

Figure 1.1 Fermi level of a semiconductor at 0K and room temperature.

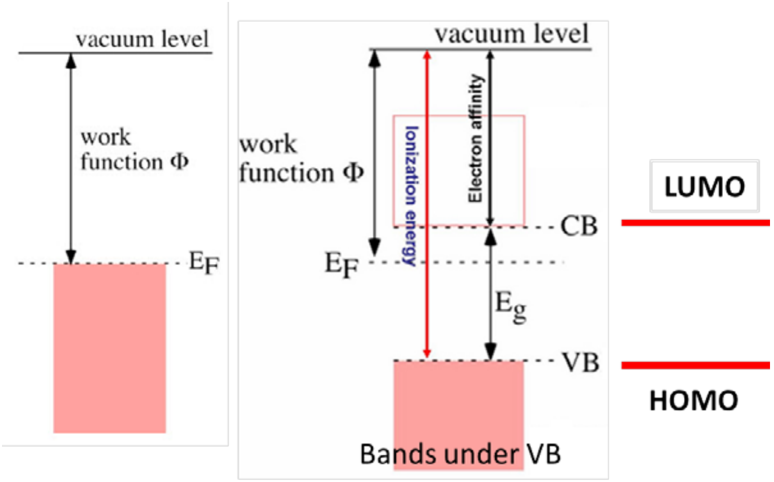

Figure 1.2 Schematic energy diagram of a metal (left) and a semiconductor (right).

1.3 Thermoelectric Effect

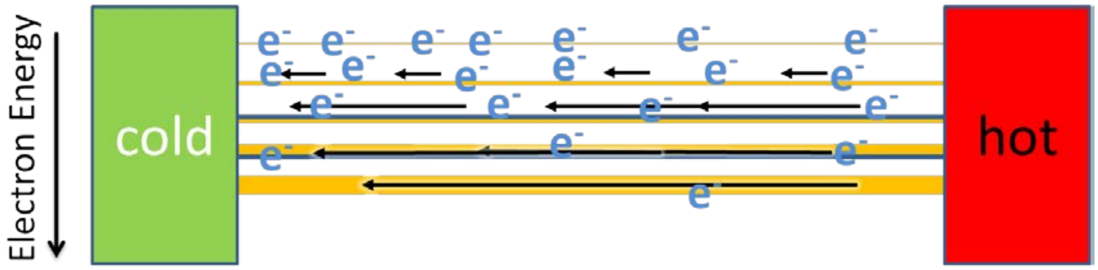

Figure 1.3 A schematic representation of the phenomenon leading to the Seebeck effect.

Figure 1.3 shows the phenomenon of the Seebeck effect, which is the effect that thermoelectric materials use to generate electrical power from a temperature difference. Electrons diffuse from T_{hot} region to T_{cold} region, as there is a temperature difference between two regions of a conductor. Since thermally excited electrons move faster than colder electrons, the electrons accumulate at the colder side and a potential difference is established between the two regions. The conversion between thermal energy and electrical energy is called the thermoelectric effect. Seebeck, Peltier, and Thomson effects are three related thermoelectric effects. Seebeck effect, in which a temperature difference is directly converted into a voltage, was named by Thomas J. Seebeck for his discovery of this phenomenon. Peltier effect is the reverse of the Seebeck effect, i.e., electrical current run through a material creates a temperature differential. Thomson effect refers to voltage build up in conductors because of electric current and temperature gradient. In this dissertation, only the Seebeck effect is focused upon. In the Seebeck effect, since the induced voltage is proportional to a temperature gradient, we can write an equation to define the Seebeck coefficient as $S=\Delta V/\Delta T$. Where S is Seebeck coefficient, ΔV is induced voltage difference, and ΔT is a temperature difference. For the same material, the Seebeck coefficient changes at different temperatures. For example, the Seebeck coefficient of polycrystalline bismuth can vary from *ca.* -200 µV/K at 310 K, to -90 µV/K at 473K.[43] The performance of a thermoelectric device is calculated as $ZT = \frac{\sigma\alpha^2 T}{\kappa}$. Where ZT is the figure-of-merit; α is Seebeck coefficient; σ is electrical conductivity; T is absolute temperature; κ is thermal conductivity, and $P = \sigma\alpha^2$ is power factor. The equation shows that to achieve high figure-of-merit ZT, it is necessary to improve a material electrical conductivity and Seebeck coefficient or decreasing a material's thermal conductivity. However, these three parameters typically have opposite dependencies (*i.e.,* when the electrical conductivity increases, the Seebeck coefficient decreases).[44] To circumvent these interdependencies, strategies such as nanostructuring to control phonon scattering,[45,46] increasing the slope of the electronic density of states (e.g., through the quantum confinement effect or introduction of appropriate dopants),[47,48,49] and utilizing the energy filtering effect need to be examined.[50]

1.4 Energy Filtering

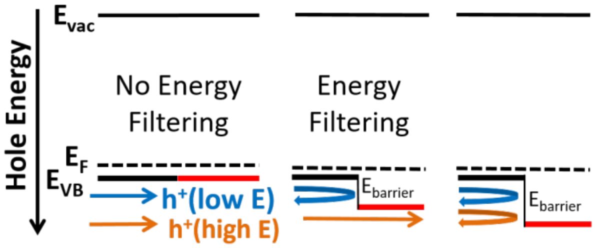

Figure 1.4 The effect of the energy barrier to charge carriers.

The energy filtering model explores the relationship between energy barriers and thermoelectric properties (electrical conductivity and Seebeck coefficient).[51] It predicts that at a proper energy barrier, low energy carriers will be scattered, and high energy carriers will pass through the interfaces. Since carriers at different energies will now make different contributions to the electrical conductivity, this filtering process can lead to higher Seebeck coefficients. According to theoretical models and previous experiments, a couple parameters need to be satisfied to observe effective energy filtering phenomenon: i) Low volume of loading nanocrystals (*i.e.*<10%) and ii) Proper energy barriers between two components (typically 0.04 eV to 0.2 eV).[50,51,52,53,54,55] Figure 1.4 is an example of how energy barriers can affect hole transport in p-type semiconductors. When there is no energy barrier, charge carriers at different energy states will pass through the boundaries. As the energy barrier difference increases to the appropriate range (*i.e.* 0.04 eV ~ 0.2 eV), higher energy charge carriers will pass through while the low energy holes will be scattered. Since high energy carriers transfer more entropy than low energy carriers, a higher Seebeck coefficient will be obtained without major sacrifices in electrical conductivity. When the energy barrier is larger than 0.2 eV, most charge carriers will be impeded and the electrical conductivity will drop significantly. Thus, if proper interfacial energy barrier is built up, an enhanced Seebeck coefficient and power factor may be obtained.

Chapter 2: Transparent Electrodes of Modified Silver Nanowire and Conjugated Polymer Composites

This chapter is based on the manuscript: Zhiming Liang, Kenneth R. Graham, *ACS Appl. Mater. Interfaces*, **2015**, 7 (39), 21652–21656.[56]

2.1 Introduction

Transparent electrodes are required in a number of opto-electronic devices, such as light emitting displays, touch screens, and solar cells.[57,58] For these applications the electrodes should be highly transparent to visible light with a low sheet resistance (R_S). Indium Tin Oxide(ITO), likely the most widely used material for transparent electrodes, meets these requirements with > 90% transmittance at 550 nm and a R_S of 10 Ω/□ on glass.[59] However, there are two main disadvantages of ITO for use in the upcoming generation of flexible, solution processed electronics; namely, ITO has poor mechanical flexibility and cannot be solution-processed.[58,59] Thus, alternative materials that will enable large-scale, rapid and inexpensive solution processed devices, as well as flexible electronics, are being widely explored.[58,60,61] Attractive alternatives to ITO include carbon nanotube films (R_S=60 Ω/□ at T=90.9%),[62,63,64] graphene (R_S=21.26 Ω/□ at T=88%),[65] and metal nanowires such Ag (R_S=13 Ω/□ at T=85%, R_S=20 Ω/□ at T=93%),[66,67] and Cu (R_S=24 Ω/□ at T=88%, R_S=100 Ω/□ at T=92-93%).[68,69] Higher values for AgNWs (R_S=8.5Ω/□ at T=90) and CuNWs (R_s=11.2 Ω/□ at T=91%) are also possible using an electrospinning fabrication method, though the wire diameters are significantly larger at around 500 nm.[70] Compared with carbon materials, metal nanowire films typically demonstrate lower R_S at comparable transmittance. Of the metal NWs, Ag is more widely studied owing to its higher oxidative stability over Cu and more neutral color as opposed to the orange hue of CuNWs.

Commonly, AgNW films are used in combination with the conductive polymer blend poly(3,4-ethylenedioxythiophene):polystyrenesulfonate (PEDOT:PSS), where PEDOT:PSS serves multiple roles including filling the voids between AgNWs, work function modification, and planarization. Various methods have been reported to fabricate transparent AgNW/PEDOT:PSS electrodes. These include subsequent spray deposition of AgNWs and PEDOT:PSS spray deposition of AgNWs followed by embedding the AgNWs network into PEDOT:PSS,[71] and subsequent coating of AgNWs, polyvinyl alcohol, and PEDOT:PSS.[72] However, all these methods are either multistep processes or yield films with large surface roughness. To the best of our knowledge, only one report currently exists of a one-step processing method for AgNW/PEDOT:PSS films; however, in that work, it is not clear if the films are homogeneous over a large scale, and if so, it is not clear how this was achieved.[73]

Here we report the surface modification of AgNWs with various thiols, which allows for compatibility with polymers, such as PEDOT:PSS, and solvents to be controllably adjusted while simultaneously reducing wire-to-wire junction resistance. Utilizing this surface modification strategy a one-step processing method is demonstrated for the fabrication of uniform AgNW/PEDOT:PSS composite films. Surprisingly, there are few previous reports of AgNW modification with thiols,[74,75] despite the facile modification process and versatility it provides. Herein, it is demonstrated that AgNWs can be readily modified with thiols ranging from ionic to hydrophobic, with the thiols displacing the polyvinylpyrrolidone (PVP) previously present on the AgNW surface. Surface modification not only allows the compatibility with polymers and solvents to be tuned, but it can also significantly decrease wire-to-wire junction resistances. As will be demonstrated, this combination of improved compatibility and minimized junction resistance leads to uniform AgNW/PEDOT:PSS films with high transmittance and low R_S.

2.2 Results and Discussion

2.2.1 Surface Modification of Silver Nanowires

To probe whether as-prepared PVP coated AgNWs could be modified with thiols, X-ray photoelectron spectroscopy (XPS) is used to compare sulfur binding energies between pure sodium 3-mercapto-1-propanesulfonate (MPS) and MPS modified AgNWs (MPS-AgNWs). As shown in Figure 2.1, sulfur is clearly present in the XPS spectrum of the MPS-AgNW sample, indicating that MPS remains adsorbed on the AgNW surfaces following rinsing in ethanol and deionized water. Analysis of S peak positions in the XPS spectra further confirms MPS binding to the AgNWs. The XPS spectrum of pure MPS shows $2p_{3/2}$ binding energies of 163.69 eV and 168.45 eV for

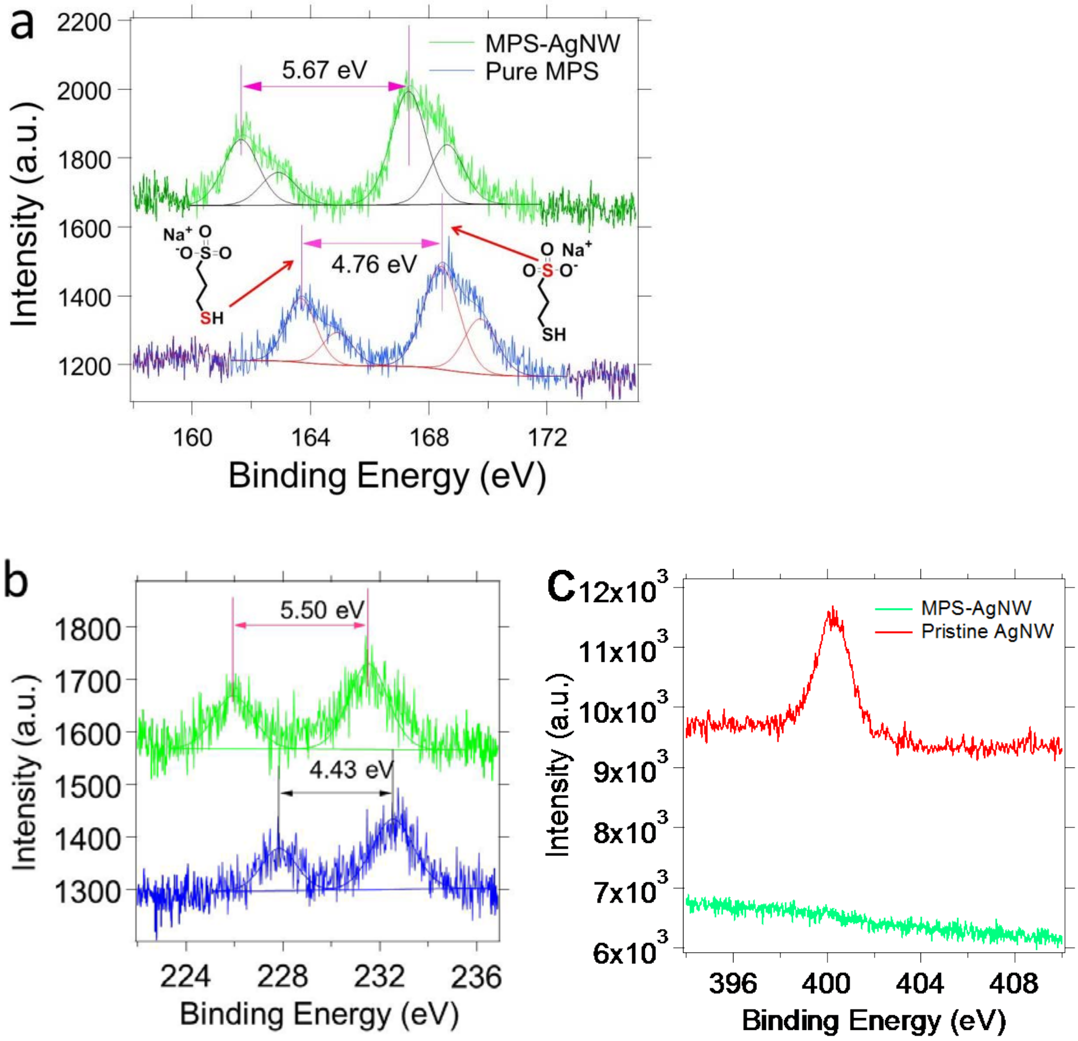

Figure 2.1 XPS spectra of a) pristine MPS S2p (blue) and MPS-AgNWs S2p (green), b) pristine MPS S2s (blue) and MPS-AgNWs S2s (green), c) MPS-AgNW N 1s (green), Pristine AgNW N1s(red).

mercapto and sulfonate sulfurs, respectively, which is a difference of 4.76 eV. For MPS-AgNWs, the mercapto sulfur $2p_{3/2}$ peak is shifted to lower binding energy by 2.05 eV at 161.64 eV, while the sulfonate sulfur $2p_{3/2}$ binding energy is shifted by only 1.14 eV to 167.31 eV, a difference of 5.67 eV between sulfur peaks as highlighted in Figure 2.1(a) This larger shift in the binding energy of the mercapto sulfur in the MPS-AgNW sample confirms that this sulfur is binding with the AgNW surface. As expected, the same trend exists for the S2s peaks as shown in Figure 2.1(b). The synthesis of AgNWs involves the use of PVP to stabilize and promote one-dimensional growth, resulting in PVP coated AgNWs.[76] To determine if this PVP is displaced through the surface modification of AgNWs, the nitrogen 1s peak in the XPS spectra is examined. Figure 2.1(c) shows a strong N 1s peak at 400.29eV originating from the N atom in the PVP repeat unit. In contrast, MPS modified AgNWs display no evidence of this N 1s peak. This data indicates that MPS displaces PVP on the AgNW surface. Importantly, this displacement of PVP lowers the wire-to-wire junction resistance, as will be highlighted later in the manuscript.

Silver nanowires were also modified with decanethiol (DT) and mercaptoethanol (MEtOH), and as expected DT-AgNWs display distinctly different dispersability than MEtOH- and MPS-AgNWs. For example, DT-AgNWs disperse well in ethanol and are completely aggregated in deionized water (Figure 2.2). By contrast, MPS-AgNWs can be well-dispersed in both ethanol and water, though the dispersions are more stable in water than in ethanol. MEtOH-AgNWs are also well-dispersed in water and ethanol. This data confirms that AgNW dispersability can be readily tuned through thiol modification. Control over dispersability is particularly relevant to the development of completely solution processed electronics, where orthogonal solvents are generally necessary for processing multilayer devices.

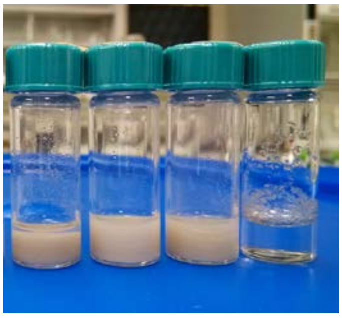

Figure 2.2 Optical images of modified silver nanowires. From left to right, MPS-AgNWs in EtOH, MPS-AgNWs in H_2O, DT-AgNWs in EtOH, and DT-AgNWs in H_2O at concentrations of 1 mg/ml. (30 minutes after shaking to create a uniform dispersion)

2.2.2 Morphology of Modified Silver Nanowire and PEDOT:PSS Composites.

The effect of surface modifier on the morphology of AgNW/PEDOT:PSS blend films are examined through optical microscopy and scanning electron microscopy (SEM). In this comparison AgNWs purchased from Blue Nano (BN) are used. MPS- and MEtOH-AgNW/PEDOT:PSS blends are compared at AgNW to PEDOT:PSS wt. ratios of 1:9, 2:8, 3:7, and 4:6, while DT- and unmodified (UM)-AgNW/PEDOT:PSS blends are compared at wt. ratios of 1:19, 1:9 and 2:8. The images presented in Figure 2.3 show AgNW/PEDOT:PSS wt. ratios of 2:8 for the various surface modifiers. These images reveal that MPS-AgNW/PEDOT:PSS blends are uniform with AgNW wt. ratios up to 4:6. Mercaptoethanol modified-AgNW/PEDOT:PSS blends also show a homogeneous morphology at wt. ratios up to 4:6, though the MEtOH-AgNW blends appear slightly less uniform than MPS-AgNW blends. On the other hand, DT-AgNW/PEDOT:PSS films are inhomogeneous with large aggregated regions appearing throughout the concentration range from 1:19 to 2:8. UM-AgNW/PEDOT:PSS films appear homogenous at a low AgNW ratio of 1:19, but larger scale defects appear at increased AgNW wt. ratios of 1:9 and 2:8 as evident in Figure 2.3.

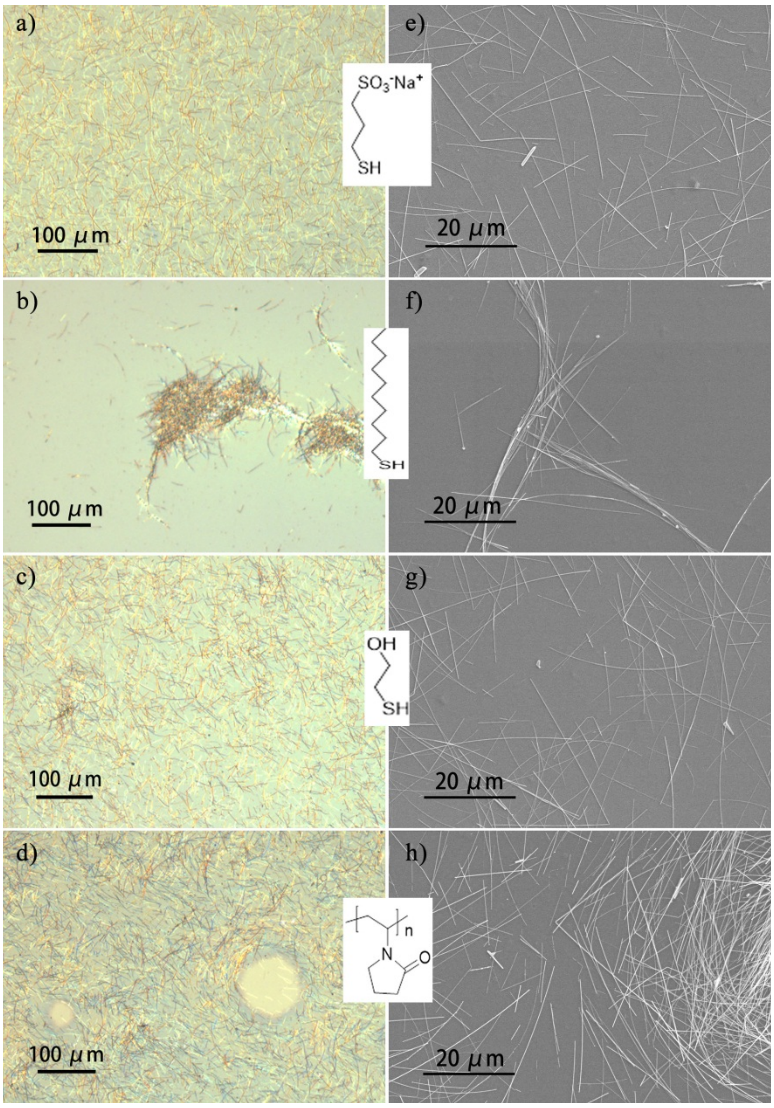

Figure 2.3 Optical (left) and SEM (right) images of AgNW/PEDOT:PSS blends at a 2:8 wt. ratio: a, e) MPS-AgNWs; b, f) DT-AgNWs; c, g)MEtOH-AgNWs; and d, h) UM–AgNWs

2.2.3 Sheet Resistance vs. Transmittance for Modified Silver Nanowire and PEDOT:PSS Composites.

The trend in film quality with MPS-AgNWs and DT-AgNWs forming the most and least homogeneous films with PEDOT:PSS, respectively, are predicted from considerations of basic electrostatic interactions. Here the anionic sulfonate group of MPS interacts strongly with the cationic PEDOT, thus resulting in homogeneous MPS-AgNW/PEDOT:PSS films. The hydrophilic and more polar MEtOH modified silver nanowires will also interact more favorably with the aqueous solvent and PEDOT:PSS than will the less polar PVP coated UM-AgNWs, thus yielding more homogeneous films. Finally, the least polar and hydrophobic DT leads to unfavorable interactions with both PEDOT:PSS and the aqueous solvent, resulting in significant DT-AgNW aggregation.

Transmittance (T) vs. sheet resistance (R_S) data shown for the AgNW/PEDOT:PSS blend films is in Figure 2.4. Each series, whereby the only parameter changed is the AgNW/PEDOT:PSS ratio, shows a 1.5 to 3 order of magnitude decrease in R_S as the AgNW ratio is increased from 1:19 to 2:8 or 1:9 to 4:6. Accompanying this drop in R_S is a decrease of 0.12 to 0.24 in T. This decrease in R_S and T with increasing AgNW concentration is attributed primarily to the contribution of the AgNWs, though the PEDOT:PSS film thickness also increases with AgNW concentration (Table 2.1). Surprisingly, at similar transmittance values MPS- and MEtOH-AgNW/PEDOT:PSS films display approximately an order of magnitude lower R_S than the UM-AgNW/PEDOT:PSS films. As will be discussed, this trend is attributed to the higher wire-to-wire junction resistance of the PVP coated AgNWs. Thus, modification of the AgNWs with MPS or MEtOH has two complementary effects that include uniform film morphologies and lower R_S at comparable T.

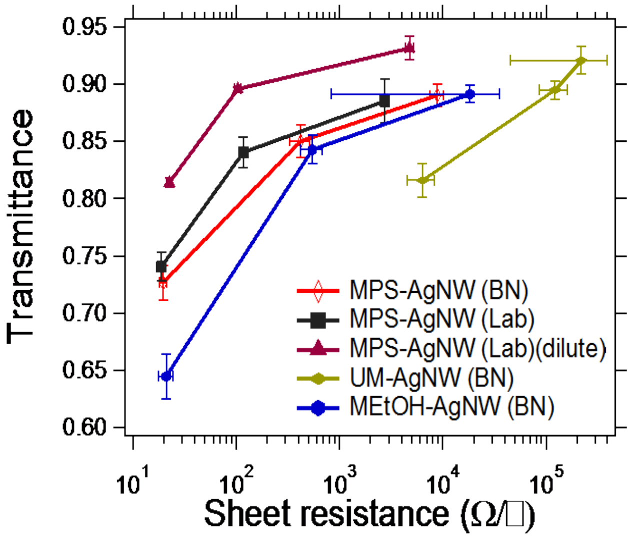

Figure 2.4 Sheet resistance vs transmittance at 550 nm of AgNW/PEDOT:PSS films: UM-AgNW(BN) at wt. ratios of 1:19, 1:9, 2:8; MEtOH-AgNW(BN), MPS-AgNW(BN), MPS-AgNW(Lab) and MPS-AgNW(Lab)(dilute) at wt. ratios of 1:9, 2:8, 4:6.

Table 2.1 Films thickness of sodium 3-mercapto-1-propanesulfonate modified AgNWs(Blue Nano and Lab made) (MPS-AgNWs)/PEDOT:PSS blends at different silver nanowire wt. ratio from 1:9 to 4:6. And MPS-AgNW(lab made)/PEDOT:PSS(thin) at different nanowire wt. ratio from 1:6 to 1:1 (Unit: nm)

	1:9	2:8	4:6	1:6	2:5.3	1:1
MPS-AgNW(BN)	114±13	154±3	194±10			
MPS-AgNW(Lab)	99±5	125±6	160±7			
MPS-AgNW(Lab)(thin)				83±3	91±3	110±9

Original experiments with MPS-AgNW/PEDOT:PSS blends containing BN AgNWs yielded respectable values of 20 Ω /□ at 73% T, though multiple optimizations are possible to improve these performance metrics. For example, the electronic properties of silver nanowire films are greatly affected by lengths and diameters of the AgNWs, with larger L/D ratios resulting in decreased R_S at similar transmittance values.[77,78,79] Original experiments were carried out with AgNWs purchased from Blue Nano (BN), with a diameter observed through SEM of 118±34 nm and length of 28.7±14.7μm as shown in Figure 2.5. In an effort to improve performance metrics, we synthesized AgNWs in our laboratory (Lab) based on the procedure reported by Ran, *et al.*[79] Our synthesis yielded AgNWs with a diameter of 59±11 nm and lengths of 36.6±21.4 μm (Figure 2.5). As shown in Figure 2.4, films utilizing MPS-AgNWs(Lab) display slightly better performance than MPS-AgNWs(BN). Taking AgNWs at wt. ratios equal to 4:6 for instance, MPS-AgNW(BN) has a T=72.7±1.5% at R_S=19.6±1.7 Ω/□, while MPS-AgNW(Lab) has a T=74.1±1.2% at R_S=18.9±1.7 Ω/□.

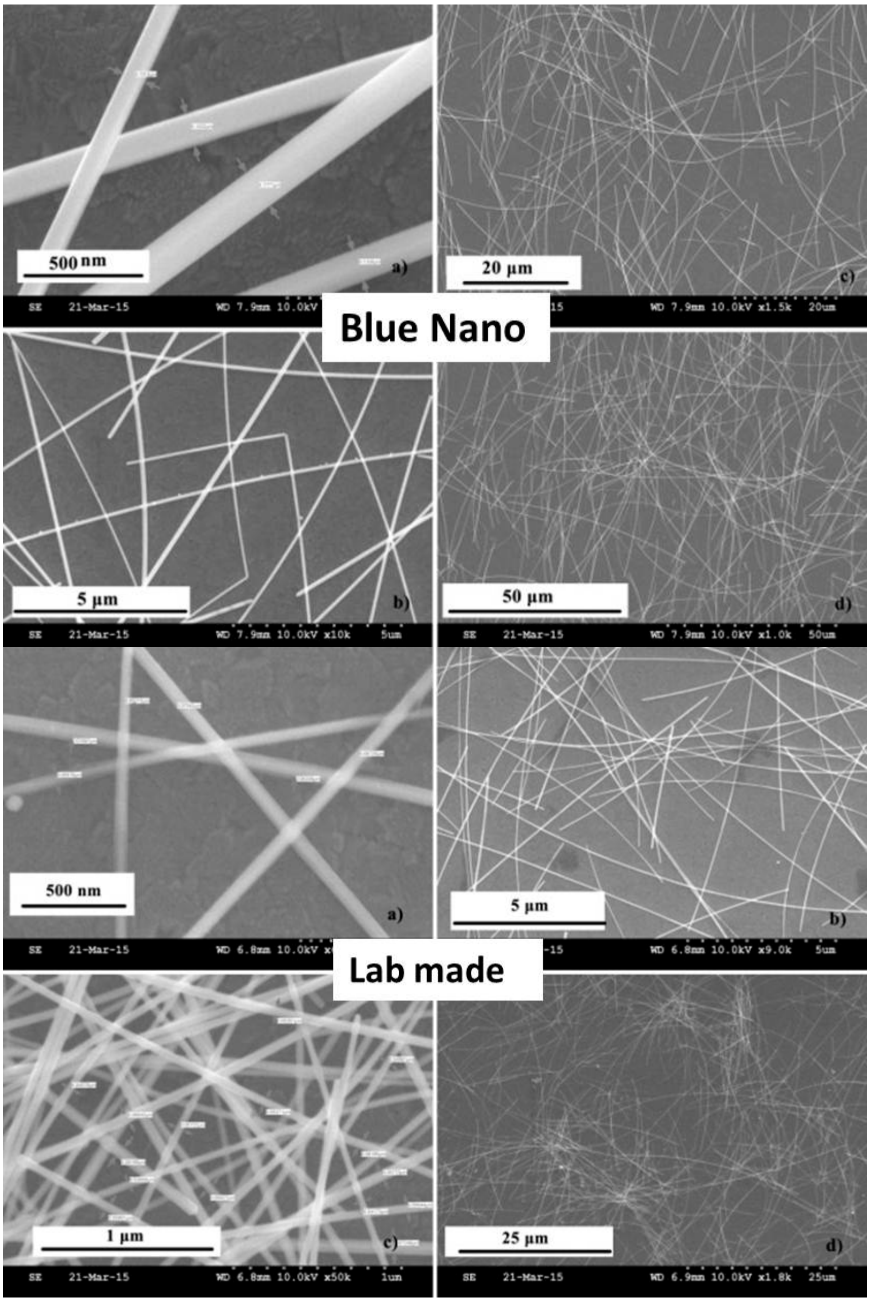

Figure 2.5 SEM images of Blue Nano AgNWs (up) and lab-made AgNWs (bottom).

The transmittance may be further optimized through reducing the overall film thickness and further increasing the relative AgNW concentration. Here PEDOT:PSS was diluted from 1.1 to 0.73 wt.%, resulting in thinner films with MPS-AgNW/PEDOT:PSS wt. ratios of 1:6, 2:5.3, and 1:1 Table 2.1). Figure 2.4 displays higher performance for these MPS- AgNW(Lab)/PEDOT:PSS(dilute) blends. At a wt. ratio of 1:1, these thinner films (thickness of 110±9 nm vs. 160±7 nm for non-dilute blends) display R_S=22.6±1.2 Ω/□ and T=81.4±0.4% with similar homogeneous film morphologies.

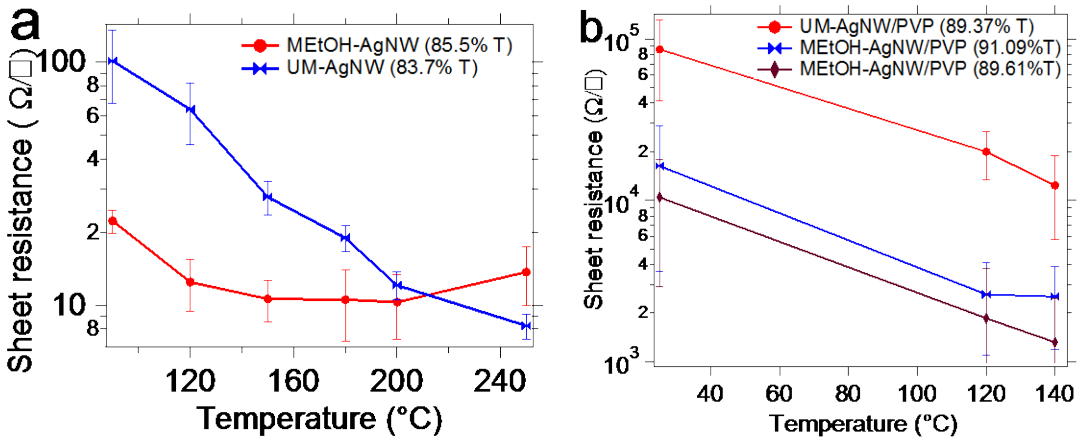

Figure 2.6 Temperature vs. Sheet resistance of MEtOH-AgNW, and UM-AgNW(a), MEtOH-AgNW/PVP and UM-AgNW/PVP film (b).

Unmodified-AgNW(BN)/PEDOT:PSS blends show approximately an order of magnitude higher R_S than MPS or MEtOH modified AgNW(BN) blends at similar T. Taking AgNW wt. ratios of 2:8 for instance, UM-AgNW(BN) has a R_S of *ca*. 6000 Ω/□ at a T of 82%, while MEtOH-AgNW(BN)/PEDOT:PSS has a R_S of 500 Ω/□ at. 84% T. To determine if the lower R_S of MPS-and MEtOH-AgNW/PEDOT:PSS blends is due to increased wire-to-wire charge transfer rates (lower junction resistance) or increased charge transfer rates between AgNWs and PEDOT:PSS, pure films of MEtOH-AgNWs(BN) and UM-AgNWs(BN) are compared. The pure UM-AgNW and MEtOH-AgNW films were spun cast on glass substrates, with the films shown in Figure 2.6a having comparable absorbance values of 0.11±0.01 (MEtOH-AgNWs) and 0.14±0.01 (UM-AgNWs) at the AgNW absorbance peak of 355nm (Figure 2.7). The films were then annealed for 20 minutes at temperatures ranging from 90 to 300 °C, with R_S measurements taken after the films had cooled to room temperature. Annealing temperatures of 300 °C cause the AgNWs to break apart, resulting in R_S values of *ca.* 10^8 Ω/□. Figure 2.6a shows that after a 90 °C annealing step the UM-AgNW film has a R_S of 100±34 Ω/□ while the MEtOH-AgNW has a R_S= 22.3±2.4 Ω/□, in spite of the slightly lower absorbance of the MEtOH-AgNW film. This difference in R_S for the pure

AgNW films of similar T (83.7% and 85.5% at 550 nm for UM-AgNWs and MEtOH-AgNWs, respectively), indicates that there must be higher wire-to-wire charge transfer rates (lower junction resistance) for the MEtOH-AgNWs than the UM-AgNWs. Annealing at a higher temperature (120-200 °C) has been shown to fuse the AgNW junctions, thus nearly eliminating any junction resistance. Since after a 200℃ annealing step the films show a nearly identical R_S, this confirms that modification with MEtOH lowers the wire-to-wire junction resistance prior to high temperature annealing. This decreased junction resistance at lower annealing temperatures is another major advantage of AgNW surface modification.

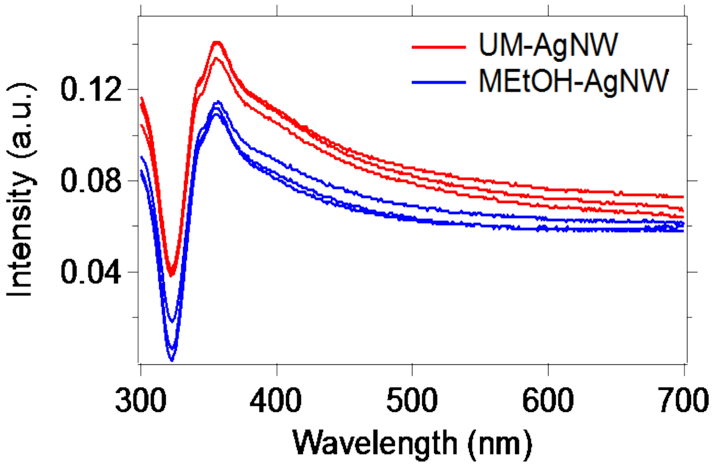

Figure 2.7 UV-Vis absorbance spectra of UM-AgNW and MEtOH-AgNW films on glass.

Further verification that the AgNW-to-AgNW junction resistance is lower in MEtOH-AgNWs than in UM-AgNWs is demonstrated by comparing the effects of an insulating polymer matrix. Here, the system is morphological as similar as possible to the PEDOT:PSS blend, only the polymer host is the non-conductive polymer PVP. Mercaptoethanol-AgNW(BN)/PVP and UM-AgNW(BN)/PVP (Film absorbance at AgNW λ_{max}(355 nm)= 0.06$\pm$0.01, 7:3 AgNW/PVP ratio) blend films' sheet resistance and transmittance are examined, and similar to the PEDOT:PSS blends the UM-AgNW/PVP film has approximately an order of magnitude higher R_S than MEtOH-AgNW/PVP films after annealing at 25°C, 120°C, and 140°C (Figure 2.6b). Due to the insulating polymer host, the absolute R_S values of both films are approximately an order of magnitude higher than with PEDOT:PSS as the host polymer. All films have similar morphology, thus further supporting that displacement of PVP with MEtOH on the AgNW surface lowers the AgNW-to-AgNW junction resistance.

2.3 Conclusion

In summary, surface modification of AgNWs provides a means of controllably altering solubility, compatibility with various polymers, and minimizing wire-to-wire junction resistance. Through blending MPS-AgNWs with PEDOT:PSS, uniform films that can be utilized as transparent electrodes for electronic devices were formed with a one-step solution processing method. The facile surface modification of AgNWs with thiols opens up a variety of promising future uses. These could include controllably altering the work function of AgNWs by controlling the dipole moment and direction of the surface modifier, altering dispersibility of AgNWs for utilization in multistep solution processed devices where orthogonal solvents are needed, and increasing compatibility with various polymers to create electrically conductive polymer films with mechanical properties such as flexibility or strechability.

2.4 Experimental Details

AgNWs synthesis

0.2455g silver nitrate (Aldrich, 99.9999% trace metal basis) was added to 4.0908ml ethylene glycol (Sigma Aldrich, anhydrous, 99.8%) and sonicated for 8 min. at room temperature. 0.1091g PVP (Aldrich, Average M_W of 55, 000, PVP-55000) and 0.1091g PVP (Aldrich, Average M_W of 360,000, PVP-300,000) were dissolved in a separate 30ml of ethylene glycol. The PVP solution was heated to 130 °Cin an oil bath under stirring to help all PVP dissolve. To this PVP solution, 3.409ml 600 µM $FeCl_3$ ethylene glycol solution was rapidly added, followed by the silver nitrate solution. The flask was capped and kept at 130°C without stirring for 160 minutes.[79] Following the synthesis, rinsing and centrifugation with ethanol and D.I. water was performed to remove any unreacted reactants and eventually dispersed the nanowires in ethanol.

Surface modification of silver nanowires

Separately, solutions of sodium 3-mercapto-1-propanesulfonate (aldrich, technical grade 90%)(120µl, 10mM), 2-mercaptoethanol (alfa aesar 98+%)(120µl, 10mM), or decanethiol (aldrich, 96%)(120µl, 10mM) with pristine silver nanowires (5ml, 2mg/ml) in ethanol were prepared and left for 10h[75], with moderate shaking every two hours to keep silver nanowires dispersed in solution. After reaction the modified AgNWs were rinsed with ethanol (3x), chloroform (3x), and D.I. water (3x), using the centrifuge (fisher scientific, accuSpin micro 17 centrifuge) after each rinse to collect the AgNWs in the pellet and remove non-reacted thiols and PVP in the supernatant. The final solution was dispersed in water or ethanol.

Blending methods

A calculated amount of a 10 mg/mL AgNW in ethanol solution was centrifuged and the supernatant removed, leaving a known weight of AgNWs in the pellet. The PEDOT:PSS solution (aldrich, 1.1 wt. % in H_2O, surfactant-free, high-conductivity grade) was then added to the AgNW pellet, followed by moderate shaking by hand and vortex-mixer vibration for 5 minutes to disperse the AgNWs. Dilute AgNW/PEDOT:PSS blends were prepared by diluting the PEDOT:PSS solution to 0.733 wt. % with DI water prior to adding AgNWs.

Film preparation

All glass was cleaned through sequential sonication with sodium dodecyl sulfate (sigma aldrich, reagent plus ≥98.5%) in deionized water, deionized water, acetone, and isopropanol, followed by UV-ozone cleaning (helios-500) for 10minutes. AgNW/PEDOT:PSS solutions were spun cast at 1000rpm for 60 seconds, then 4000rpm for 10 seconds, followed by thermal annealing on a hotplate in the air at 150°C for 15min.

Film and AgNW characterization:

UV-Vis absorbance spectra were measured with a Thermo Scientific Evolution 300 spectrometer; SEM images were measured by a Hitachi S-4300with an accelerating voltage of 10 kV; Optical images were measured by an Olympus, Qcolor3 Microscope; Sheet resistance was measured with a four-point probe setup (Signatone S302-4, Keithley 2450 source meter); Films thicknesses were measured by a Dektak D6M/32 Profilometer; and XPS spectra were collected using X-rays generated by a Mg K-α source (1253.6 eV, PHI 04-548 Dual Anode X-ray source), an 11 inch diameter hemispherical electron energy analyser with multichannel detector, with pass energies of 23.5 eV and 0.025 eV step sizes(PHI 5600)

Chapter 3: Tellurium Nanowires and Conjugated Polymer Nanocomposites: Thermoelectric Properties and Role of Energy Filtering at the Interfaces

This chapter is based on the paper: Zhiming Liang, Mathias J. Boland, Kamal Butrouna, Douglas R. Strachan, Kenneth R. Graham. *J. Mater. Chem. A*, **2017**,5, 15891-15900. [80]

3.1 Introduction:

More than half of the energy used in the world is wasted as heat.[81,82] It will be of great economic and environmental benefit if a fraction of this waste heat can be collected and reused. Thermoelectric (TE) devices provide one such means of converting waste heat into electricity; however, the costs are prohibitively high for most applications based on currently available thermoelectric materials.[83,84] Lower cost materials than the traditionally used inorganic materials (e.g., Bi_2Te_3) are available, but their performance must be increased for them to be practically useful.[24]

The efficiency of a thermoelectric material is related to the figure of merit (ZT), where $ZT = \frac{\sigma\alpha^2 T}{\kappa}$. Here, σ is the electrical conductivity, α is the Seebeck coefficient, T is the absolute temperature, κ is the thermal conductivity, and $\sigma\alpha^2$ is the power factor. The equation shows that increases in ZT can be obtained by improving the electrical conductivity and/or the Seebeck coefficient, and/or decreasing the thermal conductivity. However, these three parameters typically have opposite dependencies (i.e., when σ increases, α decreases and κ increases).[44] To reduce these interdependencies, strategies such as nanostructuring,[45,46] increasing the slope of the electronic density of states (e.g., through the quantum confinement effect or introduction of appropriate dopants),[47,48,49] and utilizing energy filtering are being examined.[50] However, the majority of these efforts focused on inorganic materials.

Although inorganic semiconductors currently have significantly higher performance than organic materials, drawbacks such as mechanical stiffness, material scarcity, and expensive fabrication costs limit their applications.[85] Organic materials such as carbon nanotubes,[86,87,88] polyaniline,[89] polythiophenes [e.g., poly(3,4-ethylenedioxythiophene) blends],[90,91,92,93] and a number of other conjugated polymers are continuing to gain interest as potential TE materials.[94,95] These materials have advantageous properties over inorganic materials, such as their light weight, mechanical flexibility, and potentially low-cost materials and fabrication methods, which makes them attractive TE materials. Recently, organic-inorganic nanocomposites were demonstrated with higher power factors than both the pure polymers and pure nanocrystals.[96,97,98,99,100,101] For example, He *et.al* reported a Bi_2Te_3-P3HT composite with a power factor of 13.6 μW K^{-2} m^{-1}, which is 3 times higher than doped P3HT.[28] Choi *et.al* reported tellurium nanowire-single wall carbon nanotube composites and found the nanocomposite power factor was 3 times higher than pure TeNWs.[38] In part, these enhancements, as well as those observed in similar systems,[86,102,103] were attributed to energy filtering, but experimental measurements of material energetics were lacking and/or Seebeck coefficients were not compared to the pure nanocrystal films. Without these data, it is difficult to identify the role of energy filtering.

The Seebeck coefficient is determined by the average entropy transported per charge-carrier.[104] Thus, α will increase as charge-carriers with greater entropy contribute more to the total electrical conductivity. As shown schematically in the center energy diagram of Figure 3.1, introducing energetic barriers to restrict the transport of lower-energy charge-carriers, while allowing higher-energy carriers to pass unimpeded, is one means by which the average entropy transported per charge-carrier can be increased. This strategy, referred to as energy filtering,[51] has been experimentally and theoretically suggested to offer a route to improved power factors.[47,48,49,50] Energy filtering is typically accomplished by introducing nanoparticles into a conductive matrix, whereby the energy barrier between the matrix and nanoparticles only allows passage of higher-energy carriers. According to theoretical models and experiments, to observe enhancements in the TE performance through energy filtering the nanocrystal size should be on the order of the carrier scattering length and a small energy barrier (≤0.2 eV) should be present between the two components.[50,51,52,53,54,55] As shown in Figure 3.1, with no energy barrier charge-carriers of all energies pass between the components and there is no enhancement in α; a small barrier allows only higher-energy carriers to pass and thus an increase in α can be obtained without major sacrifices in σ; and a large barrier allows too few carriers to pass and σ drops significantly. Thus, the barrier height is a major consideration for effective energy filtering.

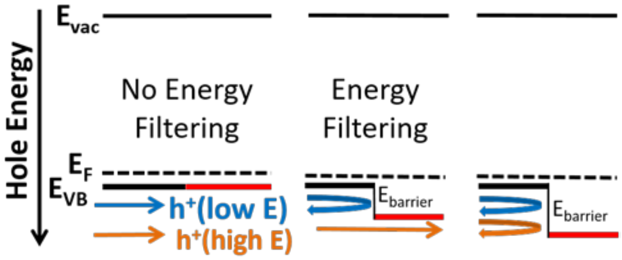

Figure 3.1 Schematic of how an appropriate energy barrier (center) can lead to energy filtering. E_{vac} is the vacuum level, E_F is the Fermi energy, and E_{VB} is the valence band energy. The black and red lines for E_{VB} represent the matrix and nanoparticles, respectively.

Surprisingly, despite claims of energy filtering in organic-inorganic composites, there is no systematic experimental data showing how the TE performance changes as the energy barrier varies in these materials. In this work, we experimentally vary the energy barrier between the highest occupied molecular orbital (HOMO) of poly(3-hexylthiophene) (P3HT) and the valence band (VB) of tellurium nanowires (TeNWs) to determine how this barrier height influences the electrical conductivity, Seebeck coefficient, and power factor. We find that for both small (0.08 eV) and large (0.88 eV) energy barriers between the transport states of P3HT and TeNWs, the power factors of the composite materials exceed that of both pure materials. In an effort to determine if these enhancements are due to energy filtering, we compare the experimentally measured Seebeck coefficients to a model of two materials in parallel and in series. Based on these modeled Seebeck coefficients, we find that energy filtering is not necessary to explain the increasing Seebeck coefficient with increasing TeNW concentration. Furthermore, this model predicts that even larger power factor increases over the pure materials are possible, and suggests that the impact of energy filtering on the TE performance of organic-inorganic composites is significantly less than previous work has suggested.

3.2 Results and Discussion:

3.2.1 Energy Levels of P3HT and TeNWs

We explored two methods for altering the energy level alignment between P3HT and TeNWs. Initially, we aimed to control the TeNWs work function and valence band energy through the surface ligands. The two primary synthesis methods investigated included polyvinylpyrrolidone (PVP) or cetyltrimethylammonium bromide (CTAB) as stabilizing surfactants. With both surfactants the work functions, as measured with ultraviolet photoelectron spectroscopy (UPS), remained between 3.6 eV (PVP/TeNWs) and 4.22 eV (CTAB/TeNWs) for the TeNW films, where the highest work function of 4.22 eV is still lower than that of lightly p-doped P3HT. These work functions are both significantly lower than the previously reported value of 4.95 eV.[38] We also investigated using ligand exchange reactions to further increase the work function, but this strategy did not yield significant increases. Based on the more similar ionization energy of P3HT with CTAB stabilized TeNWs, we utilized CTAB stabilized TeNWs throughout this work.

To further explore why our measured work functions are 0.7 eV lower than those previously reported, we prepared pure tellurium thin films through thermal evaporation and investigated the films with UPS before and after argon-ion sputter cleaning, as shown in Figure 3.2a. The work functions (WF) of the samples are determined from the equation WF = $h\upsilon$ – SECO, where $h\upsilon$ is 10.2 eV and SECO is the secondary electron cut-off. The ionization energy was determined by the equation IE = WF + valence band (or HOMO) onset. The procedures used for determining the SECO, valence band, and HOMO onset for the various samples are described in the experimental section. We measure a work function of 4.78 eV for sputter-cleaned Te films, which is in the range of previously reported values that range from 4.73 eV to 4.95 eV.[105,106,107] The differing values reported in the literature may arise due to the nature of the surface and the crystallographic orientations.[108,109,110,111] It is also likely that the value of 4.95 eV reported for TeNWs was actually for planar tellurium.[106] The difference in work functions between the TeNWs and planar tellurium films highlights the importance of performing UPS measurements on the nanowires, as surface states, surface ligands, and quantum confinement effects can all lead to significant variations between the energetics of bulk materials and nanomaterials. As shown in Figure 3.2b, the valence band onset of tellurium nanowires and planar tellurium is gradual, which is in agreement with a gradual increase in the density of states as predicted with theoretical calculations.[112]. Based on this onset and work function, the valence band energy for our TeNWs is 4.52 eV.

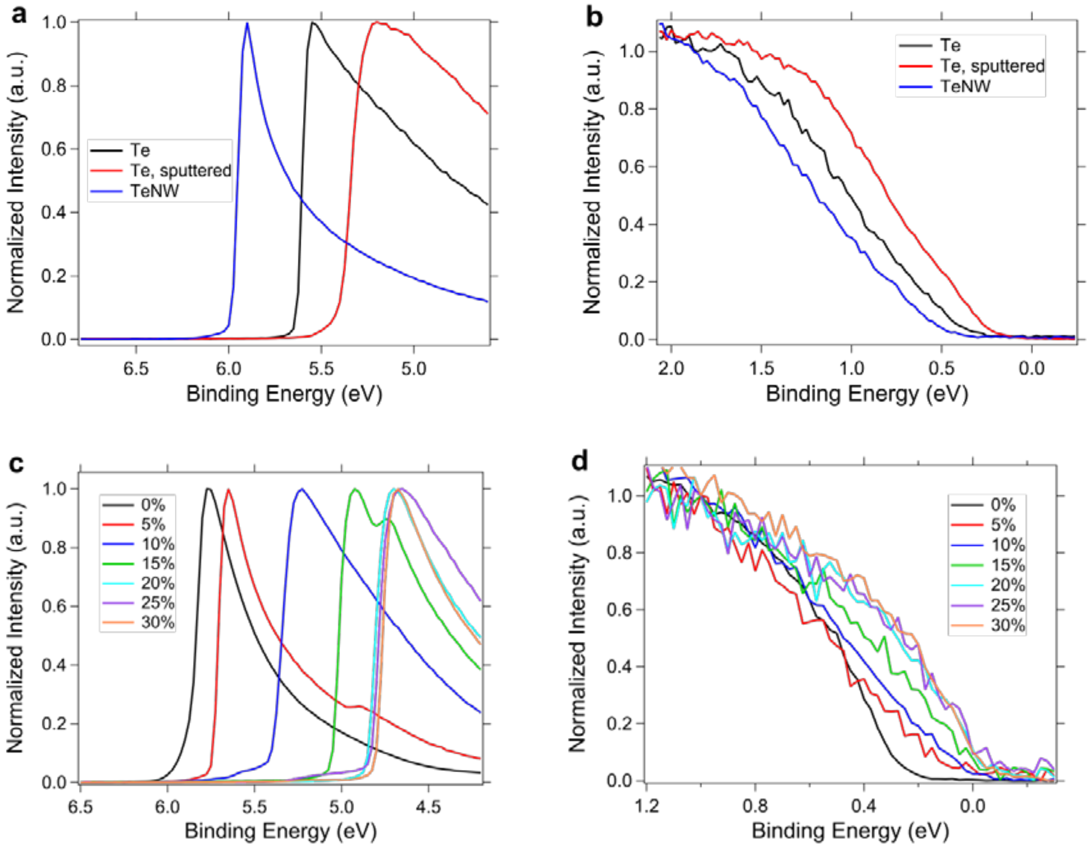

Figure 3.2 UPS spectra measured with a 10.2 eV H Lyman-α lamp of as prepared and sputter-cleaned tellurium films and tellurium nanowires (a,b) and P3HT with 0 to 30% $FeCl_3$ (c,d). The SECO regions are shown in a) and c) and the valence band or HOMO onset regions are shown in b) and d).

The work function and ionization energies of P3HT with varying amounts of the p-type dopant ferric chloride were measured, as shown in Figure 3.2c and 3.2d. As the concentration of $FeCl_3$ increases, the HOMO onset of P3HT shifts closer towards the Fermi energy, which is the expected behavior for p-type doping. For 0 and 5% doping (by wt.) the ionization energy (IE) of P3HT remains the same, as the work function shift parallels that of the HOMO onset. However, at higher doping concentrations the work function continues to increase to a value of 5.39 eV, which results in a substantial increase in the IE to 5.40 eV. Similar increases in IE with increasing dopant concentration were previously observed, though to a lesser extent.[113,114] The accessible range of IEs for P3HT through changing the dopant ratio is from 4.60 to 5.40 eV, which is 0.08 to 0.88 eV higher than the IE of our TeNWs. The ionization energies are used to approximate the barrier heights since the ionization energies more accurately reflect the transport edge, as many of these semiconducting materials do not have mobile states present at the Fermi energy. Further insight into the doping process is evidenced by UV-Vis absorbance measurements, which show the P3HT polaron absorbance band with a maximum at *ca.* 800 nm increasing and the neutral absorbance band with a maximum at *ca.* 520 nm decreasing as the concentration of $FeCl_3$ increases from 0 to 30% (Figure 3.3).[40]

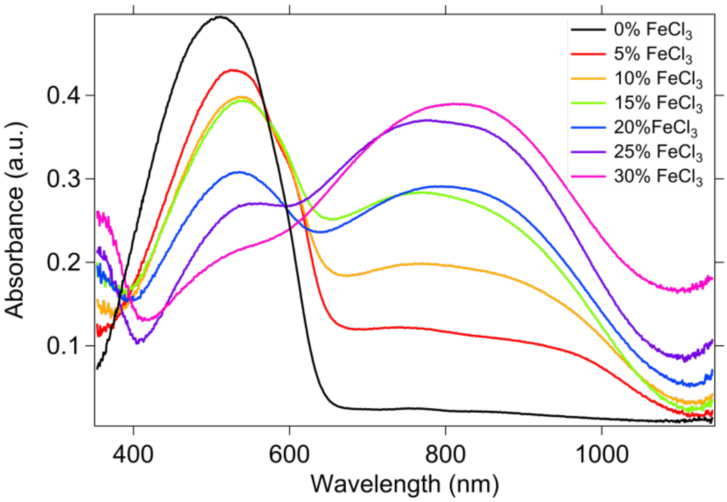

Figure 3.3 UV-VIS absorbance spectra of 5 to 30% $FeCl_3$ doped P3HT.

As discussed in the introduction, a proper interfacial energy barrier in nanocomposites can hinder the transport of low-energy carriers and facilitate high-energy carrier transport, which will enhance the Seebeck coefficient. The transport energy levels (i.e., the IEs) are depicted for TeNWs and P3HT in Figure 3.4. In our experiments, we focus on two different interfacial energy barriers, 0.08 and 0.88 eV. These barriers are obtained for P3HT:TeNW composites with 5 and 30% $FeCl_3$, with a barrier of 0.08 eV for 5% $FeCl_3$ and 0.88 eV for 30% $FeCl_3$. These interfacial energy barriers may change slightly based on the interfacial interactions present in the films, but these changes should be minor relative to the large 0.8 eV difference in barrier heights. UPS measurements of 5 and 30% $FeCl_3$ doped P3HT:TeNW blends are displayed in Figure 3.5. The UPS spectra shown in Figure 3.5 support the general trend in the energy barrier, i.e. it is significantly larger for the 30% $FeCl_3$ doped samples than the 5% doped samples. If we look at the spectra for the 50% TeNW blends, we see that the work functions and IEs are within 0.2 eV of their values for pure $FeCl_3$ doped P3HT. At 50% TeNW loading the TeNWs are nearly completely coated with P3HT, as the SEM images included in the main manuscript show that most of the TeNWs are coated even at 90% TeNW loading. Thus, the UPS results for the 50% TeNW films can be considered as analogous to TeNWs covered with a thin layer of P3HT. To illustrate how the interfacial energy landscape and barrier to charge transfer arises, we show the work function (blue lines) and IE (green lines) of pure TeNW films and pure 30% doped $FeCl_3$ films. As the P3HT is brought into contact with the TeNWs, electrons will transfer from the higher energy occupied electronic states (i.e. the states closer to the vacuum level) in the TeNWs to the available lower energy unoccupied electronic states in P3HT (P3HT is highly doped and thus there are many holes that can be filled), as indicated by the red arrow. As a result of this charge redistribution, the TeNW valence band bends towards the Fermi level at the TeNW/P3HT interface while the P3HT HOMO energy shifts away from the Fermi level at the TeNW/P3HT interface. Accompanying this charge redistribution is an upwards shift in the vacuum level, giving rise to the resulting energy landscape shown in Figure 3.5e. Assuming the starting work function (4.22) and IE for the pure TeNWs is the same in both the 5 and 30% $FeCl_3$ doped samples, and the work function of the 50% TeNW samples are 4.4 and 5.2 eV for the 5 and 30% $FeCl_3$ doped samples, it is apparent that the energy barrier for charge transfer must be significantly greater for the sample with 30% $FeCl_3$. Typically, the theoretical effective energy barrier for maximum enhancements in the power factor is ≤0.2 eV.[50,53] Based on these previous calculations, we would expect to observe greater enhancements in the power factor for the 5% $FeCl_3$ doped P3HT:TeNW composites.

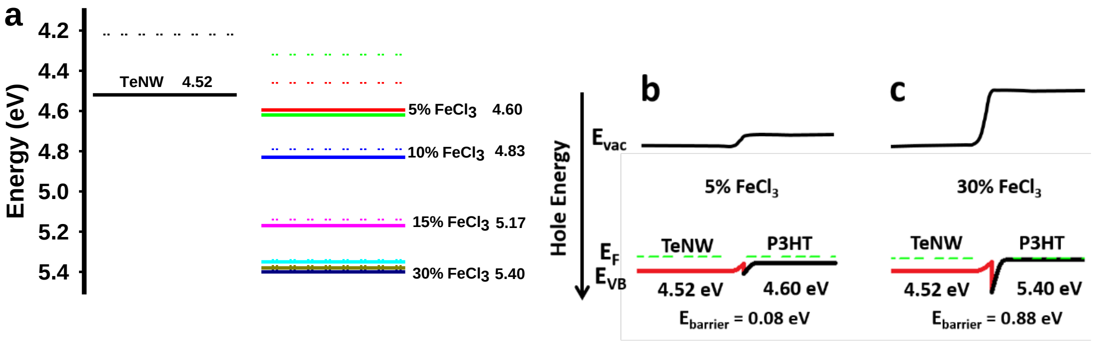

Figure 3.4 (a) Work function (dashed lines) and IE (solid lines) of TeNWs and 0, 5, 10, 15, 20, 25, and 30% $FeCl_3$ doped P3HT. Energy diagrams of 5% (b) and 30% (c) $FeCl_3$ doped P3HT:TeNW composites.

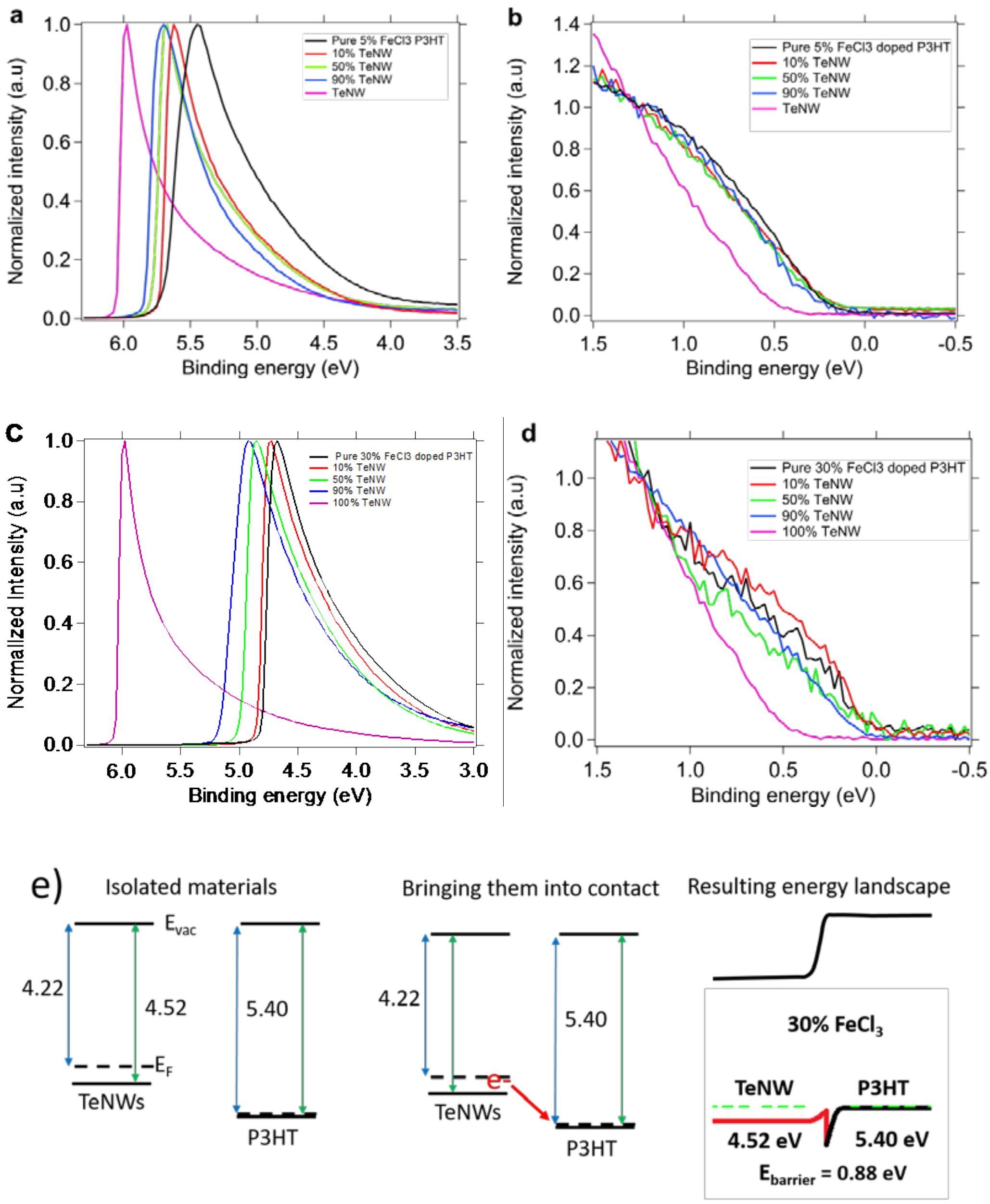

Figure 3.5 UPS spectra showing the secondary electron cut-off region (a, c) and the HOMO onset region (b, d) for 5 (a, b) and 30% (c,d) $FeCl_3$ doped blends with varying TeNW concentration. The origin of the energy landscape is shown in (e). E_{vac} and E_F are the vacuum and Fermi levels, respectively.

Activation energy measurements provide another means of qualitatively analyzing the barrier heights. The activation energies, as shown in Figure 3.6, of P3HT:TeNW blends with 5 and 30% $FeCl_3$ were extracted through fitting temperature dependent electrical conductivity measurements with the Arrhenius equation. These measurements were repeated twice, and in the first measurement the samples were exposed to air as was necessary for sample loading in the cryogenic probe station, a silver paste was applied, and the samples were cooled to 77 K. Following warming to room temperature, the sample showed up to 120 times lower electrical conductivity values than originally measured. These measurements were repeated over a smaller temperature range in our nitrogen filled glovebox with a linear four-point probe and a thermoelectric module used for temperature control. The significant difference between these measurements is apparent in Figure 3.6d. The activation energies extracted through measurements performed in our glovebox, as shown in Figure 3.6a, show that the activation energies of the 5% $FeCl_3$ doped samples decrease as the TeNW loading is increased, while those of the 30% $FeCl_3$ doped samples increase as the TeNW loading is increased. The activation energy for the 5% $FeCl_3$ doped blend at 90% TeNW loading is 15% lower than the pure 5% $FeCl_3$ doped P3HT sample and 39% lower than the pure TeNW sample, which supports that the barrier for charge transport between the TeNWs and P3HT must be small. Although qualitatively these trends may be interpreted to support that the barrier height is smaller for the 5% $FeCl_3$ doped sample, the fact that the starting activation energy for the 30% $FeCl_3$ doped P3HT sample is an order of magnitude lower than the 5% $FeCl_3$ doped P3HT sample (10 meV vs. 100 meV) makes it difficult to draw definitive conclusions about the barrier heights from the activation energies.

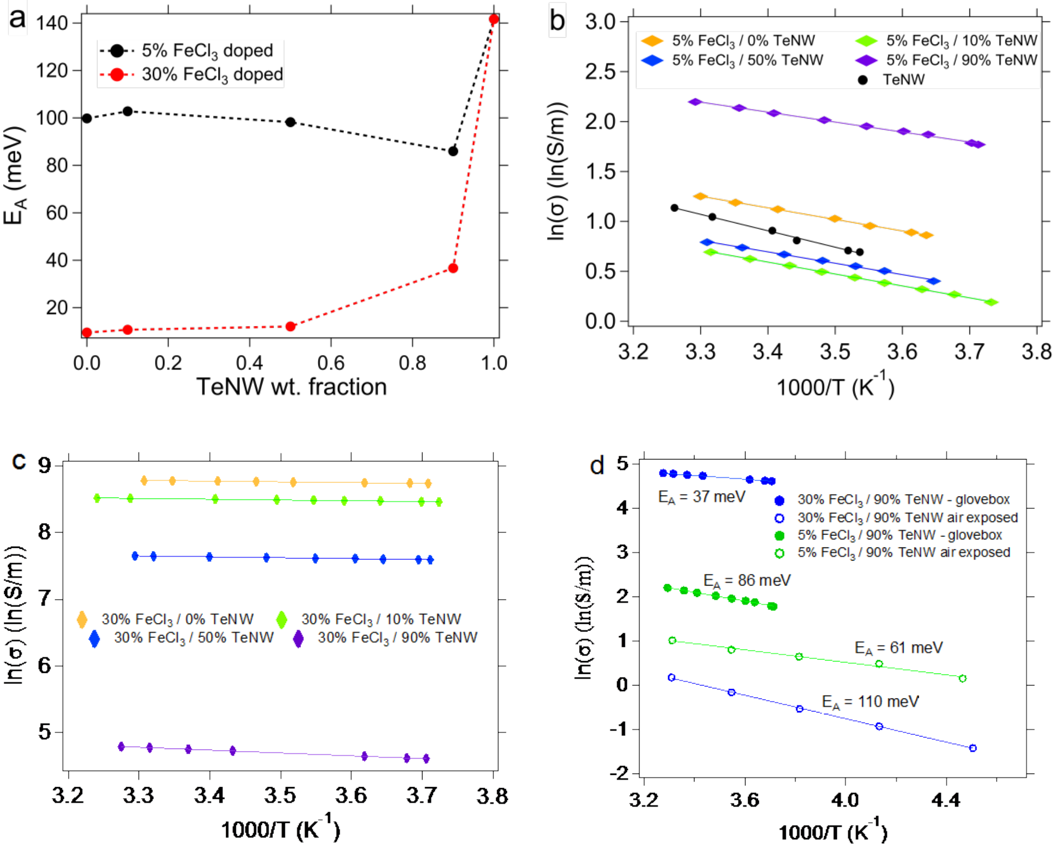

Figure 3.6 Activation energies for samples measured inside of our glovebox (a), temperature dependent electrical conductivity plots (b and c) measured inside of our glovebox and used to extract the activation energies for the P3HT:TeNW blends shown in a, and a comparison of the temperature dependent electrical conductivity measurements for 90% TeNW films performed in a probe station and in our glovebox (d), where the probe station measurements (labeled air exposed) involved unavoidable exposure to the ambient atmosphere and cooling to 77 K before beginning the measurements.

3.2.2 Film Morphology and TE Characteristics of P3HT:TeNW Composites

Tellurium nanowires with diameters of 10 to 20 nm and lengths of 1 to 3 µm (see Figure 3.7 for SEM and TEM images) were thoroughly mixed in solution with FeCl$_3$ doped P3HT by following the procedures detailed in the experimental section. Both the 5 and 30% FeCl$_3$ doped films show similar morphologies with no significant nanowire or polymer aggregation observed, as shown by the SEM images in Figure 3.8 for the films with 80% (by wt.) TeNW concentration. Film thicknesses of the

P3HT:TeNW nanocomposites were typically 4 to 8 µm. The sample thicknesses were relatively uniform for a given film, with standard deviations of multiple thickness measurements for each sample varying from 1 to 9% of the total film thickness.

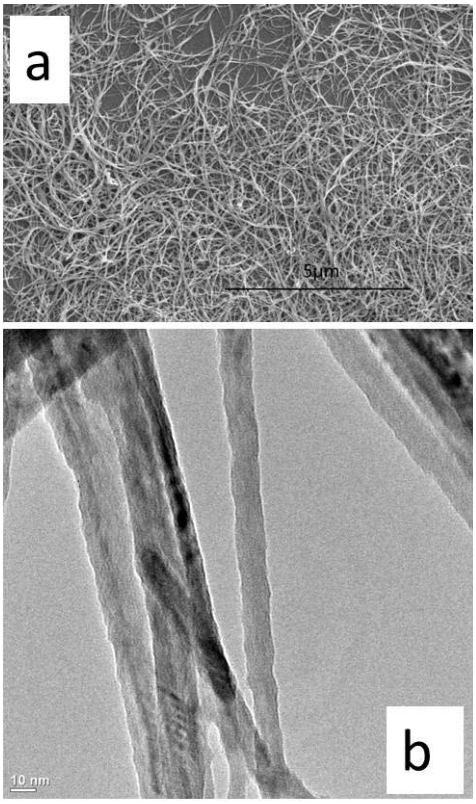

Figure 3.7 SEM (a) and TEM (b) images of the CTAB stabilized tellurium nanowires utilized in this work.

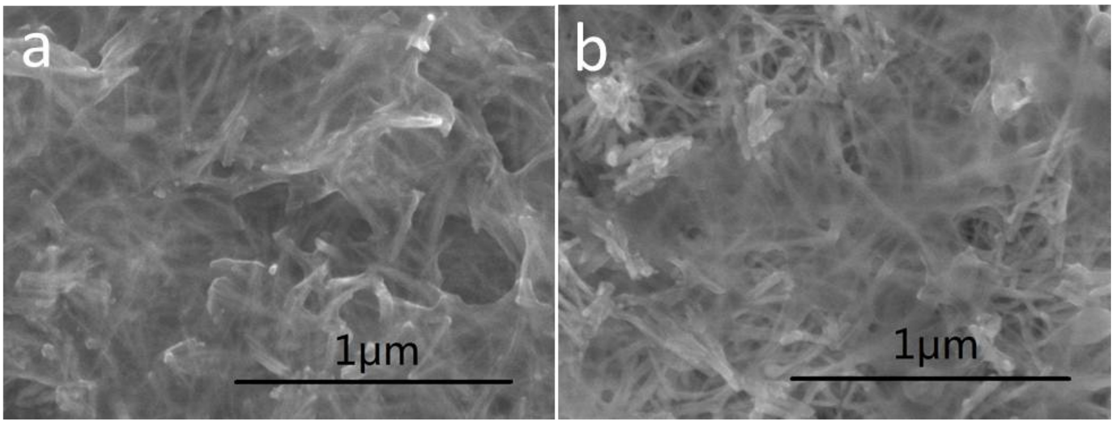

Figure 3.8 Scanning electron microscope (SEM) images of TeNW-P3HT nanocomposites with 80 wt. % TeNWs and 5% (a) and 30% (b) $FeCl_3$ doped P3HT.

The Seebeck coefficients, electrical conductivities, and power factors are displayed in Figure 3.9 for the 5 and 30% $FeCl_3$ doped P3HT:TeNW films with varying concentrations of TeNWs. The Seebeck measurements were performed using recommended film geometries and with a pure bismuth film serving as a thermometer,[115] as detailed in the experimental section. For the 5% $FeCl_3$ doped samples (Figure 3.9a), the Seebeck coefficient increases from 172.6 μV/K to 758 μV/K as the TeNW concentration increases from 0 to 100%. The electrical conductivity first decreases slightly from 3.61 S/m (0% TeNWs) to 1.64 S/m (50% TeNWs), then increases to 20.45 S/m (80% TeNWs), before dropping to 1.65 S/m (100% TeNWs). As a result, the 5% $FeCl_3$ doped composite with 80% TeNWs has a power factor that is nearly an order of magnitude higher than either of the pure 5% $FeCl_3$ doped P3HT and two times higher than TeNWs. For the 30% $FeCl_3$ doped P3HT:TeNW composites, the Seebeck coefficient increases from 31 μV/K to 758 μV/K and σ gradually decreases from 6661 to 1.65 S/m as the TeNW concentration increases from 0 to 100% (Figure 3.9b). These trends result in the 30% $FeCl_3$ doped composite with 50% TeNWs displaying a 49% higher power factor than the 30% $FeCl_3$ doped P3HT sample with 0% TeNWs. In general, these data confirm that these composites provide an effective means to increase power factors beyond those of the pure components.

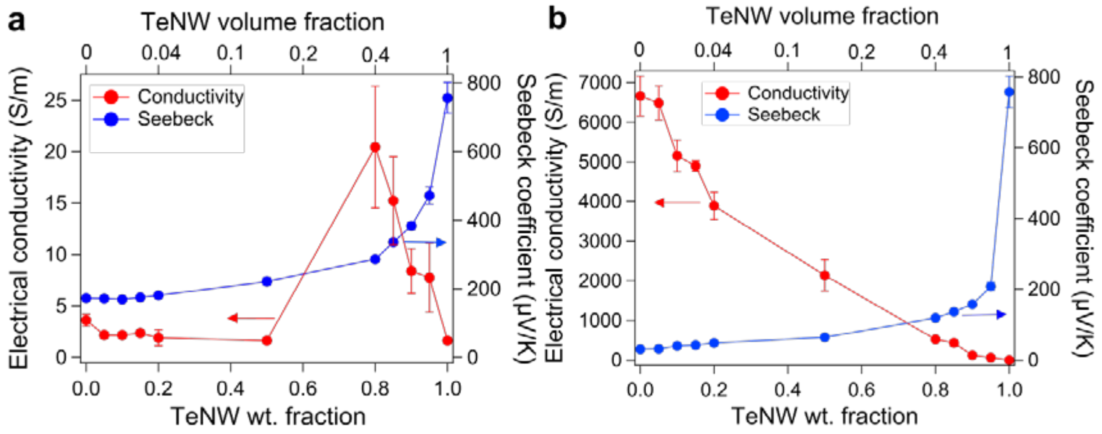

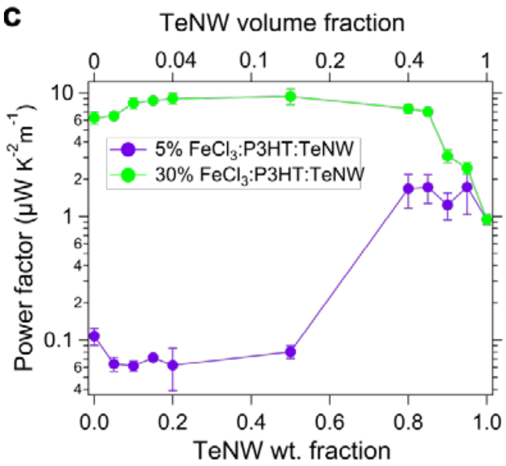

Figure 3.9 Seebeck coefficients and electrical conductivities for 5% (a) and 30% (b) $FeCl_3$ doped P3HT:TeNW films, and power factors for these series of materials (c).

The electrical conductivity that we measure for the P3HT film with 30% $FeCl_3$ is larger than typically measured by other groups, where σ commonly ranges from 700 to 2,100 S/m for P3HT that is heavily doped with $FeCl_3$.[28,116] Our experiments indicate that the primary reason for the higher electrical conductivity obtained in our laboratory is due to the fabrication of our samples in a nitrogen filled glovebox (<1ppm H_2O and <1ppm O_2). In our experiments, the electrical conductivities of 30% $FeCl_3$ doped P3HT films prepared inside our glovebox were more than three times greater than identical films prepared completely in ambient atmosphere. Another report also shows a similarly high electrical conductivity of 6,300 S/m for $FeCl_3$ doped P3HT, where doping was carried out by P3HT film exposure to $FeCl_3$ vapor under vacuum.[40]

3.2.3 Seebeck Coefficients of the P3HT:TeNW Nanocomposites

For both the 5 and 30% $FeCl_3$ doped P3HT-TeNW composites, the Seebeck coefficient increases as the TeNW concentration increases from 0 to 100%. One explanation for the increasing Seebeck coefficient with increasing TeNW loading, which has been proposed by other groups for similar materials, is the energy filtering effect.[28,38,86,87] In traditional systems with small nanoparticles in a semiconducting matrix, signatures of energy filtering include a decrease in the electrical conductivity and an increase in the Seebeck coefficient. For the 5% $FeCl_3$ doped composites, which have a 0.08 eV barrier between the transport states in P3HT and the TeNWs, we do not see a statistically significant decrease in σ, and α remains fairly constant at low nanowire loadings. Furthermore, the Seebeck coefficient never exceeds that of the pure TeNWs. In the 30% $FeCl_3$ doped composites, the energy barrier between the transport states is higher than the predicted range where beneficial energy filtering effects can be observed. As with the 5% $FeCl_3$ sample, the 30% $FeCl_3$ doped samples do not show a significant increase in α at low TeNW loadings, and the Seebeck coefficient never exceeds that of the pure TeNWs. This combination of observations suggests that the increased power factors may not be due to energy filtering.

To further determine if energy filtering is necessary to explain the measured Seebeck coefficients, we applied simple models developed for composite materials that do not account for energy filtering.[117] These models are based on two materials in parallel, two materials in series, and linear combinations of these series and parallel models. The models were effectively applied by Gelbstein in two phase Sn/SnTe alloys to evaluate the correlation between thermoelectric properties and microstructure of phases.[117] With a similar two phase structure in the P3HT:TeNW composites, we expect that if energy filtering effects are minimal, then our measured Seebeck coefficients will also fit these models, as described by **Equations (1)** and **(2)**.[117] On the other hand, if energy filtering effects are significant, then we expect that the Seebeck coefficients will exceed those predicted by the model.

$$\alpha_{eff}(parallel) = \frac{\alpha_1\sigma_1 x_1 + \alpha_2\sigma_2(1-x_1)}{\sigma_2(1-x_1)+\sigma_1 x_1} \qquad (1)$$

$$\alpha_{eff}(series) = \frac{\alpha_1\kappa_2 x_1 + \alpha_2\kappa_1(1-x_1)}{\kappa_1(1-x_1)+\kappa_2 x_1} \qquad (2)$$

Here, the subscript 1 is used to indicate values for P3HT, with x_1 being the volume fraction of $FeCl_3$ doped P3HT, the subscript 2 indicates values for TeNWs, and κ for doped P3HT and TeNWs are taken from the literature to be 0.45 and 0.28 W $k^{-1}m^{-1}$.[28,38] The parallel model represents the scenario where charge-carriers are transported through either P3HT or TeNWs, with minimal transport between the two components. On the other hand, the series model represents a situation where the charge carriers are constantly transferring between the two phases. Between these two extremes lie all the intermediate situations with varying degrees of transport between phases. The Seebeck coefficient of this combined transport model is given in **Equation (3)**, where y is the fraction of the parallel model.

$$\alpha_{eff} = \frac{[\alpha_1\sigma_1 x_1 + \alpha_2\sigma_2(1-x_1)]}{\sigma_2(1-x_1)+\sigma_1 x_1}\,y + \frac{[\alpha_1\kappa_2 x_1 + \alpha_2\kappa_1(1-x_1)]}{\kappa_1(1-x_1)+\kappa_2 x_1}(1-y) \qquad (3)$$

The calculated α_{eff} values are shown in Figure 3.10 along with the experimentally measured Seebeck coefficients. As y increases from 0 to 1, the Seebeck coefficients gradually decrease in both 5 and 30% systems. In other words, the Seebeck coefficient increases as the contribution of series-like transport increases. This phenomenon can be explained by considering that the Seebeck coefficient is determined by the average amount of entropy transported per charge carrier. In a parallel model, the higher conductivity phase will contribute more to the electrical conductivity and thus also exert a stronger influence on the Seebeck coefficient. This trend is most apparent in the 30% $FeCl_3$ doped samples, where the electrical conductivity of P3HT is 3 orders of magnitude higher than the TeNWs. As a result, in a parallel model, the Seebeck coefficient is determined almost entirely by P3HT. By contrast, in a series model the charges are transported through both materials and thus they contribute more equally to the Seebeck coefficient. Hence, the Seebeck coefficient is higher for the series model than the parallel model.

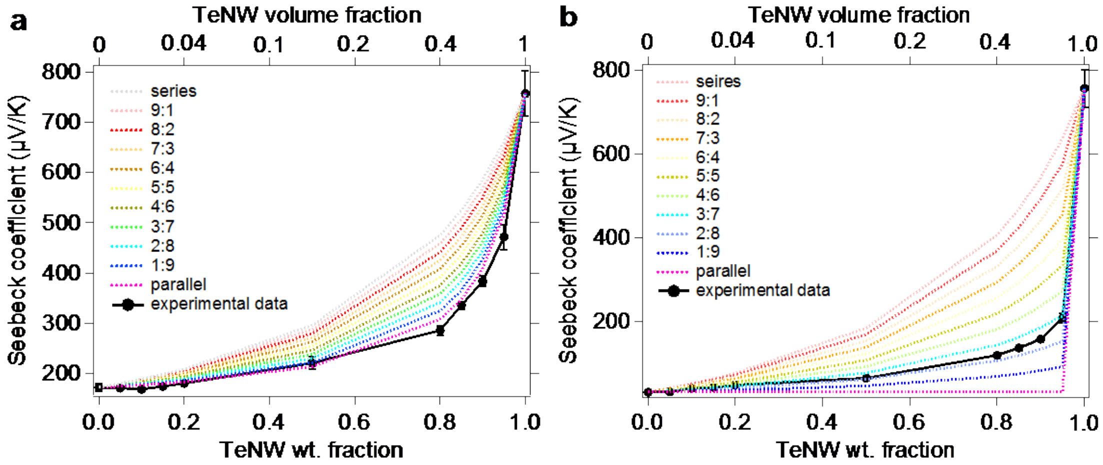

Figure 3.10 Calculated Seebeck coefficients using various ratios of the series and parallel models (series:parallel) along with the experimentally measured Seebeck coefficients for a) 5% and b) 30% $FeCl_3$ doped P3HT:TeNW composites.

The fact that the Seebeck coefficients for both blends fit relatively well with these series and parallel models indicates that energy filtering is not necessary to explain the variation in Seebeck coefficients in the composites. Actually, in the case of the 5% $FeCl_3$ series, where the energy offset appeared ideal for observing the energy filtering effect, the Seebeck coefficients for the composites are actually slightly lower than what these models would predict. With this in mind, it appears that energy filtering is not responsible for the variation in the Seebeck coefficient in these composites.

Surprisingly, the 5% $FeCl_3$ doped sample series agrees most closely with a 100% parallel transport model, while the 30% $FeCl_3$ doped sample series agrees best with a model where 20 to 30% of the contribution is from a series connected model. The models are fairly robust to variations in both σ and κ, with the 5% series showing minimal changes in the model fit with varying κ and the 30% series showing minimal changes in the fit with varying σ. The models and data are shown in Figures 3.11 and 3.12 to show how variations in σ and κ influence the Seebeck coefficient predicted by the model. The necessity of using this combined parallel and series model is especially apparent for the 30% blend at TeNW loadings between 80 and 95 wt. %, where the measured Seebeck coefficients are 4 to 7 times greater than those predicted based purely on the parallel model, and 3 to 4 times less than those predicted based purely on the series model.

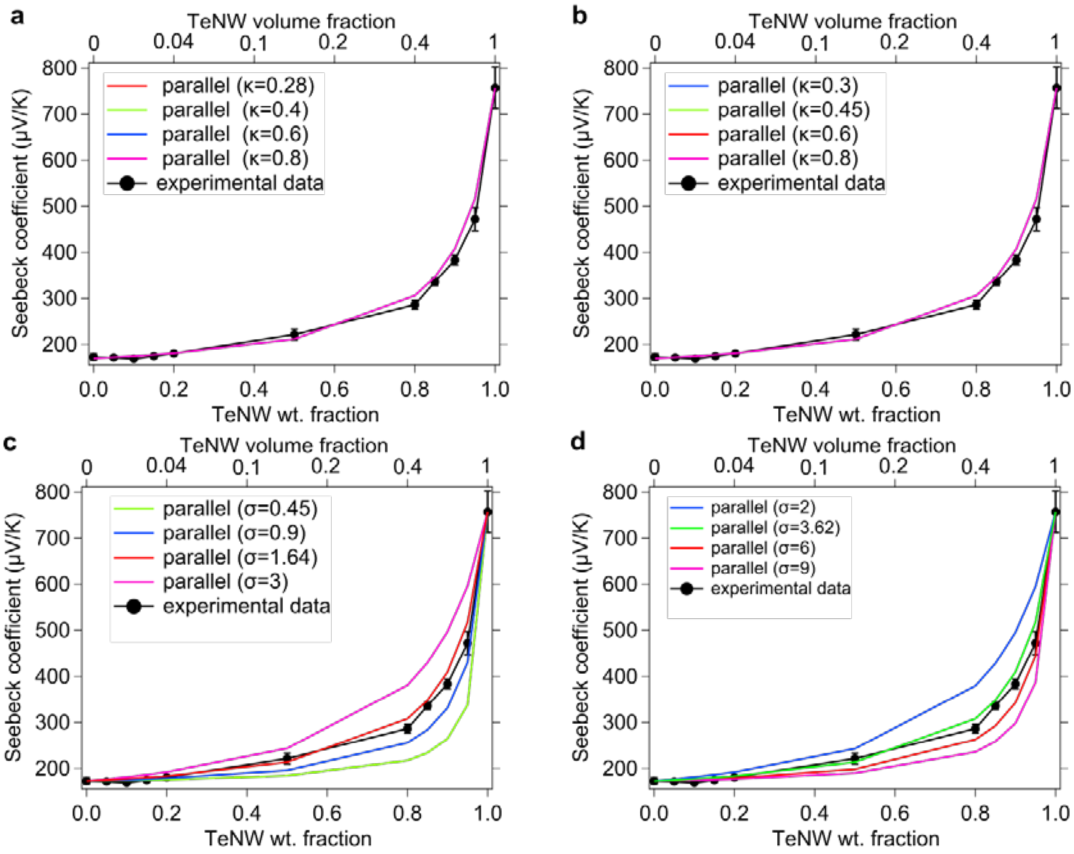

Figure 3.11 5% $FeCl_3$ doped P3HT blends with varying TeNW loading showing how variations in the thermal conductivity (a,b) and electrical conductivity (c,d) of the TeNW (a,c) and P3HT (b,d) components influence how the pure parallel model fits the experimental data.

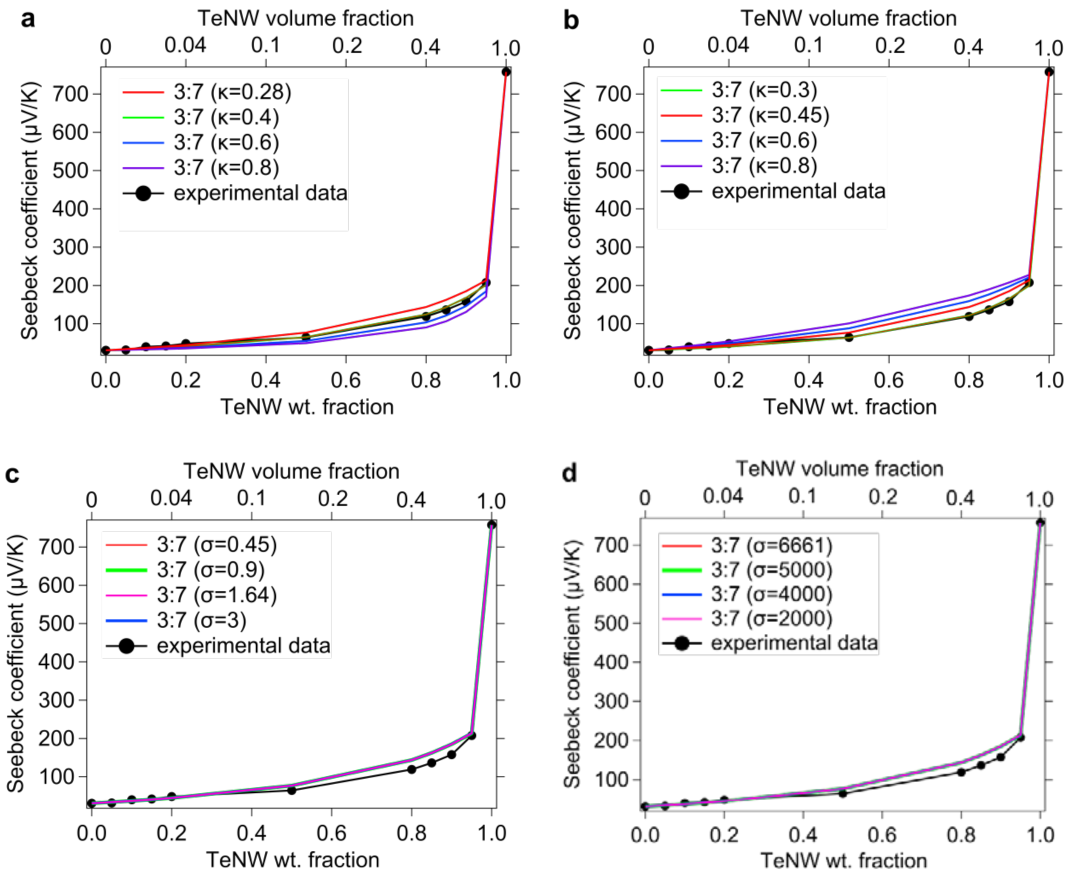

Figure 3.12 30% $FeCl_3$ doped P3HT blends with varying TeNW loading showing how variations in the thermal conductivity (a,b) and electrical conductivity (c,d) of the TeNW (a,c) and P3HT (b,d) components influence how the 3:7 series:parallel model fits the experimental data.

The significant contribution of series based transport in the 30% $FeCl_3$ doped sample series suggests that despite the greater energy barrier between the TeNWs and P3HT, the charges still move between the TeNWs and P3HT. This trend may potentially be explained by the thinner barrier at the P3HT/TeNW junctions for the 30% $FeCl_3$ doped samples. Based on previously reported equations for semiconductor junctions and literature reported values of carrier densities, as detailed in (Equation 4), the barrier width for the 5 and 30% $FeCl_3$ doped samples will be 5 and 3 nm, respectively. These thin barrier widths are within the tunneling regime, and it has been shown that five-fold increases in doping concentration can lead to changes in contact resistance by multiple orders of magnitude.[118,119] Changes in interfacial charge transfer rates with doping concentration may explain why the more highly doped samples display a significant contribution of series-based transport, despite the significantly higher interfacial energy barrier.

$$W_D = \left[\frac{2N_{NW}\varepsilon_P\varepsilon_{NW}V_{bi}}{qN_P(\varepsilon_P N_P+\varepsilon_{NW}N_{NW})}\right]^{1/2} \qquad (4)$$

Where V_{bi} is the built-in potential at equilibrium, N_{NW} and N_P are the charge-carrier concentrations in the TeNWs and P3HT, respectively, ε_{NW} and ε_P are the dielectric constants of Te and P3HT, W_D is the depletion width, and q is the elementary charge. In these calculations we use V_{bi}=0.08 V (5% $FeCl_3$ doped) and 0.88 V (30% $FeCl_3$ doped); $N_{NW}=1\times10^{18}$ cm^{-3};[38,120] $N_P=2.7\times10^{19}$ cm^{-3} (5% $FeCl_3$ doped) and 1.6×10^{20} cm^{-3} (30% $FeCl_3$ doped);[28] $\varepsilon_P=3.1*10^{-11}(CV^{-1}cm^{-1})$;[121,122] $\varepsilon_{NW}=2.43*10^{-10}(CV^{-1}cm^{-1})$;[123,124] and $q=1.6*10^{-19}$ C.[125]

3.2.4 Electrical Conductivity of the P3HT:TeNW Composites

Intriguingly, the electrical conductivity exhibits a sharp peak at 90% TeNW concentration in the 5% $FeCl_3$ doped P3HT:TeNW composites that is nearly an order of magnitude higher than either of the individual components, as shown in Figure 3.9a. Coates *et al.* observed a similar peak in TeNW-PEDOT:PSS composite films, which they attributed to interfacial interactions in polymer-nanocrystal systems that result in a high-conductivity interfacial polymer phase.[96] Another potential explanation is that the presence of the polymer significantly improves charge transfer between the nanowires. Here, we know that the junction resistance between the nanowires can be large and limit the overall electrical conductivity of pure nanowire films.[56] For example, the electrical conductivity of TeNW films is 1.65 S/m, while we measured the electrical conductivity of planar tellurium to be 1000 S/m, which is in the range of previously reported values.[126,127] We hypothesize that charge transfer between the nanowires can occur through the polymer. This polymer mediated charge-transfer between nanowires could potentially explain the increased electrical conductivity with high nanowire loadings in the 5% $FeCl_3$ doped composites, and is also consistent with the lower activation energy observed for the 5% $FeCl_3$ doped P3HT sample with 80% TeNW concentration by weight.

The electrical conductivity of the 30% $FeCl_3$ doped composites gradually decreases as the TeNW concentration increases and does not exhibit a peak in σ as the 5% samples did. This is likely because the 30% doped P3HT has a much larger conductivity (6662 S/m) than even bulk tellurium, and even with high nanowire loadings the majority of charge transport still occurs through the P3HT phase. For example, at 95% TeNWs the 30% $FeCl_3$ doped film displays an electrical conductivity of 64 S/m, as opposed to the 20.45 S/m maximum electrical conductivity observed for the 80% P3HT:TeNW composite with 5% $FeCl_3$.

The electrical conductivities of the blends were calculated using similar parallel and series connected composite models as applied to the Seebeck coefficients, as listed Equations 6 – 7. The electrical conductivities of both the 5 and 30% $FeCl_3$ doped samples do not fit well with the series and parallel models, as illustrated in Figure 13. For the 5% blend, the anomalous increase in electrical conductivity for high TeNW concentrations will not be predicted by any micro- or macro-scale model. Here, the conductivity increase most likely arises from nano- to molecular-scale transport properties, as previously discussed. The 30% $FeCl_3$ composites also do not follow a particular trend line predicted by the model, but all points do fall within the bounds of the parallel and series connected models. Potential explanations for the deviations from the predicted electrical conductivities include both interfacial charge-transfer effects and changes in the P3HT morphology upon increasing TeNW concentration.

$$\sigma_{eff}(parallel) = x_1\sigma_1 + (1-x_1)\sigma_2 \qquad (5)$$

$$\sigma_{eff}(series) = \frac{\sigma_1\sigma_2}{x_1\sigma_2 + (1-x_1)\sigma_1} \qquad (6)$$

$$\sigma_{eff} = (x_1\sigma_1 + (1-x_1)\sigma_2)y + \frac{\sigma_1\sigma_2(1-y)}{x_1\sigma_2 + (1-x_1)\sigma_1} \qquad (7)$$

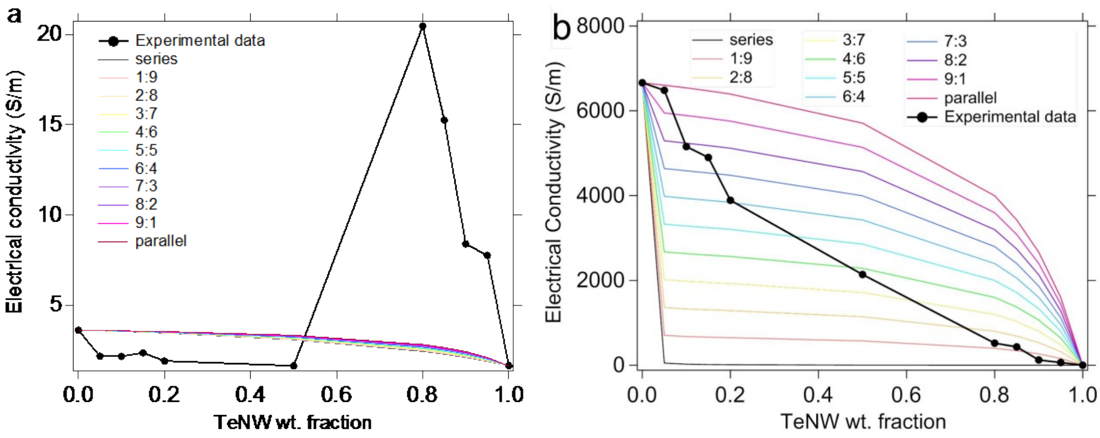

Figure 3.13 Combined series and parallel models of calculated and experimentally measured electrical conductivity for a) 5% $FeCl_3$ and b) 30% $FeCl_3$ doped P3HT:TeNW composites.

The calculated curves for σ of the 30% $FeCl_3$ doped samples indicate that σ may be significantly increased at higher TeNW concentrations if the sample followed a trend line with a higher weighting of the parallel conductivity. Furthermore, as highlighted in Figure 3.13, if σ of the 30% $FeCl_3$ doped composites followed the behavior predicted by the 2:8 or 3:7 series:parallel model, then the power factor may be an order of magnitude higher than that obtained experimentally in this work (Figure 3.14). This finding is consistent with theoretical predictions of Feng and Ellis,[128] where a high σ, low α polymer blended with a low σ, high α polymer can yield significantly higher TE performance than either of the pure polymers. This previous work, combined with our observed and modeled data, demonstrates that high-performing nanocomposite TE materials should be reachable even without energy filtering.

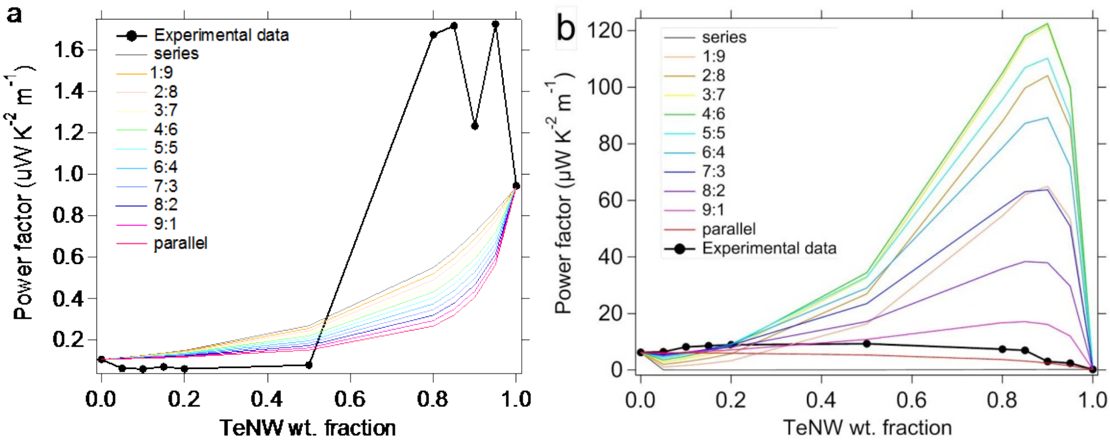

Figure 3.14 Combined series and parallel models of calculated and experimental power factor for a) 5% $FeCl_3$ and b) 30% $FeCl_3$ doped P3HT:TeNW composites.

3.3 Conclusion

The P3HT:TeNW nanocomposites investigated demonstrate higher power factors than both of the pure components, regardless of whether a small or large interfacial energy barrier exists. The power factors of the 5 and 30% $FeCl_3$ doped nanocomposites are 2 and 1.4 times higher, respectively, than the pure component with the higher power factor. Energy filtering, which is a commonly adopted explanation for power factor enhancements in nanocomposites, does not appear to be playing a significant role. Rather, the Seebeck coefficient is well-described by a model for parallel and series connected composite materials. Furthermore, these models based on the effective medium theory predict significantly larger increases in the power factor. To enable these predicted increases, the electrical transport behavior in the composite must be manipulated to create a material that has significant contributions from both series (transport between heterogeneous phases) and parallel (transport between homogeneous phases) transport. The anomalous increase in the electrical conductivity in the 5% $FeCl_3$ doped samples further highlights how understanding and manipulating the nano- to molecular-scale charge transfer processes may provide a route to higher performing TE nanocomposites.

3.4 Experimental Details

Materials

L-ascorbic acid (acs grade, BDH); sodium tellurite(IV) (alfa aesar, 99.5% metals basis); tellurium(IV) oxide (BTC, 99.99% metal basis); polyvinylpyrrolidone (M. W. 40,000) (Alfa Aesar); poly(3-hexylthiophene-2,5-diyl) (rieke metals, regioregular, electronic grade); iron(III) chloride (anhydrous, 98%, crystalline, alfa aesar); chloroform (anhydrous, driSolv); cetyltrimethylammonium bromide (>98.0%, TCI); ethylene glycol (99%, alfa aesar); hydrazine monohydrate, (98+%, alfa aesar); bismuth(99.99%, kurt J. lesker); tellurium shot (99.9999% metal basis, alfa aesar).

TeNWs synthesis

TeNWs were synthesized following literature procedures.[129,130] Briefly, 3.75g L-ascorbic acid and 0.375g cetyltrimethylammonium bromide (CTAB) were added and stirred in 150 ml deionized water. Then 0.195 g sodium tellurite was added and vigorously stirred. The mixture was heated to 90 °C in an oil bath and kept for 20 hours. The solution cooled down to room temperature and was washed three times with deionized water and ethanol.[129] Finally, the CTAB/TeNW powder was dried in a vacuum oven overnight and stored in the nitrogen-filled glovebox until further use. PVP/TeNWs were synthesized by adding 0.8344 g PVP, 0.4 g TeO_2, and 0.7520 g NaOH in 27 ml ethylene glycol solution under stirring. The solution was heated to 120 °C in an oil bath and rapidly injected into 1.5ml $N_2H_4 \cdot H_2O$. The reaction proceeded at 120 °C for 45 minutes under N_2 protection.[130] The PVP/TeNWs were the purified using the same procedure as for the CTAB/TeNWs.

Tellurium thin films

150 nm of tellurium was thermally evaporated onto indium tin oxide coated glass, removed inside a glovebox under N_2 protection (O_2 <0.1ppm, H_2O =0 ppm) and mounted on a sample holder, then directly transported through a thermal evaporator to an ultrahigh vacuum system.

P3HT, TeNW, and P3HT-TeNW film preparation

Pure P3HT was dissolved in chloroform (10 mg/ml) and the desired amount of a $FeCl_3$ chloroform solution (10 mg/ml) was added to the P3HT solution. The solution was stirred at 40 °C on a hotplate for *ca.* 15 hours in a nitrogen-filled glovebox. For the composites, the appropriate mass of TeNWs was weighed and separately added to either a 5 or 30% $FeCl_3$ doped P3HT solution and stirred. The solutions were drop-cast onto 2×2 cm clean glass slides, which were patterned using Kapton tape to define the region where the sample was deposited. For UPS measurements, the films were deposited onto indium tin oxide coated glass slides to prevent sample charging during measurement. The glass slides were cleaned through sequential sonication in a sodium dodecyl sulfate solution, deionized water, acetone, and ethanol followed by 10 minutes of UV-ozone exposure. The drop-cast films naturally dried and the dried films were annealed at 70 °C on a hotplate for 15 minutes inside of the glovebox. These films were then transferred to the thermal evaporator for electrode deposition and deposition of the bismuth thermometer. At no point were the films exposed to air.

Characterization

UV-Vis absorbance spectra were measured with an Ocean Optics QE Pro high performance spectrometer; SEM images were measured by a Hitachi S-4300 with an accelerating voltage of 10 kV; TEM images were taken with a JEOL 2010F at 200 kV; sheet resistance was measured with a four-point probe setup (Signatone S302-4, Keithley 2450 source meter); film thicknesses were measured with a Dektak D6M/32 profilometer; and XPS spectra were collected using X-rays generated by a Mg K-α source (1253.6 eV, PHI 04-548 Dual Anode X-ray source), an 11 inch diameter hemispherical electron energy analyzer with multichannel detector, with pass energies of 23.5 eV and 0.025 eV step sizes (PHI 5600). UPS measurements were performed using the Excitech H Lyman-α photon source (E-LUX^{TM}121) coupled with a 90^{o} ellipsoidal mirror (E-LUX^{TM} EEM Optical Module), as detailed in a previous publication.[131] Samples were negatively biased (-5 V) during UPS measurements and the pass energy was 5 eV. All UPS measurements were checked under a dry nitrogen purge of the beam path at 7.5 to8.5 Torr. The SECO of the samples was determined by the intersection of the background and a linear fit to the lower 50% of the SECO. The ionization energies were determined by the intersection of a linear fit to the lower 50% of the valence band or HOMO onset with the background.

Four probe Van der Pauw resistivity measurements were performed under vacuum using a Lakeshore CRX-VF probe station. Transport was measured using a Keithley 6517A and a Keithley 2182A. Silver paste is applied. All samples were cooled to 77K. A repeated temperature dependent resistivity measurement was checked in nitrogen filled glovebox with a linear four-point probe and a thermoelectric module used for temperature control. Temperature ranged from 300K to 265K.

Seebeck coefficients were measured with a custom-built setup. The P3HT:TeNW films were patterned according to geometries recommended to reduce any geometric contact errors below 8%.[115] A detailed drawing of our setup is provided in Figure 3.2. The P3HT:TeNW films were prepared by drop casting on a substrate that was masked with Kapton tape. Following film deposition, the tape was removed and 100 nm bismuth (α = -64.4 μV/K) was deposited alongside the P3HT:TeNW film through thermal evaporation to serve as a thermometer. The Seebeck coefficient of the 100 nm thick bismuth film was determined through placing type T thermocouples even with each gold contact to the bismuth film to determine the temperature differential across the bismuth film while measuring the thermovoltage. It is known that the Seebeck coefficient of bismuth will vary with thickness, and our determined value is 7% greater than that reported for a 123 nm thick film at 300 K.[132,133] Following bismuth deposition, 50 nm of gold was thermally evaporated for the electrodes and electrical contact pads. During Seebeck coefficient measurements the temperature of the hot block (Figure 3.15) was resistively heated and controlled by a temperature controller (TC200 Thorlabs) to vary the temperature difference across the sample by up to 8 K, while the voltage was measured across both the P3HT:TeNW film and bismuth thermometer using two Keithley 2100 6½ digit multimeters. A custom LabVIEW program was utilized to control the instruments and record the data. Each reported Seebeck value is the average of at least 4 different samples, with included error bars representing ± 1 standard deviation. Representative temperature vs. voltage plots are given in Figure 3.16.

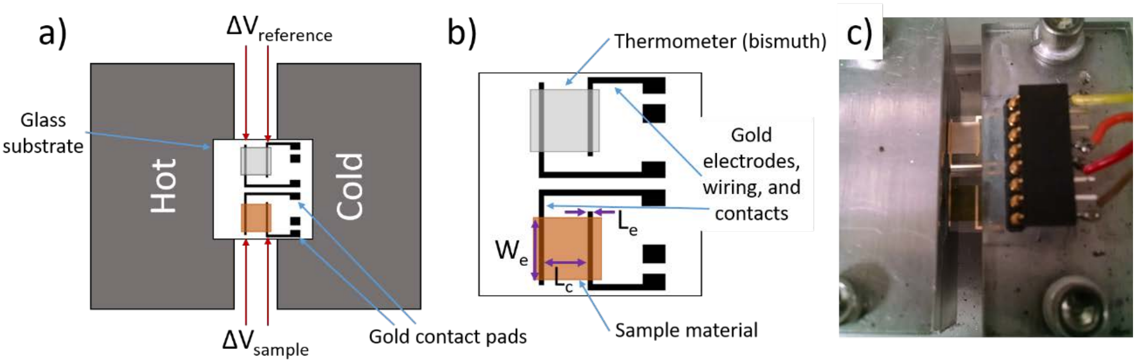

Figure 3.15 a) Overview schematic of our Seebeck measurement setup showing the substrate suspended between the hot and cold block, b) patterns of the sample, thermometer, and gold electrodes, and c) a photograph of the setup. In b) the critical dimensions are $L_c = 4.0$ mm, $L_e = 0.4$ mm, and $W_e = 5.5$ mm, which will result in an error of less than 8%.[115]

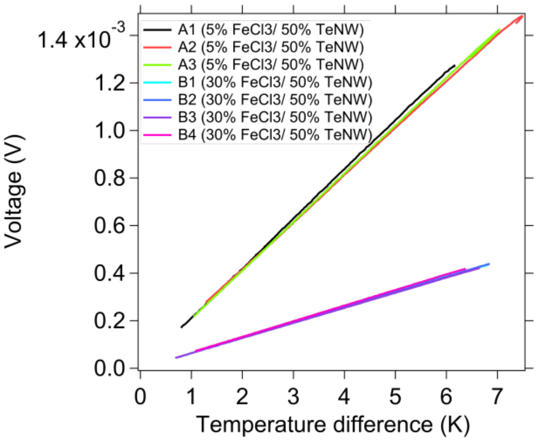

Figure 3.16 Sample voltage vs. temperature for 5 and 30% $FeCl_3$ doped samples with 50% TeNW concentration by weight. Each line corresponds with a separate film and is composed of approximately 200 individual data points. The temperature difference is calculated based on the bismuth film having a Seebeck coefficient of -64.4 μV/K.

Chapter 4: Influence of Dopant Size and Electron Affinity on the Electrical Conductivity and Thermoelectric Properties of Conjugated Polymers

This chapter is based on the paper: Zhiming Liang, Yadong Zhang, Maryam Souri, Xuyi Luo, Alex M. Boehm, Ruipeng Li, Yan Zhang, Tairan Wang, Doo-Young Kim, Jianguo Mei, Seth R. Marder, Kenneth R. Graham*, 2018, Submitted.

4.1 Introduction

Organic semiconductors are appealing for use in light-emitting diodes (OLEDs),[19,20] transistors,[21,22,134] photovoltaics,[135,136] and thermoelectrics (TEs)[23,24] due to their readily modified electrical and optical properties,[25] mechanical flexibility,[26] and solution processability.[27] Chemical doping (i.e., introducing free charge-carriers through the addition of a molecule that oxidizes or reduces the organic semiconductor) is particularly important in OLEDs, where doped transport layers are used in to improve charge injection,[137,138] and in TEs, where dopants are used to manipulate both the electrical conductivity (σ) and Seebeck coefficient (α) in TEs.[139,140] Controllably altering the electrical properties in chemically doped organic semiconductors is a major challenge. As opposed to doping in inorganic semiconductors, where the crystalline structure is largely unaffected by the incorporation of dopant atoms and the high dielectric constants and electronic band structures lead to highly delocalized charges, dopant incorporation into organic semiconductors significantly disrupts the morphology, alters the microstructure, and leads to charge-carriers with varying degrees of delocalization.[29,141,142,143] Furthermore, the doping efficiency (i.e., the fraction of dopants that lead to mobile charges) in organic semiconductors can be significantly less than unity and is hard to quantify. Selecting and designing dopants to achieve specific properties in films of organic semiconductors thus demands a better understanding of how dopants impact these parameters.

Since the field of π-conjugated polymers (πCPs) began with the discovery that πCPs could be made to have high electrical conductivities through chemical or electrochemical doping,[144,145] a consistent search for high performing dopants and polymers has continued. A number of different p-type dopants have received widespread attention due to their ability to effectively dope solution processed π-conjugated polymers and lead to high electrical conductivities, including $FeCl_3$,[40,80] I_2,[41,146] $Mo(tfd)_3$,[147] and F4TCNQ[29,142,148,149,150] and its derivatives.[151,152] Many factors that influence the electrical properties of doped πCPs are roughly understood, for example, the electrical properties are highly dependent on the doping efficiency, film morphology, doping mechanism (ground state charge-transfer complex vs. integer charge transfer[151,152]), and the polaron-anion coulombic attraction; however, the details and interrelationships between these parameters must be further understood to help guide the development of higher performing materials.

The doping efficiency of a given polymer-dopant system will be determined by two primary variables. The first variable expected to influence the doping efficiency is the difference between the polymer ionization energy (IE) and dopant electron affinity (EA) for p-doped polymers, or the polymer EA and dopant IE for n-doped polymers.[153] For p-doped polymers, the doping efficiency should generally increase as the $IE_{polymer}$ - EA_{dopant} difference increases and results in a larger thermodynamic driving force for polymer oxidation.[154,155] For example, Karpov *et al.* showed that when a high IE polymer (IE = 5.49 eV) is doped with a high EA dopant, hexacyno-trimethylene-cyclopropane (EA = 5.9eV), the electrical conductivity is more than two orders of magnitude higher than when a lower EA dopant is used, F4TCNQ (EA = 5.24eV).[151,153] Another factor determining the doping efficiency is the dopant miscibility with the polymer.[141,156,157,158,159] As the dopant molecules aggregate and phase separate from the polymer, they no longer efficiently dope the polymer. As a prime example, Schlitz *et al.* showed that σ for an n-doped polymer, poly{N,N'-bis(2octyl-dodecyl)-1,4,5,8-napthalenedicarboximide-2,6-diyl]-alt-5,5'-(2,2'-bithiophene), is limited by the miscibility of the n-type dopants, dihydro-1H-benzoimidazol-2-yl derivatives, with the polymer.[157]

Influential aspects of the morphology on the electrical conductivity include the degree of polymer crystallinity,[29] the size of the crystalline domains,[141,160] the effect of the dopant on the crystalline packing,[149,151] and the dopant distribution within the film (e.g., whether the dopant is primarily in the crystalline or amorphous regions).[29,141,160] The morphology of the doped film will depend largely on the processing conditions, the ability of the polymer to crystallize, and the interactions between the polymer and dopant. In doped regioregular poly(3-hexylthiophene)(RR-P3HT), the electrical conductivity can vary by *ca.* an order of magnitude a factor of five depending on the degree of crystallinity.[29,161] Typically, single-solution doping, whereby the polymer and dopant are both mixed together in solution, can lead to more disconnected crystallites compared with films of the pure polymer.[141] A sequential processing strategy has recently been explored to maintain highly connected polymer crystallites upon dopant addition.[29,141,155] Here, the polymer film is first cast from solution and then the pure polymer film is exposed to a solution containing the dopant. The dopant solution should be a poor solvent for the polymer and primarily cause the amorphous regions to swell and uptake dopant molecules while leaving the crystalline regions largely unaffected.[29,141] F4TCNQ doped RR-P3HT films prepared through sequential doping show electrical conductivities that are approximately an order of magnitude higher than films prepared through a standard single-solution doping method at the same doping concentrations.[29,141,152]

The doping mechanism can also vary based on the organic semiconductor and dopant used.[151,154,162] Here, the doping mechanism refers primarily to whether a charge-transfer complex is formed or whether integer charge transfer occurs. A ground state charge-transfer complex is characterized by the formation of hybrid intermolecular orbitals formed between the dopant and organic semiconductor upon doping, thus resulting in only partial charge transfer.[154] By contrast, integer charge transfer refers to the transfer of a whole charge from the organic semiconductor to the dopant and does not involve the formation of hybrid intermolecular orbitals. In the case that integer charge transfer occurs, the polaron-anion binding energy will also influence the electrical conductivity, as smaller polaron-anion coulombic interaction energies will lead to more delocalized polarons and higher charge-carrier mobilities.[143,163,164] The extent of polaron delocalization will highly impact the electrical conductivity and will be determined by both the polymer conformation, e.g., the degree of crystallinity as highlighted in the previous paragraph, and also on the distance separating the center of charge on the polymer and dopant.[29,163,165] We expect that dopant size is one of the key variables that will influence the separation between the center of charge on the polymer and dopant, and thus the coulombic interaction energy. By comparing the spectra of delocalized polarons and the mobility of RRa-P3HT, RR-P3HT, methylated ladder-type poly(para-phenylene), poly(9,9-dioctyl)fluorine and poly(phenylene-vinylene), Wohlgenannt *et al.* conclude that more delocalized polarons result in higher charge-carrier mobility and higher electrical conductivity.[166]

The above discussion highlights some of the complexities of how dopants influence the electrical conductivity in conjugated polymers, but this is only a portion of the required knowledge needed to design more efficient thermoelectric polymer-dopant systems. In thermoelectrics the power factor will depend on the product of the electrical conductivity (σ) and the Seebeck coefficient squared (α^2). Thus, it must also be understood how the dopant influences the Seebeck coefficient. To create high-performing thermoelectrics the effects of doping on both the electrical conductivity and Seebeck coefficient must be balanced to create the highest power factor ($P=\sigma\alpha^2$). For example, through controlling the degree of oxidation in poly(3,4-ethylenedioxythiophene) with tosylate and tetrakis(dimethylamino)ethylene, Bubnova *et al.* were able to reach power factors of 320 $\mu W\, m^{-1}\, K^{-2}$ at intermediate values of both σ and α.[139]

In this work, we investigate the effects of dopant size and EA on the electrical conductivity and Seebeck coefficient of p-doped conjugated polymers with varying IEs. The dopants include Mo(tfd-CO_2Me)$_3$, Mo(tfd)$_3$, and $FeCl_3$. Mo(tfd-CO_2Me)$_3$ and Mo(tfd)$_3$ are both relatively large dopants in size (~11--14 Å diameters) with high EAs of 5.30 eV and 5.51 eV (as measured with IPES), while $FeCl_3$ is smaller in size (~3 Å diameter) and has a much lower EA of 4.65 eV (as determined electrochemically, Figure 4.1e). As the doping efficiency is expected to vary with the difference between the polymer IE and dopant EA, we investigate polymers with IEs spanning from 4.6 to 5.15 eV, including RR-P3HT, RRa-P3HT, PDPP-4T and PDPP-T-TT-T as shown in Figure 4.1. Furthermore, we apply UV-Vis-IR absorbance, Raman scattering, grazing incidence X-ray diffraction (GIXRD), and ultraviolet photoelectron spectroscopies in an effort to understand why the Mo complexes lead to significantly higher electrical conductivities and power factors at low doping concentrations.

4.2 Results and Discussion:

4.2.1 Dopants and Polymers Energetics

The dopants shown in Figure 4.1a are selected due to their varying sizes and EAs, while the polymers shown are selected for their varying IEs and morphologies (e.g. crystalline vs. amorphous). The similar structure and charge-carrier mobilities of the diketopyrrolopyrrole (DPP) containing polymers[167,168,169] further allows us to isolate the influence of the difference between the polymer IE and dopant EA on the thermoelectric properties. Polymer IEs were measured using low-energy (10.2 eV) ultraviolet photoelectron spectroscopy (UPS), while dopants EAs were measured using low-energy inverse photoelectron spectroscopy (IPES) and cyclic voltammetry (CV). The use of lower energies than commonly employed in laboratory-based photoelectron spectrometers allows us to minimize sample damage and more accurately probe the material energetics.[131,170] The IEs and EAs for the polymers and dopants are shown in Figure 4.1b, with the UPS (Figure 4.1c and d), IPES (Figure 4.1e), and CV (Figure 4.1f-h) data for the polymers and dopants.

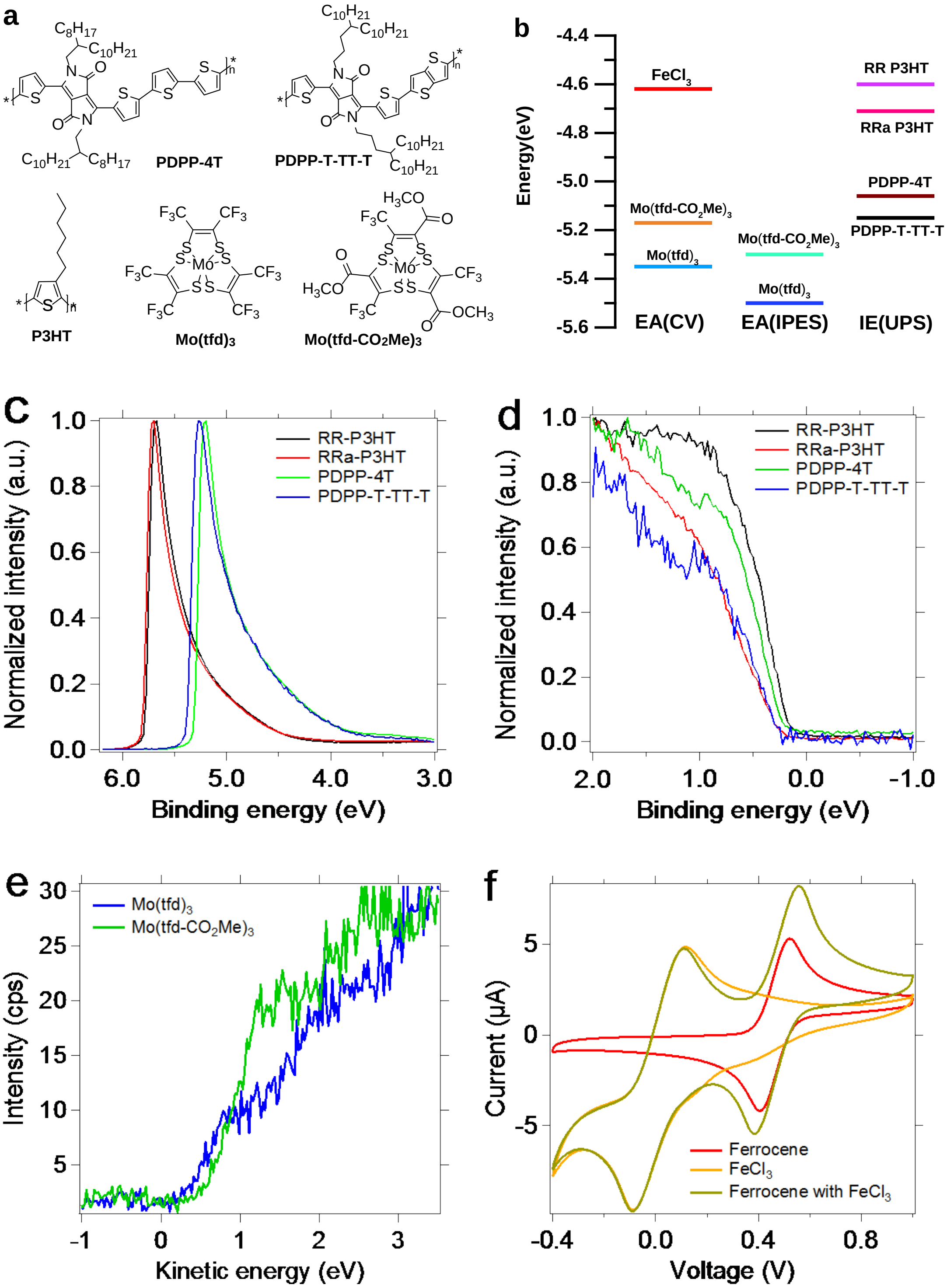
a
PDPP-4T
PDPP-T-TT-T
P3HT
Mo(tfd)3
Mo(tfd-CO2Me)3
b
Energy(eV)
-4.4
-4.6
-4.8
-5.0
-5.2
-5.4
-5.6
FeCl3
Mo(tfd-CO2Me)3
Mo(tfd)3
RR P3HT
RRa P3HT
PDPP-4T
PDPP-T-TT-T
EA(CV)
EA(IPES)
IE(UPS)
c
Normalized intensity (a.u.)
Binding energy (eV)
RR-P3HT
RRa-P3HT
PDPP-4T
PDPP-T-TT-T
d
Normalized intensity (a.u.)
Binding energy (eV)
RR-P3HT
RRa-P3HT
PDPP-4T
PDPP-T-TT-T
e
Intensity (cps)
Kinetic energy (eV)
Mo(tfd)3
Mo(tfd-CO2Me)3
f
Current (μA)
Voltage (V)
Ferrocene
FeCl3
Ferrocene with FeCl3

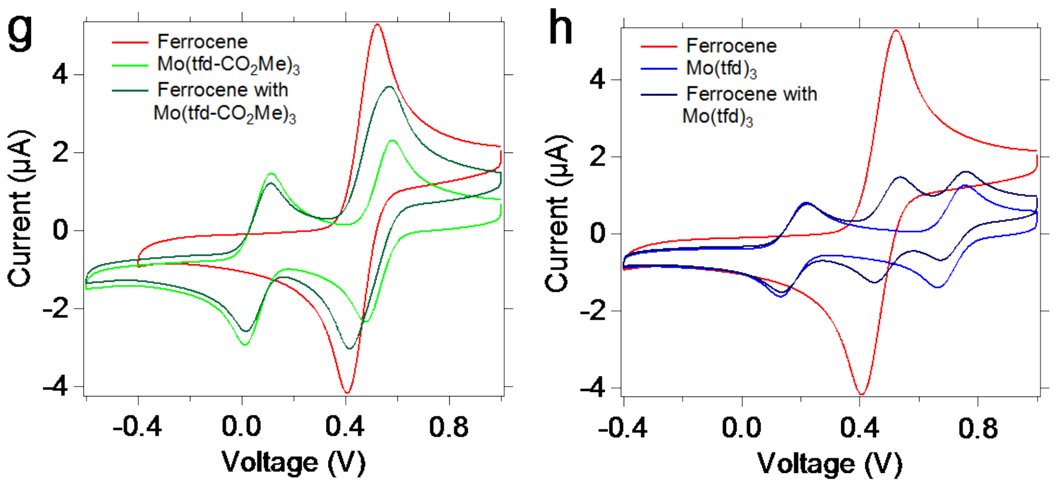

Figure 4.1 Molecular structures of P3HT, PDPP-4T, PDPP-T-TT-T, Mo(tfd)$_3$ and Mo(tfdCO$_2$Me)$_3$ (a), and polymer IEs as compared with dopant EAs (b), UPS Spectra of SECO regions (C), and HOMO onset(d), IPES spectra of LUMO onset(e), CV FeCl$_3$ and ferrocene (f), Mo(tfdCO$_2$Me)$_3$ and ferrocene (g), and Mo(tfd)$_3$ and ferrocene (h).

The UPS measured IEs correspond well with previously reported literature values.[80,171,172] However, the EAs of 5.51 and 5.30 we measured for Mo(tfd)$_3$ and Mo(tfd-CO$_2$Me)$_3$ differ slightly from the literature reported values of 5.6 and 5.0 eV.[173,174] We expect that the differences in our EA values compared to previous reports arise from the higher resolution (~0.3 eV compared to ~0.5 eV) and the reduced sample damage during measurement expected with our IPES system.[170] Uniform films of FeCl$_3$ for IPES measurements could not be prepared through solution processing and FeCl$_3$ appeared to decompose during thermal evaporation. This decomposition led to anonymously high EAs of 5.8 eV measured with IPES, and XPS measured stoichiometries that did not match the expected 1:3 composition of FeCl$_3$. The cyclic voltammetry measurements of FeCl$_3$ on the other hand showed that the reduction potential in chloroform was -0.48 V ($E_{1/2}$) vs. Fc/Fc$^+$, which can be converted to 4.62 eV vs. vacuum.[175] The $E_{1/2}$ values for Mo(tfd)$_3$ and Mo(tfd-CO$_2$Me)$_3$ vs. Fc/Fc$^+$ are 0.25 V and 0.07 V for the first reductions,[147,173,176] which yield values of 5.35 and 5.17 eV vs. vacuum. The reduction potentials from the CV measurements for Mo(tfd)$_3$ and Mo(tfd-CO$_2$Me)$_3$ are comparable to the IPES measured EA values, 5.51 and 5.30 eV, respectively.

4.2.2 Influence of Polymer IE - Dopant EA Difference on the Electrical Conductivity

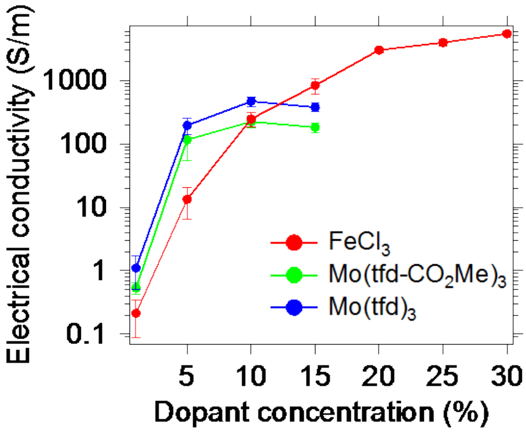

Figure 4.2 Electrical conductivities of $FeCl_3$, Mo(tfd-CO_2Me)$_3$, and Mo(tfd)$_3$ doped RR-P3HT as a function of the dopant concentration in mole percent relative to the polymer repeat unit. Each point is the average from 8 films produced from two fabrication runs and error bars are the standard deviation from all measurements over these 8 films.

The electrical conductivities of $FeCl_3$, Mo(tfd-CO_2Me)$_3$, and Mo(tfd)$_3$ doped RR-P3HT films are shown in Figure 4.2. One important trend is that at low doping concentrations sigma is up to 15 times higher for RR-P3HT doped with the Mo complexes than when doped with $FeCl_3$ at the same concentration. There are multiple factors that could potentially lead to the enhanced electrical conductivity observed for the Mo complexes as compared to $FeCl_3$ at low doping concentrations. These include differences in the doping efficiency, where we define the doping efficiency as the fraction of dopants that lead to a polaron on the polymer, or differences in the charge-carrier mobility.[177] The doping efficiency to a first approximation should be related to the difference in polymer IE and dopant EA, while the charge-carrier mobility will be primarily influenced by the film morphology and extent of polaron delocalization.[29,153,163] Another important trend evidenced in figure 4.2 is that sigma plateaus for RR-P3HT doped with the Mo complexes at between 5 and 10%, whereas sigma continues to increase for up to 30% doping with $FeCl_3$. The most likely explanation here, which will be further examined, is that the polaron concentration saturates at between 5 and 10% doping for RR-P3HT doped with the Mo complexes, while $FeCl_3$ continues to lead to mobile polarons at higher doping concentrations.

UV-Vis-near-IR optical absorbance measurements can be used as a probe of the polaron concentrations in the various doped films, as the ratio between the neutral state absorbance band at *ca.* 510 nm and the polaron band at *ca.* 790 nm will scale directly with the concentration of polarons.[40,80] Thus, we use these measurements as a semi-quantitative probe of doping efficiency. Figure 4.3a shows that the ratio between the polaron and neutral band continues to increase for $FeCl_3$ doped RR-P3HT up to 30% $FeCl_3$ concentration, whereas this ratio plateaus at 5 to 10% doping for the Mo complexes (Figure 4.3b-c). This data supports that for the Mo complexes the electrical conductivity at higher concentrations is limited by saturation in the number of polarons. We suspect that this difference in when the polaron band saturates is due to the more limited miscibility of the Mo complexes with P3HT.

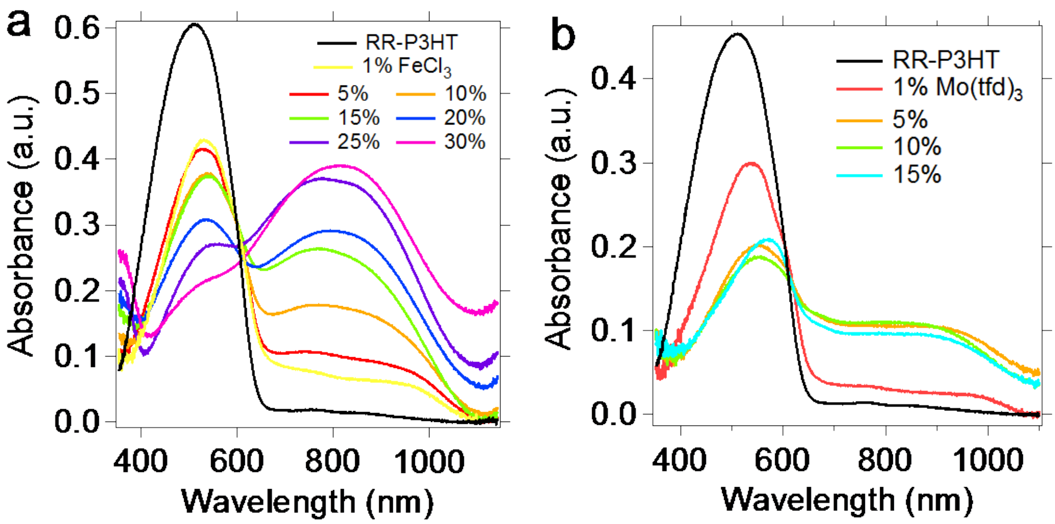

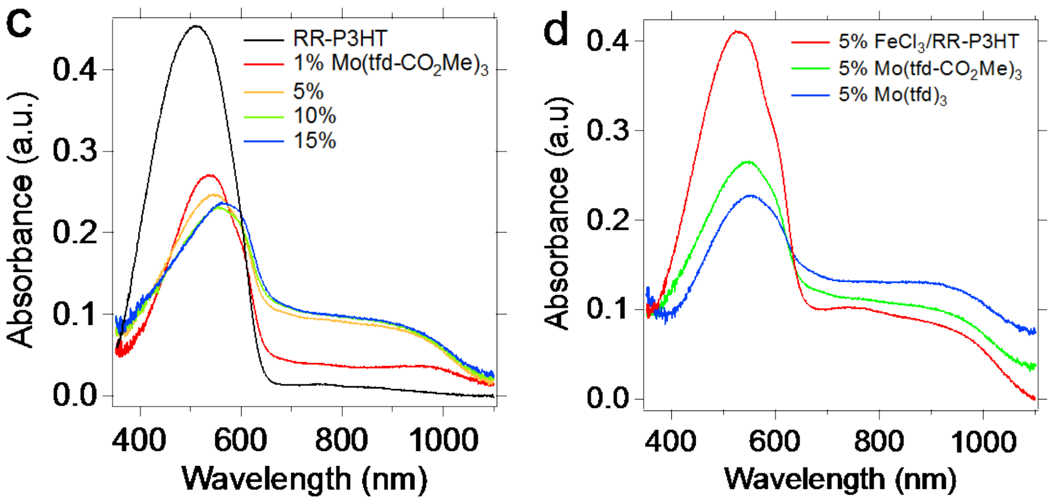

Figure 4.3 UV-Vis-near-IR absorbance spectra of RR-P3HT with a) $FeCl_3$, b) Mo(tfd)$_3$ and c)Mo(tfdCO$_2$Me)$_3$ at varying dopant concentrations (by mole). d) UV-Vis-near-IR absorbance spectra of RR-P3HT doped with 5% $FeCl_3$, Mo(tfdCO$_2$Me)$_3$, and Mo(tfd)$_3$.

Focusing on the 5% dopant concentration (Figure 4.3d), where the polaron concentration is not saturated for any of the dopants, it is evident that the polaron band to neutral band absorbance ratio is largest for the Mo(tfd)$_3$ sample, followed by the Mo(tfdCO$_2$Me)$_3$ sample, and lowest for the $FeCl_3$ sample. This trend in the polaron band to neutral band absorbance ratio is consistent with the trend in electrical conductivities, i.e., the electrical conductivity increases as the polaron band to neutral band absorbance ratio increases across the dopant series. The lower polaron band intensity for $FeCl_3$ is likely due to the lower EA of $FeCl_3$, which falls at nearly the same value as the IE of RR-P3HT, or potentially to the doping mechanism. The lower polaron band absorbance for Mo(tfd-CO$_2$Me)$_3$ relative to Mo(tfd)$_3$ may be due to the higher EA of Mo(tfd)$_3$ relative to Mo(tfd-CO$_2$Me)$_3$, although even in the case of Mo(tfd-CO$_2$Me)$_3$ a large IE-EA difference of 0.7 eV is expected to be sufficient for complete dopant ionization.[150,153,154]

Based on the absorbance spectra there are ca. 50% more polarons in RR-P3HT doped with Mo(tfd)$_3$ as there are in RR-P3HT doped with $FeCl_3$ at 5% doping; however, the σ of Mo(tfd)$_3$ doped RR-P3HT is 15 times greater than that of $FeCl_3$ at this same doping concentration. The electrical conductivity is proportional to the product of the charge-carrier mobility and the concentration of mobile charge carriers. Considering this relationship, the absorbance ratios, and the measured electrical conductivities, it appears that at low doping concentrations the charge-carrier mobility for Mo(tfd)$_3$ doped RR-P3HT is greater than for FeCl$_3$ doped RR-P3HT. The higher mobility of Mo(tfd)$_3$ doped RR-P3HT is further supported by the observation that the 5% doped Mo(tfd)$_3$ sample has a similar electrical conductivity to that of 10% doped FeCl$_3$, even though the 10% doped FeCl$_3$ has higher polaron absorbance as shown in Figure 4.3d. These differences in apparent charge-carrier mobilities are attributed partly to increased polaron delocalization for Mo(tfd)$_3$ doped RR-P3HT relative to FeCl$_3$ doped RR-P3HT, as will be discussed further in the proceeding section.

The doping efficiencies as probed through absorbance measurements agree with expectations based purely on the difference between the polymer IE and dopant EA. That is, dopants with higher EAs result in higher doping efficiencies for the same polymer. To further investigate the influence of the polymer IE-dopant EA difference on the electrical conductivity, Figure 4a shows the electrical conductivity for all polymers investigated as a function of the dopant concentration. Given that PDPP-4T and PDPP-T-TT-T have more aromatic rings in their repeat units as compared to P3HT (6 rings vs. 1 ring), we present the dopant concentration as relative to the number of aromatic rings in the polymer backbone to allow for more direct comparisons between the polymers. Figure 4.3a shows that at low doping concentrations of 1-5%, Mo(tfd)$_3$ doping leads to electrical conductivities that are 15 to 800 times higher than for FeCl$_3$ doping with the same polymer. Furthermore, the difference between the electrical conductivity with Mo(tfd)$_3$ doping and FeCl$_3$ doping increases as the polymer IE increases. Figure 4.3b compares the ratio of σ with Mo(tfd)$_3$ doping at 1-5% to σ with FeCl$_3$ at 1-5% for the polymers as a function of polymer IE. The increasing σ ratio with polymer IE shows that the doping efficiency difference between Mo(tfd)$_3$ and FeCl$_3$ increases with IE, as expected based on simple energetic considerations.

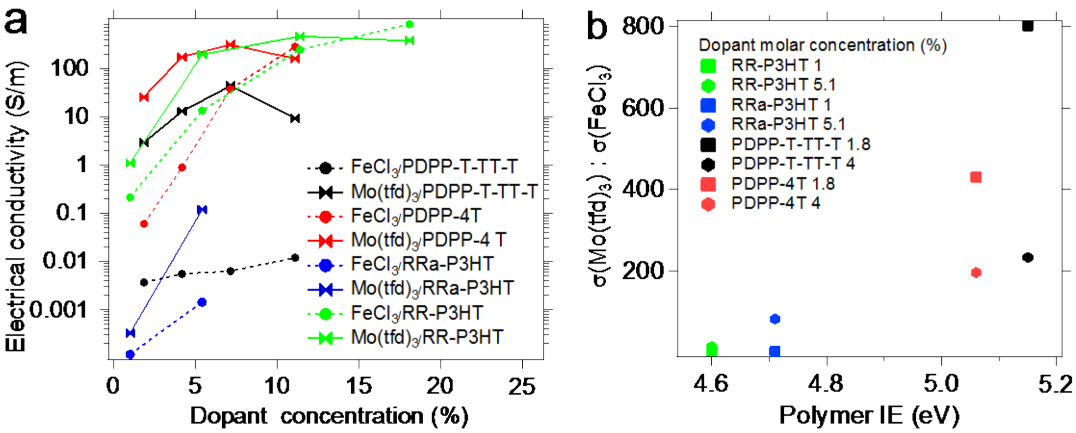

Figure 4.4 Electrical conductivity of $Mo(tfd)_3$ and $FeCl_3$ doped RR-P3HT, RRa-P3HT, PDPP-4T and PDPP-T-TT-T as a function of the dopant concentration (a) and the ratio of sigma for $Mo(tfd)_3$ and $FeCl_3$ doped polymers at 1-6% doping as a function of the polymer IE (b).

4.2.3 Influence of the Film Morphology on the Electrical Conductivity

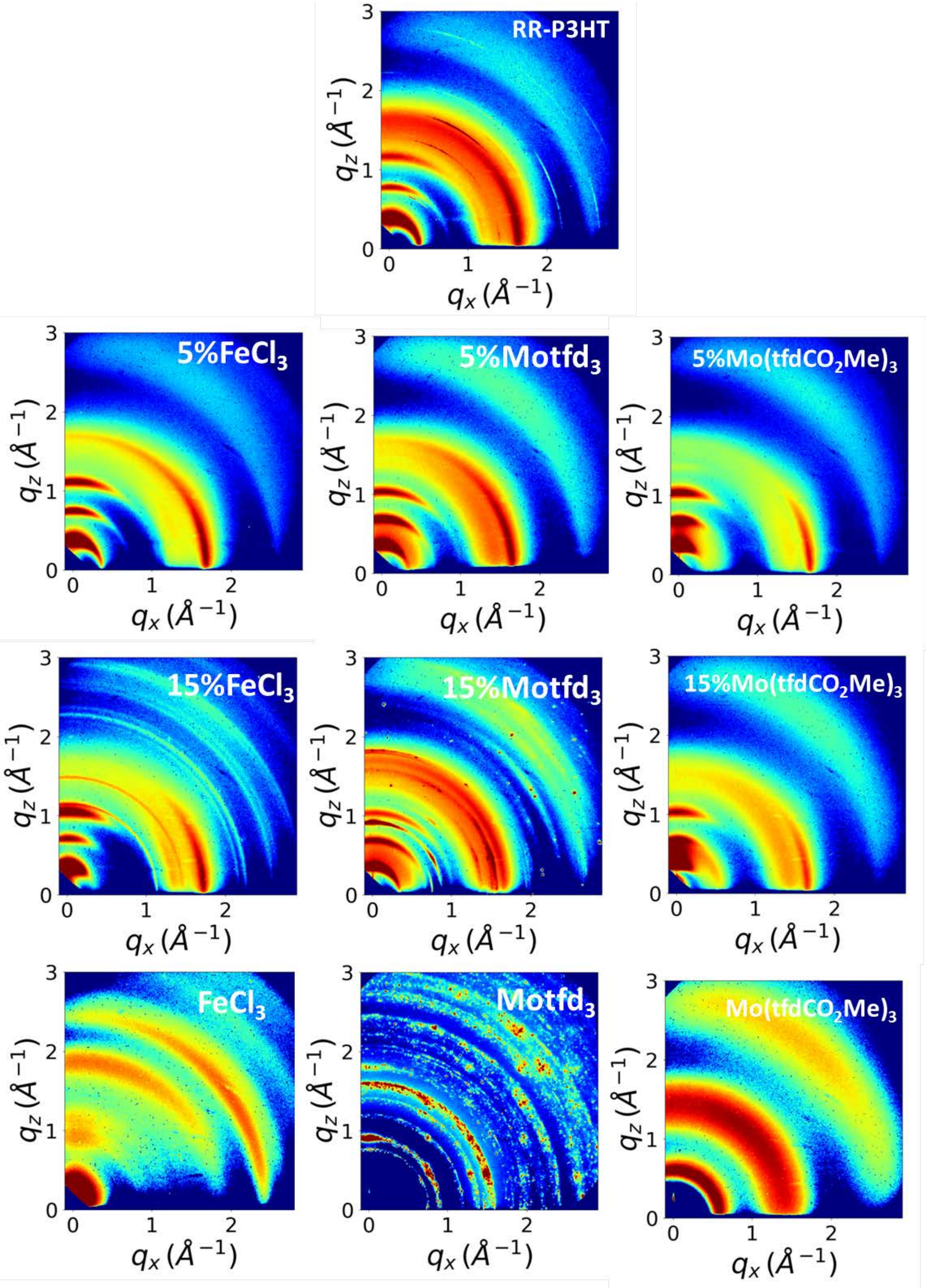

Figure 4.5 GIXRD of dopants, RR P3HT and single-solution doped RR P3HT.

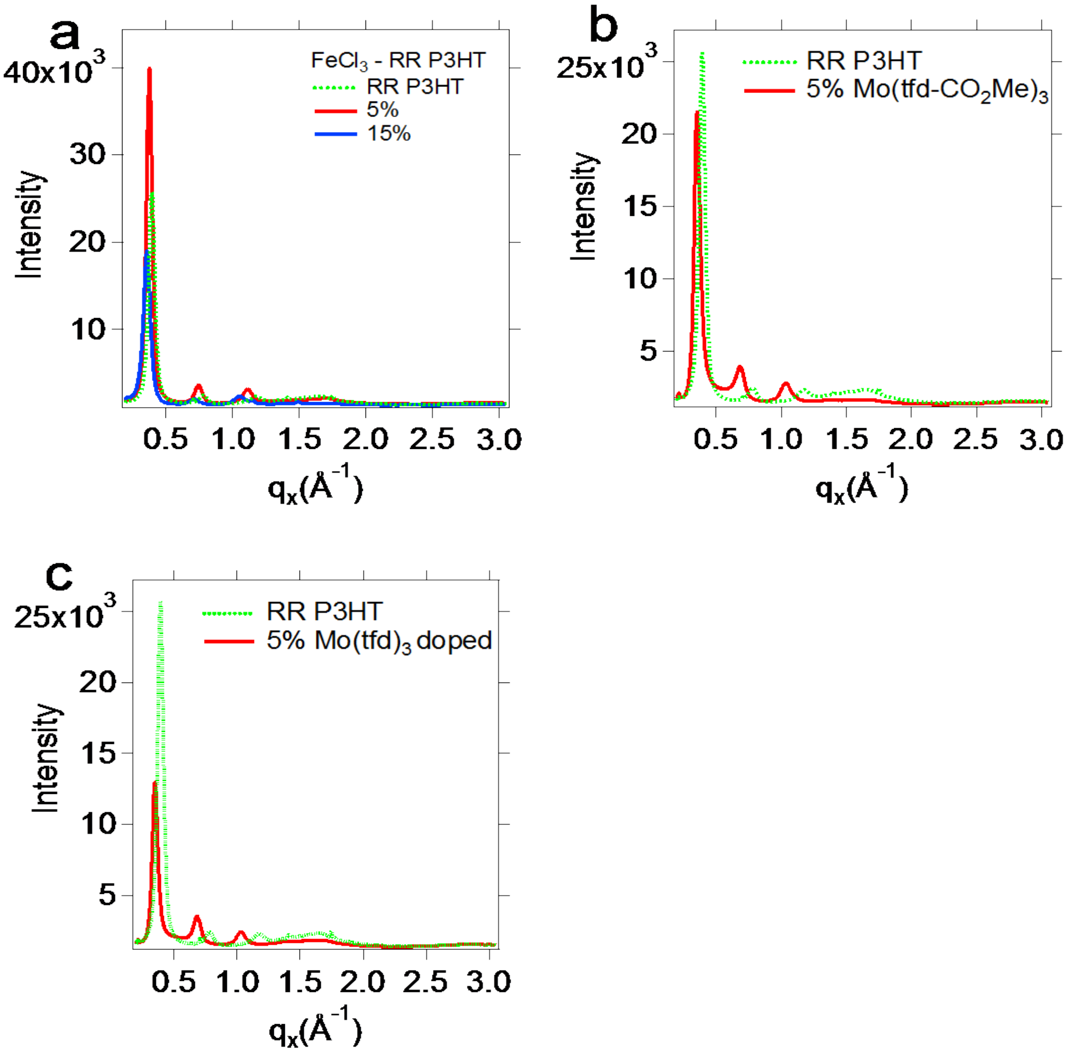

Figure 4.6 GIXRD of doped RR-P3HT. (Out of plane integrated intensity over 60 – 90 degree cake slice)

Table 4.1 In and out-plane X-ray Scattering peaks of doped RR P3HT from GIXRD

Doped RR P3HT Molar fraction	**d-spacing (Å) (010)**	**d-spacing (Å) (100)**	**d-spacing (Å) (200)**	**d-spacing (Å) (300)**
RR-P3HT	3.81	16.01	8.02	5.36
FeCl$_3$ 5%	3.72	16.75	8.48	5.65
FeCl$_3$ 15%	3.62	17.69	8.86	5.97
Mo(tfdCO$_2$Me)$_3$ 5%	3.73	18.13	9.19	6.11
Mo(tfdCO$_2$Me)$_3$ 15%	3.75	17.69	9.35	6.12
Mo(tfd)$_3$ 5%	3.75	17.83	9.19	6.07
Mo(tfd)$_3$ 15%	3.75	17.69	9.35	6.12

To a first order approximation the electrical conductivity corresponds with the number of polarons present. However, as discussed in section 4.2.2, it appears that the charge-carrier mobility also varies as a function of dopant. Part of the differences in charge-carrier mobilities may be from where the dopants are located and how the different dopants influence film crystallinity. To investigate the morphology differences between the solution doped films with varying dopants, grazing-incidence X-ray diffraction (GIXRD) was used to probe the crystalline order of the doped RR-P3HT films (Figure 4.5, 4.6 and table 4.1). The π-π stacking distance (010) contracts upon dopant addition for all three dopants. At 5% this contraction varies from 0.06 to 0.09 Å for the three doped samples as compared to undoped RR-P3HT. As the dopant concentration increases further to 15%, the π-π stacking distances are largely unchanged from the 5% doped samples for the Mo complex dopants. By contrast, the 15% $FeCl_3$ doped RR-P3HT showed an additional 0.09 Å contraction in the π-π stacking distance from the 5% $FeCl_3$ doped film. This comparison between the 5% and 15% doped samples agrees with the UV-Vis and electrical conductivity data to further support that $FeCl_3$ can continue to dope RR-P3HT at concentrations above 10%, whereas the ability of the Mo complexes to dope RR-P3HT saturates at between 5 and 10%. The origin of this decrease in the π-π stacking distance is polaron stabilization, as discussed by Scholes *et al.*[29] Essentially, the RR-P3HT backbones are pulled closer together to stabilize the positively charged polarons.

The lamellar stacking distances (100) increase from 16.01 to between 16.75 and 18.13 Å as RR-P3HT is doped at 5%. The lamellar stacking distance continues to increase for $FeCl_3$ doping as the dopant concentration is further increased from 5 and 15%, but slightly decreases as the Mo dopants are increased from 5 and 15%. The increase in lamellar spacing is only on the order of 1.6 to 2.1 Å in all Mo complex doped RR-P3HT samples, which should not be large enough to accommodate the Mo complexes (~11-14 Å diameters) (Figure 4.7). The inability of the Mo complexes to intercalate between the P3HT crystalline sidechains is supported by previous work investigating fullerene intercalation, where the similarly large size of C_{60} prevented intercalation.[178] Here, we propose that the Mo complexes are located at the edges of the crystalline regions or in the amorphous regions, which was the position recently argued by Scholes, et al. for F4TCNQ doping of RR-P3HT.[29] If this is indeed the case, then the increased lamellar stacking distance may originate partly from repulsive coulombic interactions between the polarons in the crystalline regions. It is more difficult to hypothesize where the $FeCl_3^-$ anions, or potentially $Fe_2Cl_6^-$ or $FeCl_4^-$ anions,[179,180] are located, as these are smaller (~3-6 Å diameters shown in Figure 4.6) and may be able to intercalate between the P3HT sidechains within the crystalline regions.

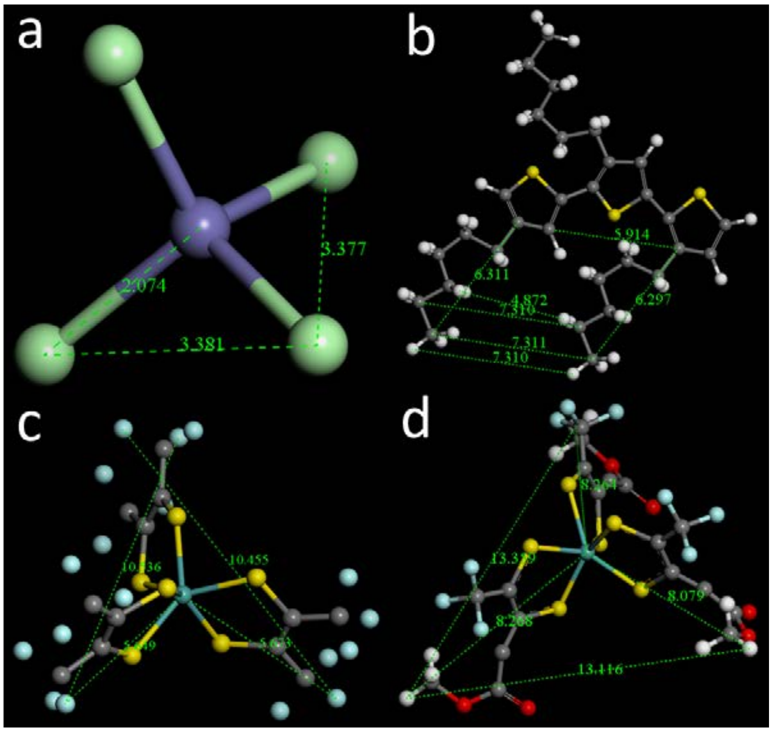

Figure 4.7 Chemical structure of dopants. a) $FeCl_4^-$, b) three repeating units of P3HT, c) $Mo(tfd)_3$,and d) $Mo(tfd\text{-}CO_2Me)_3$. These structures are geometry optimized by *ab initio* code Dmol3 in Materials studio. LDA (local density approximation) is chosen as the approximation to the exchange and correlation energy functional. SCF (Self-consistent field) tolerance is $1.0*10^{-6}$ Ha. These optimized values are comparable to some similar X-ray structure in the references)[181,182]

In solution doped RR-P3HT, the doped polymers may aggregate with the anionic dopants,[141] with different dopants leading to different extents of solution aggregation and film morphologies. As shown in Figure 4.8, for the solution doped

RR-P3HT samples with 5% of the dopants, the root mean squared (RMS) is nearly twice as high with $FeCl_3$ (10.4 nm) as with $Mo(tfd)_3$ (4.6 nm) and Mo(tfd-CO_2Me) (6.3 nm). One means of minimizing the morphological differences between the films with the varying dopants is to use sequential doping. In this method, RR-P3HT films are first Spin-cast from chlorobenzene and the film is then doped by spin coating a solution of $FeCl_3$ or $Mo(tfdCO_2Me)_3$ in acetonitrile on top of the film ($Mo(tfd)_3$ does not dissolve in acetonitrile). Acetonitrile is a poor solvent and causes the amorphous regions to swell and uptake the dopant molecules, whereas the crystalline regions stay largely intact.[29,141,163] For these sequentially doped films the $Mo(tfdCO_2Me)_3$ (σ=56.2±1.1 S/m) doped RR-P3HT sample has a doping ratio between the $FeCl_3$ doped RR-P3HT samples that were prepared with 0.03 (σ=8.1±1.2 S/m) and 0.05 (σ=34.4±1.4 S/m) $FeCl_3$ concentrations. This data is in agreement with the single-solution doped films where the Mo complexes both exhibited higher conductivity than $FeCl_3$ doped samples at similar polaron concentrations. The agreement in trends between sequentially doped and single-solution doped films suggests that the observed differences in electrical conductivity between $FeCl_3$ and Mo complex doped films are not due to the degree of crystallinity or the connectedness of the crystalline regions.

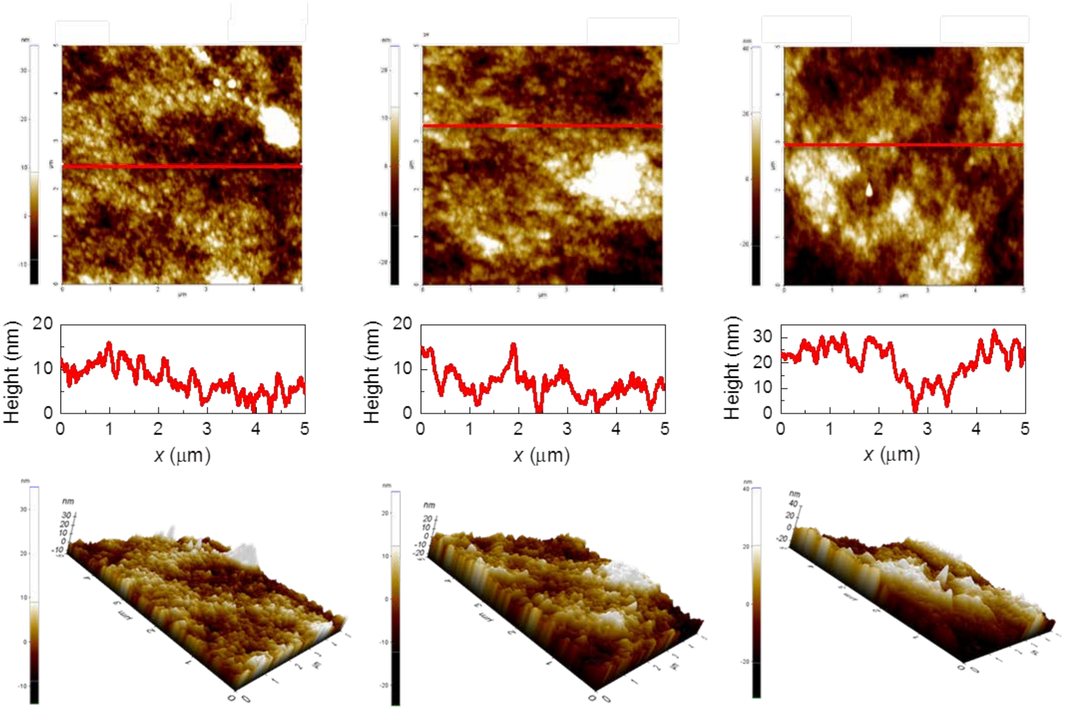

Mo(tfd)$_3$ Rq(nm) = 4.586 Mo(tfdCO$_2$Me)$_3$ Rq(nm) = 6.285 FeCl$_3$ Rq(nm) = 10.418

Figure 4.8 AFM images of 5.1% molar fraction FeCl$_3$, Mo(tfd)$_3$, and Mo(tfdCO$_2$Me)$_3$ doped RR P3HT.

Absorption measurements in the near-IR to mid-IR region can shed further light on understanding the transport properties of the doped films by probing the degree of polaron delocalization. Here, the Salleo and Schwartz groups have both shown that as the degree of polaron delocalization increases the polaron band in the mid-IR region (peak ~0.4 eV) will shift to lower energies.[29,163] For solution doped RR-P3HT at 5%, the Mo complexes dopants show similar P$_1$ bands with peaks at *ca* 0.29 eV, while with FeCl$_3$ this P$_1$ band is shifted to higher energies with a peak at 0.38 eV(Figure 4.9a). The lower energy P$_1$ bands for the Mo complexes indicate that polarons are more delocalized than with FeCl$_3$ as the dopant.[29,166] The same trend is evident with the sequentially doped samples, which suggests that the bathochromic shift of the low energy polaron peak is not due to gross changes in the degree of crystallinity. Thus, we attribute the bathochromic shift in the polaron peak to the presence of a more delocalized polaron as a result of decreased polaron-anion coulombic interactions. This decreased coulombic interaction is expected from the larger size of the Mo complexes relative to the $FeCl_3$ ions, which results in a greater average separation between the charge on the Mo anion and the P3HT polaron.

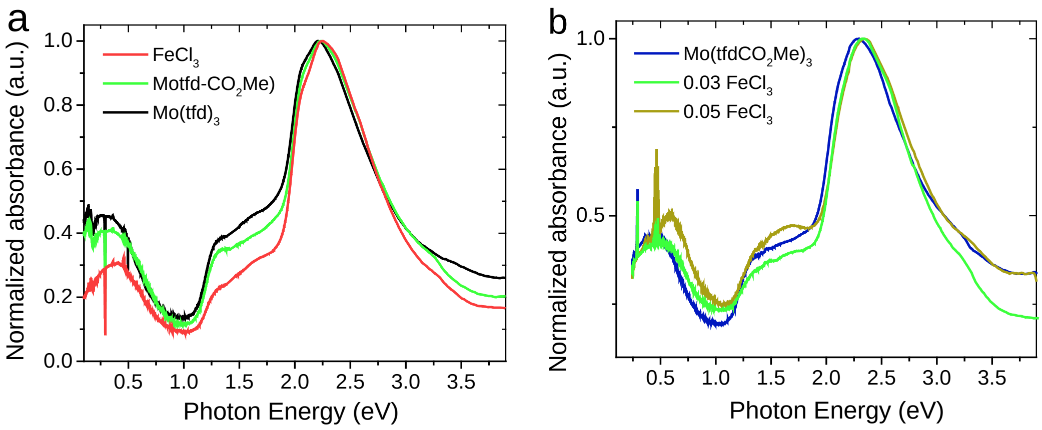

Figure 4.9 UV-Vis-IR absorbance spectra of solution doped RR-P3HT films (a) and sequential doped RR-P3HT (b).

An additional probe of polaron delocalization is the position of the Raman modes associated with the pi-conjugated polymer backbone. Previous work has shown that as the polaron becomes more delocalized it weakens the bond strengths and results in lower energy stretching modes.[40,183] The Raman spectra shown in Figure 4.10 display distinctly different changes based on the dopant. For Mo(tfd)$_3$ and Mo(tfd-CO_2Me) doped RR-P3HT the 1400-1500 cm^{-1} peak, which is attributed to C_α=C_β stretching vibrations, shifts from 1447 cm^{-1} in undoped RR-P3HT to 1425 and 1432 cm^{-1} for 10% doping with Mo(tfd)$_3$ and Mo(tfd-CO_2Me), respectively. By contrast, the RR-P3HT sample doped with 10% $FeCl_3$ displays a broadened Raman peak with a maximum that is shifted by only 1 cm^{-1} relative to undoped RR-P3HT. The significant broadening of the $FeCl_3$ doped RR-P3HT may indicate varying degrees of polaron delocalization and an overall increase in the disorder of the RR-P3HT film (Figure 4.10h). The relatively large bathochromic shift in the Mo complex doped RR-P3HT as compared to the minimal peak shift observed with $FeCl_3$ doping further supports that both Mo complexes lead to more delocalized polarons relative to $FeCl_3$.

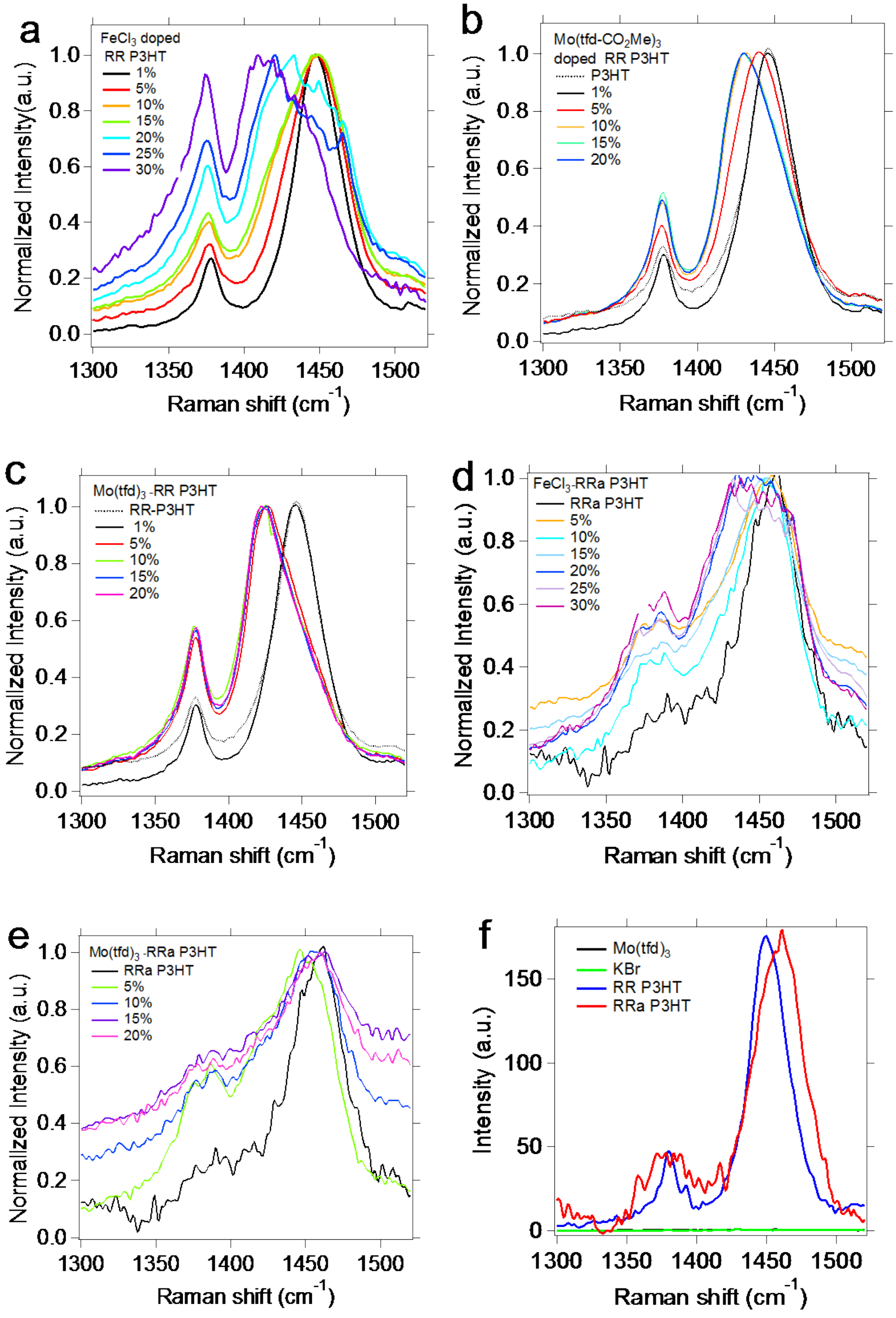
a
FeCl$_3$ doped
RR P3HT
1%
5%
10%
15%
20%
25%
30%
Normalized Intensity(a.u.)
Raman shift (cm^{-1})
b
Mo(tfd-CO$_2$Me)$_3$
doped RR P3HT
P3HT
1%
5%
10%
15%
20%
Normalized Intensity (a.u.)
Raman shift (cm^{-1})
c
Mo(tfd)$_3$ -RR P3HT
RR-P3HT
1%
5%
10%
15%
20%
Normalized Intensity (a.u.)
Raman shift (cm^{-1})
d
FeCl$_3$-RRa P3HT
RRa P3HT
5%
10%
15%
20%
25%
30%
Normalized Intensity (a.u.)
Raman shift (cm^{-1})
e
Mo(tfd)$_3$ -RRa P3HT
RRa P3HT
5%
10%
15%
20%
Normalized Intensity (a.u.)
Raman shift (cm^{-1})
f
Mo(tfd)$_3$
KBr
RR P3HT
RRa P3HT
Intensity (a.u.)
Raman shift (cm^{-1})
0.0
0.2
0.4
0.6
0.8
1.0
0
50
100
150
1300
1350
1400
1450
1500

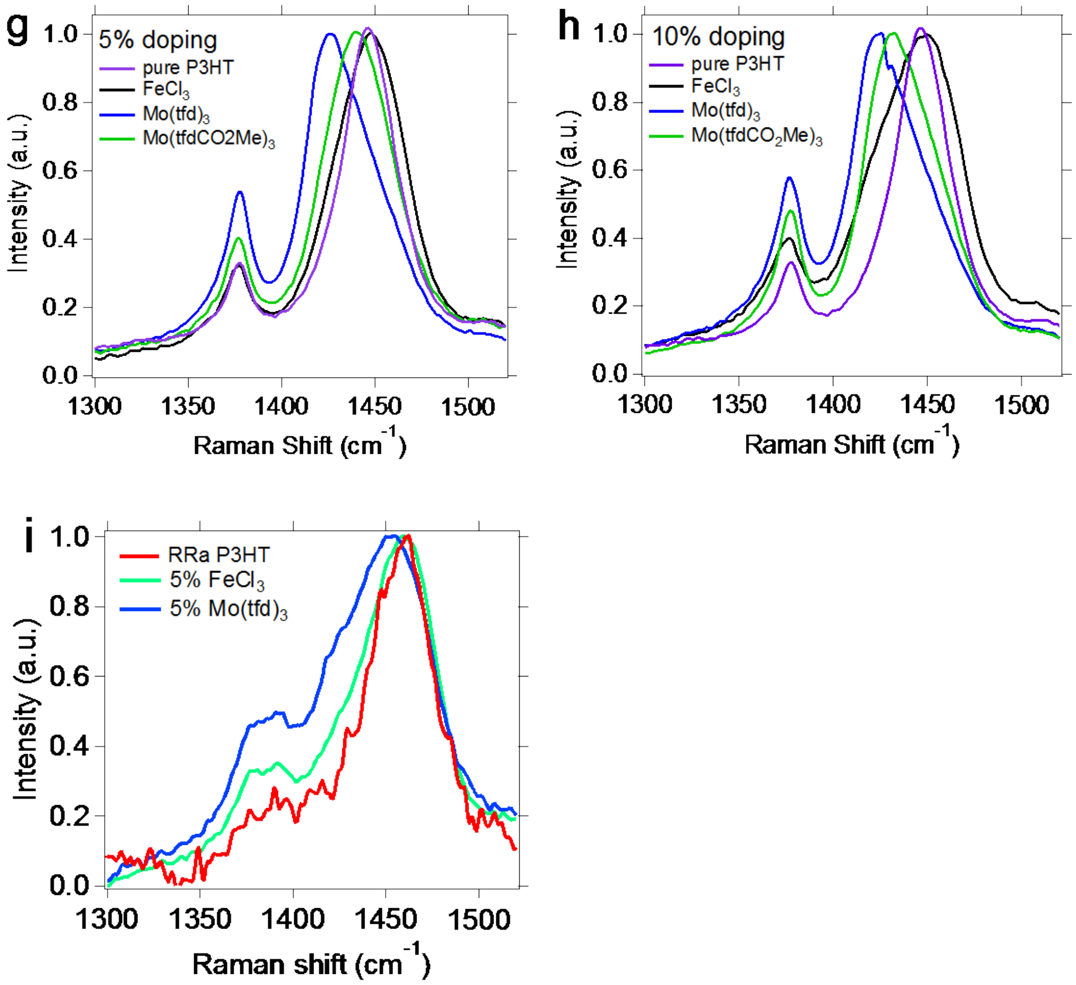

Figure 4.10 Raman spectra: a)$FeCl_3$-RR P3HT, b) $Mo(tfdCO_2Me)_3$-RR P3HT, c) $Mo(tfd)_3$-RR P3HT, d) $FeCl_3$-RRa P3HT, e) $Mo(tfd)_3$-RRa P3HT, f) RR, RRa P3HT, and $Mo(tfd)_3$, 5% (g) and 10% (h) $Motfd_3$, $Mo(tfdCO_2Me)_3$ and $FeCl_3$ doped RR-P3HT, 5% measured $Motfd_3$, and $FeCl_3$ doped RRa-P3HT (i) with 532 nm excitation.

As a final means of minimizing morphological differences, we compare RRa-P3HT with the varying dopants, as RRa-P3HT is completely amorphous and thereby not affected by varying degrees of crystallinity as RR-P3HT is. An additional verification that delocalization indeed leads to the observed bathochromic shifts in the Raman modes is obtained through an analysis of the Raman spectra of doped RRa-P3HT. Here, due to the lack of crystallinity and the increased torsion angles in the polymer backbone, the polaron should be more localized than in RR-P3HT. Comparing $Mo(tfd)_3$ doped RRa-P3HT and RR-P3HT, as shown in Figure 4.9i, we indeed see that the maximum bathochromic shift in $Mo(tfd)_3$ doped RRa-P3HT (*ca.* 14 cm^{-1}) is significantly less than in RR-P3HT (*ca.* 23 cm^{-1}).

4.2.4 Influence of the Dopant on the Seebeck Coefficient and Thermoelectric Performance

The thermoelectric performance parameters for RR-P3HT with the different dopants are displayed in Figure 4.11 as a function of dopant concentration. The Seebeck coefficient and electrical conductivity are inversely related, i.e., as the electrical conductivity increases the Seebeck coefficient decreases. This trend arises as the Seebeck coefficient is determined by the average entropy carried per charge carrier, and the entropy carried is dependent on the separation between the transport states and the Fermi energy.[184,185] In general as more charge carriers are introduced, the Fermi energy shifts closer towards the transport states (i.e., the HOMO edge in a p-type material) and therefore each charge-carrier transports less entropy. Figure 4.11a shows the Seebeck coefficient of all doped RR-P3HT films as a function of the doping concentration. With all dopants α decreases by *ca.* 60% as the dopant concentration increases from 1 to 5%. The Seebeck coefficients largely plateaus between 5 and 15% dopant for the Mo complexes, which is consistent with the saturation of the electrical conductivities. By contrast, with $FeCl_3$ doping the Seebeck coefficient continues to decrease as the dopant concentration increases.

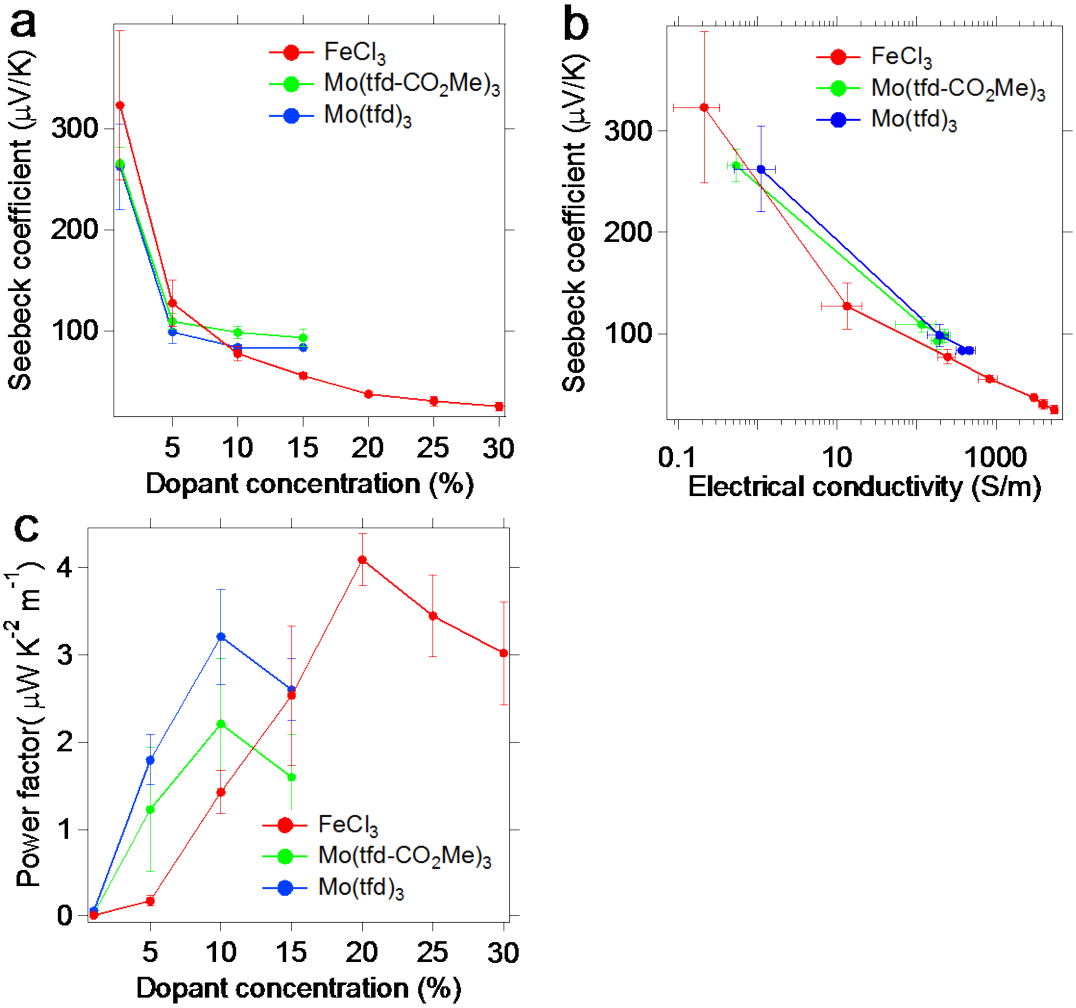

Figure 4.11 Seebeck coefficient vs. dopant concentration (a), Seebeck coefficient vs. electrical conductivity (b), and power factor vs. dopant concentration (c) for single-step solution doped RR-P3HT with $Mo(tfd)_3$, $Mo(tfdCO_2Me)_3$, and $FeCl_3$.

The most important difference in terms of thermoelectric performance is that at 5% doping the Seebeck coefficients for all dopants are similar (all fall within 20% of the mean), despite the electrical conductivities being over an order of magnitude higher for the Mo dopants. As shown in Figure 4.11b, for the 5-15% dopant concentrations the RR-P3HT films doped with the Mo complexes display higher Seebeck coefficients than RR-P3HT doped with $FeCl_3$ at a given electrical conductivity. As a result, $Mo(tfd)_3$ doping results in a power factor that is *ca.*10 times higher than with $FeCl_3$ doping at 5% and 2.3 times as high at 10% doping. The higher power factors at low doping concentrations for the Mo complexes relative to $FeCl_3$ is most likely attributed to higher mobility charge-carriers in the Mo doped samples. Our reasoning being that the position of the Fermi energy relative to the transport states will exert a large influence on the Seebeck coefficient. Neglecting changes to the density of states distributions imparted by the differing dopants, the position of the transport states relative to the Fermi energy will be determined by the number of charge-carriers present. If the charge-carrier mobilities differ by an order of magnitude upon doping with two different dopants, then with the same number of polarons and similar Seebeck coefficients the material with the higher charge-carrier mobility will have an order of magnitude higher electrical conductivity. To further investigate this explanation, we turn to UPS measurements.

Ultraviolet photoelectron spectra of RR-P3HT with the varying dopants were measured (Figure 4.12) to probe the position between the HOMO onset and the Fermi energy. At low concentrations, the work function (Figure 4.12i) and ionization energy (Figure 4.12j) of doped RR-P3HT increases as dopants concentrations increase. As the loadings of dopants is higher than 10%, WF and IE of Mo complexes doped RR P3HT is no obvious change while $FeCl_3$ doped films continue increasing even up to 30%. The trend of WF and IE is consistent with the change of doped films electrical conductivity which further supports the previous discussion of doping efficiency. At 5% doping concentration, Figure 8c and e show that the positions of the HOMO onsets relative to the Fermi energies are similar with all dopants. With the difference between the transport states and Fermi energy playing a major role in determining the Seebeck coefficient, this UPS data supports that the Seebeck coefficients should be similar at this 5% doping concentration. At higher doping concentrations the HOMO onset continues to approach the Fermi energy (Figure 4.12k), particularly for $FeCl_3$ doping. In general, the continuously decreasing difference between the HOMO onset and Fermi energy for $FeCl_3$ doping agrees with the steady drop in the Seebeck coefficient with increasing $FeCl_3$ doping.

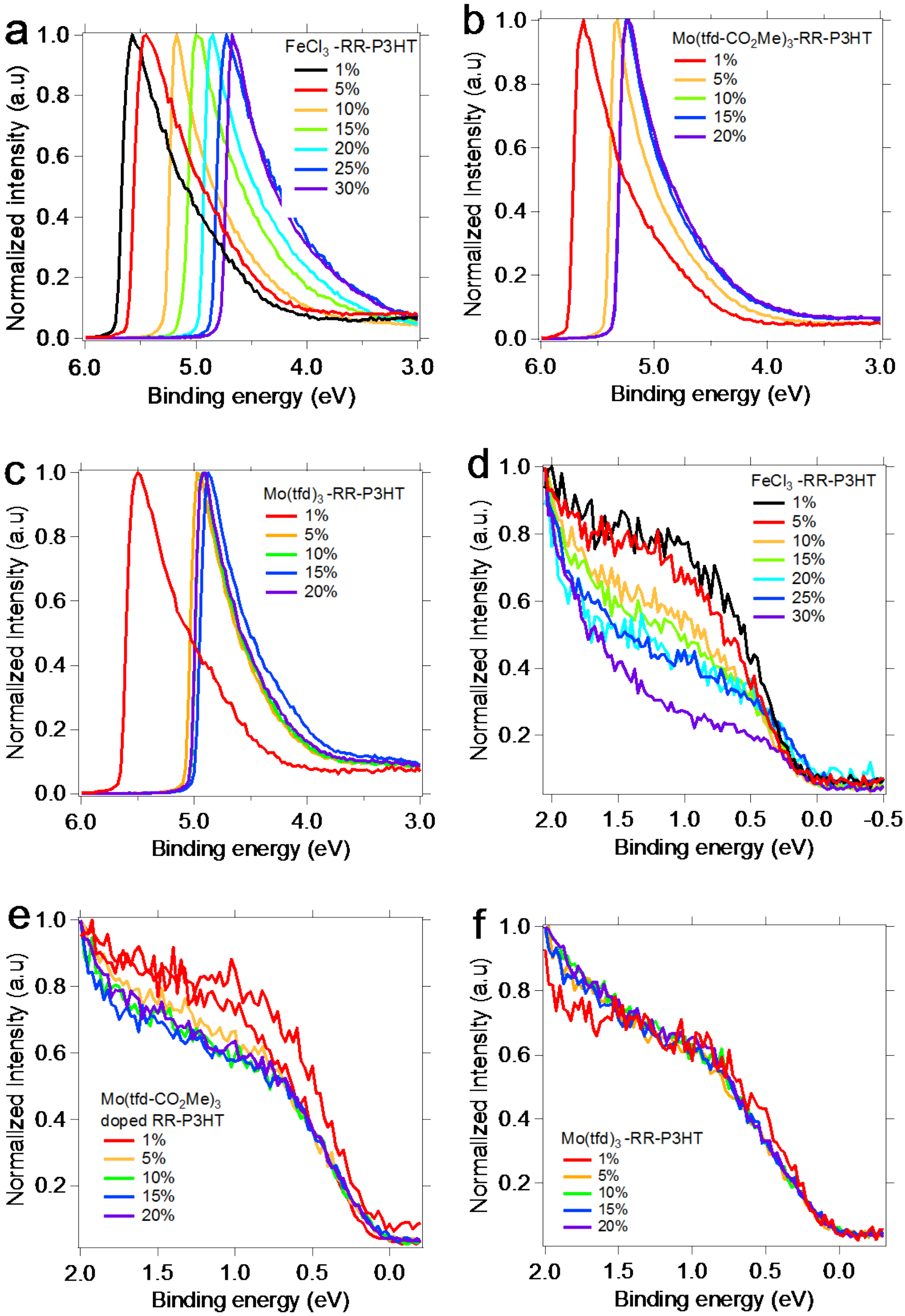
a
Normalized intensity (a.u)
Binding energy (eV)
$FeCl_3$ -RR-P3HT
1%
5%
10%
15%
20%
25%
30%
b
Normalized Instensity (a.u)
Binding energy (eV)
$Mo(tfd\text{-}CO_2Me)_3$-RR-P3HT
1%
5%
10%
15%
20%
c
Normalized Intensity (a.u)
Binding energy (eV)
$Mo(tfd)_3$ -RR-P3HT
1%
5%
10%
15%
20%
d
Normalized Intensity (a.u.)
Binding energy (eV)
$FeCl_3$ -RR-P3HT
1%
5%
10%
15%
20%
25%
30%
e
Normalized Intensity (a.u)
Binding energy (eV)
$Mo(tfd\text{-}CO_2Me)_3$
doped RR-P3HT
1%
5%
10%
15%
20%
f
Normalized Intensity (a.u)
Binding energy (eV)
$Mo(tfd)_3$ -RR-P3HT
1%
5%
10%
15%
20%
1.0
0.8
0.6
0.4
0.2
0.0
6.0
5.0
4.0
3.0
2.0
1.5
1.0
0.5
0.0
-0.5

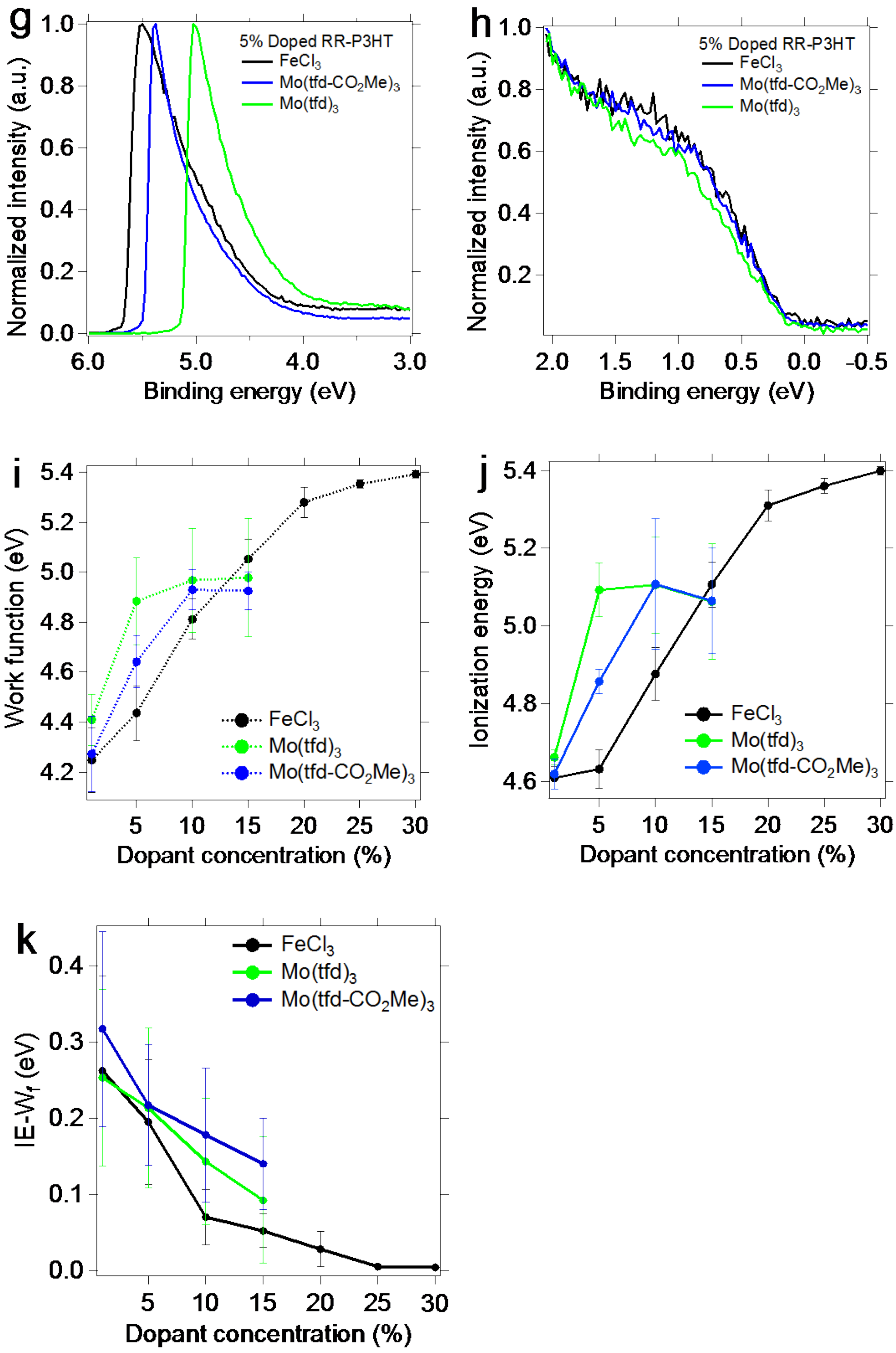

Figure 4.12 SECO and HOMO onset of $FeCl_3$(a,d), $Mo(tfdCO_2Me)_3$ (b,e), and $Mo(tfd)_3$ (c,f) doped RR-P3HT, 5% $FeCl_3$, $Mo(tfdCO_2Me)_3$, and $Mo(tfd)_3$ SECO (g) and HOMO onset(h), Work function (i), Ionization energy (j), and IE-W_f (k) of RR-P3HT doped with $FeCl_3$, $Mo(tfd)_3$, and $Mo(tfdCO_2Me)_3$ extracted from the UPS spectra.

In addition to RR-P3HT, we also looked at the influence of Mo(tfd)$_3$ and FeCl$_3$ on the thermoelectric performance of PDPP-4T, as shown in Figure 4.13. In PDPP-4T, FeCl$_3$ at low concentrations is not an effective dopant, as the electrical conductivity is two orders of magnitude lower than when Mo(tfd)$_3$ is used at the same dopant concentration. In support of the claim that σ is low for FeCl$_3$ doped PDPP-4T due to inefficient doping, we see that the Seebeck coefficient at 4% FeCl$_3$ doping is approximately four times greater than the Seebeck coefficient at 4% Mo(tfd)$_3$ doping. This contrasts with the results observed for the two dopants in RR-P3HT, where similar Seebeck coefficients were observed with both dopants at low concentrations. These trends in the Seebeck coefficient are in line with expectations of doping based on the polymer IE – dopant EA differences.

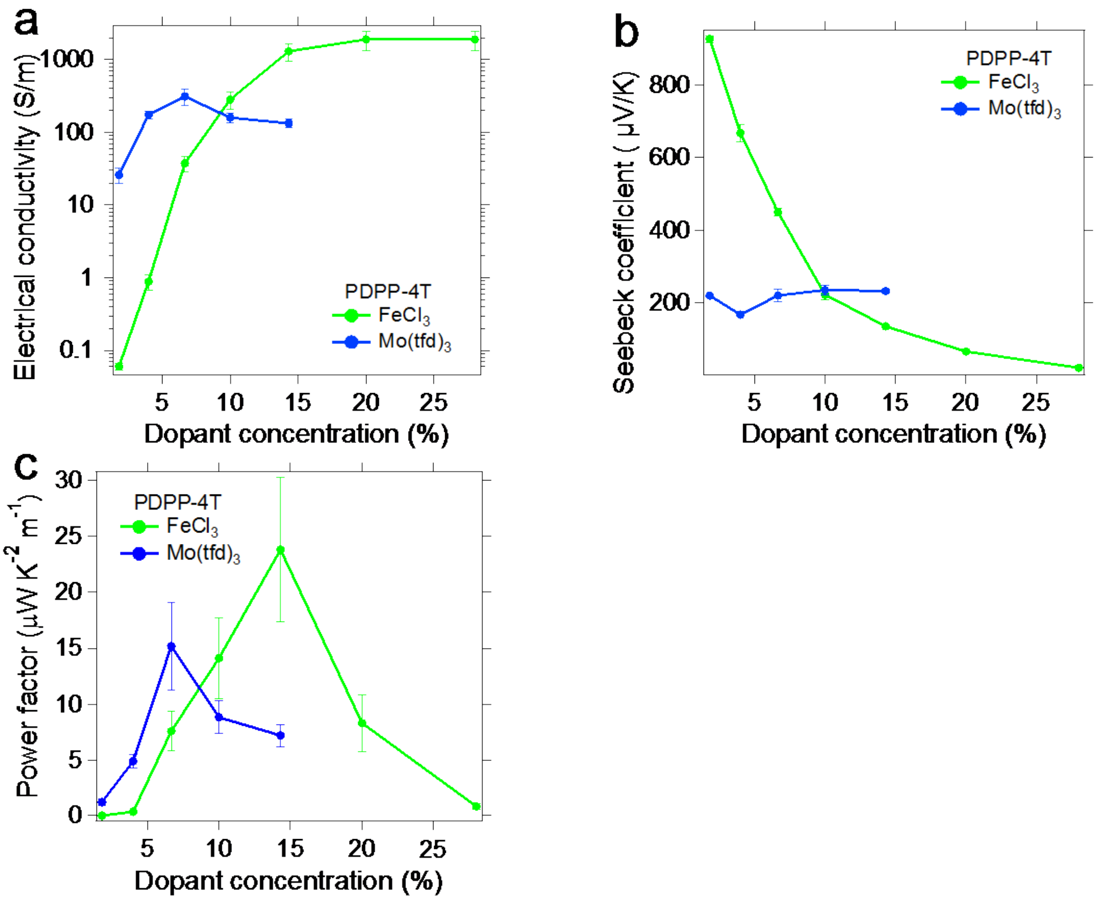

Figure 4.13 Electrical conductivity vs. dopant concentration (a), Seebeck coefficient vs. dopant concentration (b), and power factor vs. dopant concentration (c) for solution processing doped PDPP-4T with Mo(tfd)$_3$, and FeCl$_3$.

Like RR-P3HT, the power factor for Mo(tfd)$_3$ doped PDPP-4T also peaks at a relatively low dopant concentration of 6.7%, with the power factor reaching a respectable value of 15 μW K^{-2}m^{-1}, which is nearly five times greater than the maximum power factor obtained with FeCl$_3$ doped RR-P3HT. We attribute this peak in power factor at low concentrations to the plateau in electrical conductivity. As with RR-P3HT, we suspect that this saturation in σ results from limited miscibility of Mo(tfd)$_3$ in PDPP-4T. Surprisingly, PDPP-4T doped with FeCl$_3$ does reach high electrical conductivities of 1900 S/m at a FeCl$_3$ concentration of 20%, as compared to the maximum σ of 310 S/m obtained with Mo(tfd)$_3$ doping. Furthermore, the power factor of PDPP-4T with FeCl$_3$ doping surpasses that of PDPP-4T with Mo(tfd)$_3$ doping, reaching a value of 24 μW K^{-2}m^{-1} at a doping concentration of 14.3%. These results show that despite the low EA of FeCl$_3$, it can still be an efficient dopant for higher IE polymers when used at high concentrations.

4.2.5 Mixed Dopants for Improved Power Factors

The power factors for RR-P3HT films doped with Mo(tfd)$_3$ appear limited by the saturation of the polaron density in RR-P3HT at only 5 to 10% dopant concentration. Thus, the power factor reaches a maximum at 10% doping with Mo(tfd)$_3$ as opposed to 20% with FeCl$_3$. Hypothetically both Mo(tfd)$_3$ and FeCl$_3$ may be used simultaneously to dope P3HT and take advantage of the higher power factors achieved with Mo(tfd)$_3$ and the ability of FeCl$_3$ to more heavily dope RR-P3HT. Furthermore, FeCl$_3$ can likely intercalate into the crystalline regions, whereas Mo(tfd)$_3$ likely remains outside of the crystalline regions as discussed previously. Thus, these dopants present potentially complementary properties. To explore whether a mixed FeCl$_3$ and Mo(tfd)$_3$ dopant system may allow for higher thermoelectrical performance, we used 5% Mo(tfd)$_3$ with 5 to 25% FeCl$_3$. The electrical conductivities, Seebeck coefficients, and power factors of RR-P3HT with this mixed dopant system are shown in Figure 4.14.

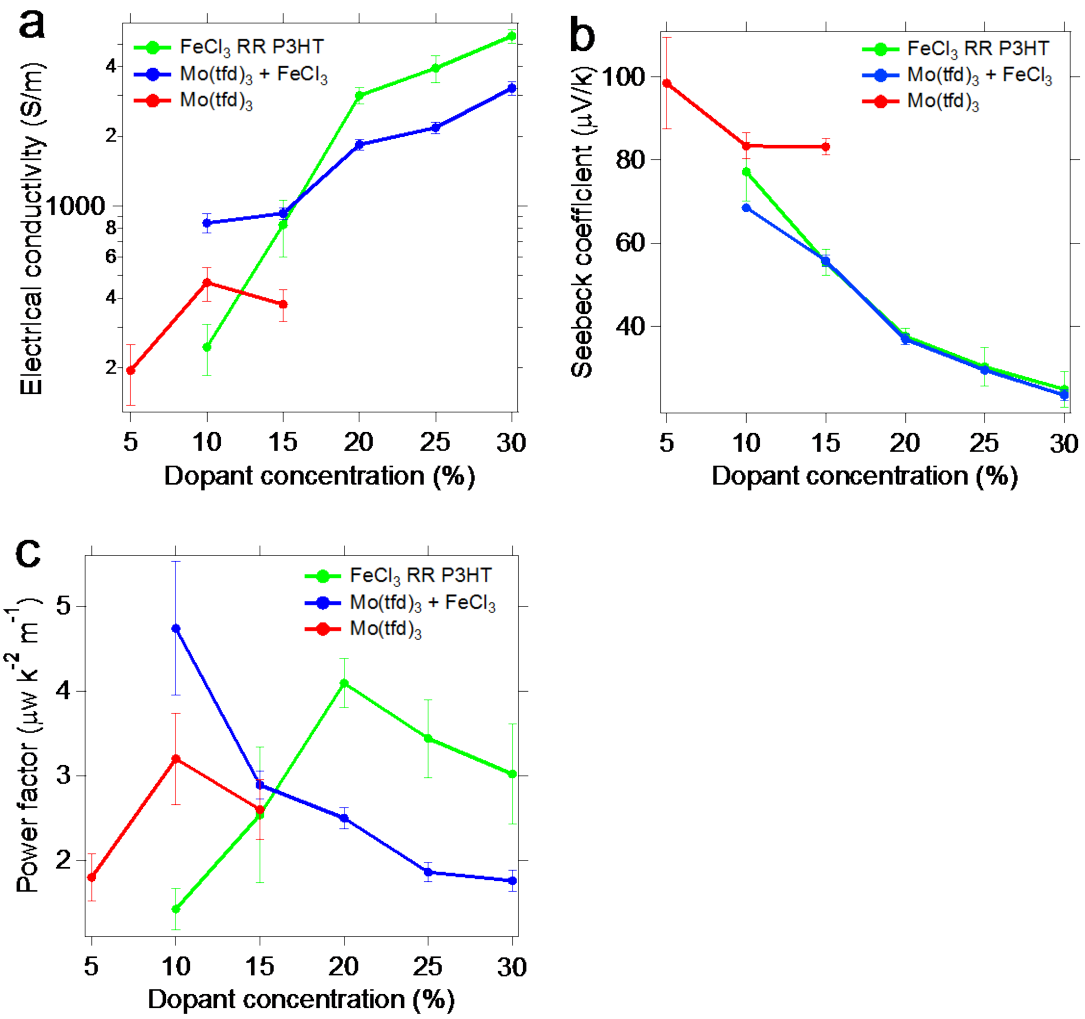

Figure 4.14 $Mo(tfd)_3$ and $FeCl_3$ mixed doped RR-P3HT electrical conductivity (a) Seebeck coefficient (b) and power factor (c).

At a total doping concentration of 10%, the mixed dopant film shows *ca.* 80% higher electrical conductivity than with only $Mo(tfd)_3$ and 250% higher than with only $FeCl_3$. Additionally, α for this mixed dopant film is only 10% lower than with only $FeCl_3$. As a result, the mixed dopant film does lead to the highest power factors for RR-P3HT observed in our hands. Additionally, relative to $FeCl_3$ as the only dopant, the use of mixed dopants reduces the amount of dopant necessary to reach the maximum power factor. As larger amounts of dopants can lead to poor film morphologies and decrease stability due to dopant diffusion, lower doping concentrations may be advantageous for the development of organic thermoelectrics.

4.3 Conclusions

We find that the electrical conductivities of πCPs with low dopant concentrations are strongly influenced by the polymer IE – dopant EA difference; however, we find that at higher dopant loadings even low EA dopants can lead to high electrical conductivities. The fact that $FeCl_3$, with a reduction potential of 4.6 eV vs. vacuum can be used to dope PDPP-4T, which has an ionization energy of 4.98 eV, and lead to electrical conductivities of nearly 2000 S/m is unexpected and shows that dopants with low EAs can still efficiently dope higher IE polymers. For all the πCPs investigated, we find that the electrical conductivity with $Mo(tfd)_3$ doping saturates at relatively low dopant concentrations of between 5 and 10% dopant per aromatic ring in the polymer backbone. At these low dopant concentrations the electrical conductivity of the πCPs with $Mo(tfd)_3$ doping are 10 to 800 times greater than the electrical conductivities with $FeCl_3$ for the same polymer. We attribute the enhanced electrical conductivity with $Mo(tfd)_3$ to higher doping efficiency owing to the high EA, and also to increased polaron delocalization afforded by the larger dopant size and thus a decreased coulomb interaction energy between the polaron and dopant anion. Overall, our results suggest that if the Mo complexes could effectively dope πCPs at higher dopant loadings, then superior electrical and thermoelectric properties should be achievable. In general, high EA dopants with large sizes that are highly miscible with conjugated polymers may provide a route to achieve high doping efficiencies at high dopant loadings. However, large dopants may also disrupt the crystallinity of πCPs at high loadings, thus further complicating the design of new dopants. As suggested in this paper, mixing small and large dopants may provide an approach to improving the thermoelectric performance of πCPs.

4.4 EXPERIMENTAL Details

Materials

RR-P3HT and RRa-P3HT(rieke metals); iron(III) chloride (anhydrous, 98%, crystalline, alfa aesar); chloroform (anhydrous, DriSolv); acetonitrile (>99.5%, sigma-aldrich); chlorobenzene (anhydrous, driSolv); bismuth(99.99%, kurt J.lesker)

Doping process

Solution processing doping

P3HT was dissolved in chloroform with a concentration of 15 mg/ml; PDPP 4T, PDPP-T-TT-T, $FeCl_3$, and $Mo(tfdCO_2Me)_3$ (chloroform, 5mg/ml); $Mo(tfd)_3$ (chloroform, 3mg/ml). The doped solution was stirred on hotplate at 40 ˚C for 10 hours. Films were fabricated by drop-cast method. Films thickness ranges from 2~4 µm. All operation finished in nitrogen filled glovebox with H_2O < 0.1ppm, and O_2 < 0.1 ppm.

Sequential processing doping

RR-P3HT was dissolved in chlorobenzene with a concentration of 15 mg/ml; $FeCl_3$, and $Mo(tfdCO_2Me)_3$ (acetonitrile , 5mg/ml). RR-P3HT was spin-cast at 3000 rpm for 30 seconds; then $FeCl_3$, or $Mo(tfdCO_2Me)_3$ solutions was added on RR-P3HT films, waited for 10 seconds, spin at 3000 rpm for 30 seconds. Films thickness ranges from 40~60 nm. All operation finished in nitrogen filled glovebox with H_2O < 0.1ppm, and O_2 < 0.1 ppm.

Film characterization

Ultraviolet photoelectron spectroscopy(UPS)

Excitech H Lyman-α photon source (E-LUX^{TM}121) coupled with a 90^{o} ellipsoidal mirror (E-LUX^{TM} EEM Optical Module) was used to characterize samples. Negatively -5V biased was added during UPS measurements and the pass energy was 5 eV. All samples were checked under a dry nitrogen purge of the beam path at 7.5 - 8.5 Torr.[131]

Grazing-incidence X-ray diffraction (GIXRD)

GIXRD measurements were carried out at the 11-BM Complex Materials Scattering (CMS) beamline of the National Synchrotron Light Source II (NSLS-II), Brookhaven National Laboratory. The x-ray with the wavelength of 0.0918 nm shone on the thin film samples at the incident angle of 0.15^{o}. An in-vacuum CCD (Photonic Science) detector was tilted ~19° from the incident X-ray beam direction and located 227mm away from the samples, which were calibrated by silver behenate. The measurements were performed in vacuum with the exposure time of 10 s. The plot of intensity vs q were integrated in the cake slice of 30^o along Qz and Qxy. The data was analyzed by SciAnalysis. (http://gisaxs.com/index.php/SciAnalysis).(This part was contributed by Ruipeng Li from Brookhaven National Laboratory)

Electrical conductivity measurement

Sheet resistance was measured with a four-point probe setup (Signatone S302-4, Keithley 2450 source meter); film thicknesses were measured with a Dektak D6M/32 profilometer.[80]

Seebeck coefficient measurement

A custom-built setup was used to check Seebeck coefficient (more information in our previously report).[80] 100 nm bismuth (calibrated α = -62.1 µV/K) and 50 nm of gold which work as the electrodes and electrical contact pads was thermally evaporated.

Optical spectra measurement

UV-Vis absorbance spectra were measured with an Ocean Optics QE Pro high performance spectrometer; Raman spectra were measured with thermo scientific DXR Smart-Raman.

CV measurement

All electrochemical measurements were conducted in a single-compartment electrochemical cell with three electrodes: working electrode (glassy carbon, geometric area of 0.07 cm^2), reference electrode (Ag/AgCl) and the counter electrode (Pt wire). Cyclic voltammetric (CV) and linear sweep voltammetric(LSV) curves were recorded by an electrochemical workstation (CHI-760D, CH Instruments, Austin, TX). The electrolyte is N_2 saturated 0.1 M NBu_4PF_6 (in chloroform) with N_2 saturated works as the electrolyte. All sample was checked with ca. concentration 0.2mM and scan speed of 50mV*S^{-1}.

CHAPTER 5 CONCLUSION AND PERSPECTIVES

Charge transport in metals and inorganic semiconductors are relatively well understood in the past decades. Many models and experiments were built and carried out to help clarify the mechanism of charge transport. To further understand the factors influencing charge transport in nanowires, conjugated polymers, and nanowire-polymer composites, different experiments were carried out in this dissertation which included manipulating nanowires and conjugated polymers morphology (e.g. crystallinity) and energetics by surface modification and molecular doping.

Transparent electrodes of AgNWs and PEDOT:PSS nanocomposites: Thiols with various functional groups (e.g. hydrophobic and ionic) modified AgNWs were investigated. The experiment showed the polarity of thiols influenced morphological and electrical properties of both AgNW/PEDOT:PSS blend films and pure AgNWs networks. By utilizing sodium 3-mercapto-1-propanesulfonate (MPS) to modify AgNWs, the quality of AgNW/PEDOT:PSS films are more homogeneous and the sheet resistance is an order of magnitude lower than unmodified AgNWs at similar transmittance values. Brief optimization of MPS-AgNW/PEDOT:PSS blends yielded a sheet resistance of 22.6 Ω/square at 81.4% transmittance. The facile surface modification of nanowires opens up a variety of promising future uses. These could include controllably altering the work function of nanowires by controlling the dipole moment and direction of the surface modifier, altering dispersability of nanowires for utilization in multistep solution processed devices where orthogonal solvents are needed, and increasing compatibility with various polymers to create electrically conductive polymer films with mechanical properties such as flexibility or strechability.

Thermoelectric properties of TeNWs and P3HT nanocomposites: The energetic barrier between transport states in the conjugated polymer poly(3-hexylthiophene)(P3HT) and tellurium nanowires(TeNWs) was adjusted from 0.08 to

0.88 eV by altering the concentration of the p-type dopant ($FeCl_3$) present in the polymer phase. We showed that the maximum power factors in these composites are increased beyond either the pure polymer or pure nanowires for barriers of both 0.08 and 0.88 eV. With both doping concentrations, the Seebeck coefficient increased as more tellurium nanowires were added. By comparing the experimentally measured Seebeck coefficients with parallel and series models, we determined that the enhanced Seebeck coefficients and power factors did not likely arise from energy filtering. Furthermore, we found that the electrical conductivity of the 5% $FeCl_3$ doped blend can exceed that of either of the pure components by nearly an order of magnitude. The results further highlight how understanding and manipulating the nano- to molecular-scale charge transfer processes may provide a route to higher performing TE nanocomposites.

Dopant size and electron affinity effect to conjugated polymers electrical and thermoelectrical properties: A series of dopants with varying sizes and electron affinities, combined with a family of polymers with different ionization energies, were used to investigate how the difference between the polymer ionization energy and dopant electron affinity influences the doping efficiency and electrical conductivity. In addition, we investigated size of the dopant influenced the thermoelectric properties. Our experiments demonstrated that: i) at low doping levels the electrical conductivities and power factors increased with the EA of the dopant; ii) the effectiveness of doping drastically decreased at high loadings for the Mo complexes, while $FeCl_3$ remained effective at high loading; and iii) the doping efficiency was highly dependent on the difference between the polymer IE and dopant EA. To take advantage of the complementary doping characteristics of $Mo(tfd)_3$ and $FeCl_3$, we used both dopants simultaneously to reach high electrical conductivities and power factors at relatively low dopant concentrations. As larger amounts of dopants can lead to poor film morphologies and decrease stability due to dopant diffusion, lower doping concentrations may be advantageous for the future development of organic thermoelectrics. Meanwhile, as suggested by the result, mixing small and large dopants may provide an approach to improve the thermoelectric performance of πCPs.

These projects provide potential routes to understand and manipulate the nano-to- molecular scale charge transfer processes. They will further inspire researchers to fabricate high performance organic-inorganic nanocomposites and design new effective dopants for conjugated polymers doping.

REFERENCES

(1) Omer, A. M. *Renewable and Sustainable Energy Reviews* **2008**, *12*, 2265-2300.

(2) Dincer, I. *Energy Policy* **1999**, *27*, 845-854.

(3) Tilman, D.; Socolow, R.; Foley, J. A.; Hill, J.; Larson, E.; Lynd, L.; Pacala, S.; Reilly, J.; Searchinger, T.; Somerville, C.; Williams, R. *Science* **2009**, *325*, 270-271.

(4) Searchinger, T.; Heimlich, R.; Houghton, R. A.; Dong, F.; Elobeid, A.; Fabiosa, J.; Tokgoz, S.; Hayes, D.; Yu, T.-H. *Science* **2008**, *319*, 1238-1240.

(5) Lasi, H.; Fettke, P.; Kemper, H.-G.; Feld, T.; Hoffmann, M. *wirtschaftsinformatik* **2014**, *56*, 261-264.

(6) Liu, S. X. *Design Management Review* **2016**, *27*, 52-58.

(7) Lin, C.-C.; Yang, C.-H.; Shyua, J. Z. *Energy Policy* **2013**, *57*, 119-132.

(8) Sims, R. E. H.; Rogner, H.-H.; Gregory, K. *Energy Policy* **2003**, *31*, 1315-1326.

(9) Rhodes, C. J. *Sci. Prog.* **2010**, *93*, 37-112.

(10) Turner, J. A. *Science* **1999**, *285*, 687-689.

(11) Shirota, Y.; Kageyama, H. *Chem. Rev.* **2007**, *107*, 953-1010.

(12) Paulo, A. S.; Bokor, J.; Howe, R. T.; He, R.; Yang, P.; Gao, D.; Carraro, C.; Maboudian, R. *Appl. Phys. Lett.* **2005**, *87*, 053111.

(13) Qian, C.; Kim, F.; Ma, L.; Tsui, F.; Yang, P.; Liu, J. *J. Am. Chem. Soc.* **2004**, *126*, 1195-1198.

(14) Wu, J.-J.; Liu, S.-C. *J. Phys. Chem. B* **2002**, *106*, 9546-9551.

(15) Ran, Y.; He, W.; Wang, K.; Ji, S.; Ye, C. *Chem. Commun.* **2014**, *50*, 14877-14880.

(16) Yang, L.; Zhang, T.; Zhou, H.; Price, S. C.; Wiley, B. J.; You, W. *ACS Appl. Mater. Interfaces* **2011**, *3*, 4075-4084.

(17) Li, B.; Ye, S.; Stewart, I. E.; Alvarez, S.; Wiley, B. J. *Nano Lett.* **2015**, *15*, 6722-6726.

(18) Brown, P. R.; Kim, D.; Lunt, R. R.; Zhao, N.; Bawendi, M. G.; Grossman, J. C.; Bulović, V. *ACS Nano* **2014**, *8*, 5863-5872.

(19) Forrest, S. R. *Nature* **2004**, *428*, 911.

(20) Lüssem, B.; Riede, M.; Leo, K. *Phys. Status Solidi A* **2013**, *210*, 9-43.

(21) Wang, C.; Dong, H.; Hu, W.; Liu, Y.; Zhu, D. *Chem. Rev.* **2012**, *112*, 2208-2267.

(22) Mei, J.; Diao, Y.; Appleton, A. L.; Fang, L.; Bao, Z. *J. Am. Chem. Soc.* **2013**, *135*, 6724-6746.

(23) Russ, B.; Glaudell, A.; Urban, J. J.; Chabinyc, M. L.; Segalman, R. A. *Nat. Rev. Mater.* **2016**, *1*, 16050.

(24) Zhang, Q.; Sun, Y.; Xu, W.; Zhu, D. *Adv. Mater.* **2014**, *26*, 6829-6851.

(25) Glaudell, A. M.; Cochran, J. E.; Patel, S. N.; Chabinyc, M. L. *Adv. Energy Mater.* **2015**, *5*, 1401072-n/a.

(26) Gupta, S. K.; Jha, P.; Singh, A.; Chehimi, M. M.; Aswal, D. K. *J. Mater. Chem. C* **2015**, *3*, 8468-8479.

(27) Mei, J.; Bao, Z. *Chem. Mater.* **2014**, *26*, 604-615.

(28) He, M.; Ge, J.; Lin, Z.; Feng, X.; Wang, X.; Lu, H.; Yang, Y.; Qiu, F. *Energ. Environ. Sci.* **2012**, *5*, 8351-8358.

(29) Scholes, D. T.; Yee, P. Y.; Lindemuth, J. R.; Kang, H.; Onorato, J.; Ghosh, R.; Luscombe, C. K.; Spano, F. C.; Tolbert, S. H.; Schwartz, B. J. *Adv. Funct. Mater.* **2017**, *27*, 1702654.

(30) Choi, D. Y.; Kang, H. W.; Sung, H. J.; Kim, S. S. *Nanoscale* **2013**, *5*, 977-983.

(31) Kango, S.; Kalia, S.; Celli, A.; Njuguna, J.; Habibi, Y.; Kumar, R. *Prog. Polym. Sci.* **2013**, *38*, 1232-1261.

(32) Gao, J.; Huang, X.; Liu, H.; Zan, F.; Ren, J. *Langmuir* **2012**, *28*, 4464-4471.

(33) Park, Y.; Choong, V.; Gao, Y.; Hsieh, B. R.; Tang, C. W. *Appl. Phys. Lett.* **1996**, *68*, 2699-2701.

(34) Huber, E. E.; Kirk, C. T. *Surf. Sci.* **1966**, *5*, 447-465.

(35) Albers, H; MDroog, J.M.; Bootsma, G.A. *Surf. Sci.* **1977**, *64*, 1.

(36) Sachtler, W. M. H.; Dorgelo, G. J. H.; Holscher, A. A. *Surf. Sci.* **1966**, *5*, 221-229.

(37) Satterthwaite, C. B.; Ure, R. W. *Phys. Rev.* **1957**, *108*, 1164-1170.

(38) Choi, J.; Lee, K.; Park, C. R.; Kim, H. *Carbon* **2015**, *94*, 577-584.

(39) Lin, S.; Li, W.; Chen, Z.; Shen, J.; Ge, B.; Pei, Y. *Nat. Commun.* **2016**, *7*, 10287.

(40) Yamamoto, J.; Furukawa, Y. *J. Phys. Chem. B* **2015**, *119*, 4788-4794.

(41) Huang, F.; MacDiarmid, A. G.; Hsieh, B. R. *Appl. Phys. Lett.* **1997**, *71*, 2415-2417.

(42) Kahn, A. *Mater. Horiz.* **2016**, *3*, 7-10.

(43) Chandrasekhar, B. S. *J. Phys. Chem. Solids* **1959**, *11*, 268-273.

(44) Dresselhaus, M. S.; Chen, G.; Tang, M. Y.; Yang, R. G.; Lee, H.; Wang, D. Z.; Ren, Z. F.; Fleurial, J. P.; Gogna, P. *Adv. Mater.* **2007**, *19*, 1043-1053.

(45) Venkatasubramanian, R.; Siivola, E.; Colpitts, T.; O'Quinn, B. *Nature* **2001**, *413*, 597-602.

(46) Balandin, A.; Wang, K. L. *J. Appl. Phys.* **1998**, *84*, 6149-6153.

(47) Hicks, L. D.; Dresselhaus, M. S. *Phys. Rev. B* **1993**, *47*, 12727-12731.

(48) Tian, Y.; Sakr, M. R.; Kinder, J. M.; Liang, D.; MacDonald, M. J.; Qiu, R. L. J.; Gao, H.-J.; Gao, X. P. A. *Nano Lett.* **2012**, *12*, 6492-6497.

(49) Hicks, L. D.; Harman, T. C.; Sun, X.; Dresselhaus, M. S. *Phys. Rev. B* **1996**, *53*, R10493-R10496.

(50) Faleev, S. V.; Léonard, F. *Phys. Rev. B* **2008**, *77*, 214304.

(51) Kishimoto, K.; Tsukamoto, M.; Koyanagi, T. *J. Appl. Phys.* **2002**, *92*, 5331-5339.

(52) Narducci, D.; Selezneva, E.; Cerofolini, G.; Frabboni, S.; Ottaviani, G. *J. Solid State Chem.* **2012**, *193*, 19-25.

(53) Zhang, Y.; Stucky, G. D. *Chem. Mater.* **2014**, *26*, 837-848.

(54) Popescu, A.; Woods, L. M.; Martin, J.; Nolas, G. S. *Phys. Rev. B* **2009**, *79*, 205302.

(55) Heremans, J. P.; Thrush, C. M.; Morelli, D. T. *Phys. Rev. B* **2004**, *70*, 115334.

(56) Liang, Z.; Graham, K. R. *ACS Appl. Mater. & Interfaces* **2015**, *7*, 21652-21656.

(57) Bonaccorso, F.; Sun, Z.; Hasan, T.; Ferrari, A. C. *Nat. Photonics* **2010**, *4*, 611-622.

(58) Ye, S.; Rathmell, A. R.; Chen, Z.; Stewart, I. E.; Wiley, B. J. *Adv. Mater.* **2014**, *26*, 6670-6687.

(59) Cairns, D. R.; Witte, R. P.; Sparacin, D. K.; Sachsman, S. M.; Paine, D. C.; Crawford, G. P.; Newton, R. R. *Appl. Phys. Lett.* **2000**, *76*, 1425-1427.

(60) Langley, D.; Giusti, G.; Mayousse, C.; Celle, C.; Bellet, D.; Simonato, J. P. *Nanotechnology* **2013**, *24*, 20.

(61) Li, L.; Yu, Z. B.; Hu, W. L.; Chang, C. H.; Chen, Q.; Pei, Q. B. *Adv. Mater.* **2011**, *23*, 5563-+.

(62) Hecht, D. S.; Heintz, A. M.; Lee, R.; Hu, L.; Moore, B.; Cucksey, C.; Risser, S. *Nanotechnology* **2011**, *22*, 169501.

(63) Blackburn, J. L.; Barnes, T. M.; Beard, M. C.; Kim, Y. H.; Tenent, R. C.; McDonald, T. J.; To, B.; Coutts, T. J.; Heben, M. J. *ACS Nano* **2008**, *2*, 1266-1274.

(64) Rowell, M. W.; Topinka, M. A.; McGehee, M. D.; Prall, H.-J. r.; Dennler, G.; Sariciftci, N. S.; Hu, L.; Gruner, G. *Appl. Phys. Lett.* **2006**, *88*, 233506.

(65) Ning, J.; Wang, D.; Zhang, C.; Wang, Z.; Tang, S.; Chen, D.; Shi, Y.; Zhang, J.; Hao, Y. *Synth. Met.* **2015**, *203*, 215-220.

(66) De, S.; Higgins, T. M.; Lyons, P. E.; Doherty, E. M.; Nirmalraj, P. N.; Blau, W. J.; Boland, J. J.; Coleman, J. N. *ACS Nano* **2009**, *3*, 1767-1774.

(67) Chang, M. H.; Cho, H. A.; Kim, Y. S.; Lee, E. J.; Kim, Y. J. *Nanoscale Res. Lett.* **2014**, *9*, 7.

(68) Ye, S. R.; Rathmell, A. R.; Stewart, I. E.; Ha, Y. C.; Wilson, A. R.; Chen, Z. F.; Wiley, B. J. *Chem. Commun.* **2014**, *50*, 2562-2564.

(69) Sachse, C.; Weiss, N.; Gaponik, N.; Muller-Meskamp, L.; Eychmuller, A.; Leo, K. *Adv. Energy Mater.* **2014**, *4*, 6.

(70) Hsu, P. C.; Kong, D. S.; Wang, S.; Wang, H. T.; Welch, A. J.; Wu, H.; Cui, Y. *J. Am. Chem. Soc.* **2014**, *136*, 10593-10596.

(71) Gaynor, W.; Burkhard, G. F.; McGehee, M. D.; Peumans, P. *Adv. Mater.* **2011**, *23*, 2905-2910.

(72) Zeng, X. Y.; Zhang, Q. K.; Yu, R. M.; Lu, C. Z. *Adv. Mater.* **2010**, *22*, 4484-4488.

(73) Kim, Y.-S.; Chang, M.-H.; Lee, E.-J.; Ihm, D.-W.; Kim, J.-Y. *Synth. Met.* **2014**, *195*, 69-74.

(74) Hsiao, S.-T.; Tien, H.-W.; Liao, W.-H.; Wang, Y.-S.; Li, S.-M.; Mma, C.-C.; Yu, Y.-H.; Chuang, W.-P. *J. Mater. Chem.C* **2014**, *2*, 7284.

(75) Andrew, P.; Ilie, A. *J. Phys.: Conf. Ser.* **2007**, *61*, 36-40.

(76) Sun, Y. G.; Gates, B.; Mayers, B.; Xia, Y. N. *Nano Lett.* **2002**, *2*, 165-168.

(77) Jiu, J.; Araki, T.; Wang, J.; Nogi, M.; Sugahara, T.; Nagao, S.; Koga, H.; Suganuma, K.; Nakazawa, E.; Hara, M.; Uchida, H.; Shinozaki, K. *J. Mater. Chem.A* **2014**, *2*, 6326.

(78) Lee, J.; Lee, P.; Lee, H.; Lee, D.; Lee, S. S.; Ko, S. H. *Nanoscale* **2012**, *4*, 6408-6414.

(79) Ran, Y.; He, W.; Wang, K.; Ji, S.; Ye, C. *Chem. Commun.* **2014**, *50*, 14877-14880.

(80) Liang, Z.; Boland, M. J.; Butrouna, K.; Strachan, D. R.; Graham, K. R. *J. Mater. Chem. A* **2017**, *5*, 15891-15900.

(81) Nielsch, K.; Bachmann, J.; Kimling, J.; Böttner, H. *Adv. Energy Mater.* **2011**, *1*, 713-731.

(82) Biswas, K.; He, J.; Blum, I. D.; Wu, C.-I.; Hogan, T. P.; Seidman, D. N.; Dravid, V. P.; Kanatzidis, M. G. *Nature* **2012**, *489*, 414-418.

(83) DiSalvo, F. J. *Science* **1999**, *285*, 703-706.

(84) Yee, S. K.; LeBlanc, S.; Goodson, K. E.; Dames, C. *Energ. Environ. Sci.* **2013**, *6*, 2561-2571.

(85) Yadav, A.; Pipe, K. P.; Shtein, M. *J. Power Sources* **2008**, *175*, 909-913.

(86) Meng, C.; Liu, C.; Fan, S. *Adv. Mater.* **2010**, *22*, 535-539.

(87) Yu, C.; Choi, K.; Yin, L.; Grunlan, J. C. *ACS Nano* **2011**, *5*, 7885-7892.

(88) Hone, J.; Ellwood, I.; Muno, M.; Mizel, A.; Cohen, M. L.; Zettl, A.; Rinzler, A. G.; Smalley, R. E. *Phys. Rev. Lett.* **1998**, *80*, 1042-1045.

(89) Yoon, C. O.; Reghu, M.; Moses, D.; Heeger, A. J.; Cao, Y. *Phys. Rev. B* **1993**, *48*, 14080-14084.

(90) Shi, H.; Liu, C.; Xu, J.; Song, H.; Lu, B.; Jiang, F.; Zhou, W.; Zhang, G.; Jiang, Q. *ACS Appl. Mater. & Interfaces* **2013**, *5*, 12811-12819.

(91) Golsanamlou, Z.; Izadi Vishkayi, S.; Bagheri Tagani, M.; Rahimpour Soleimani, H. *Chem. Phys. Lett.* **2014**, *594*, 51-57.

(92) Park, H.; Lee, S. H.; Kim, F. S.; Choi, H. H.; Cheong, I. W.; Kim, J. H. *J. Mater. Chem. A* **2014**, *2*, 6532-6539.

(93) Bubnova, O.; Khan, Z. U.; Malti, A.; Braun, S.; Fahlman, M.; Berggren, M.; Crispin, X. *Nat Mater* **2011**, *10*, 429-433.

(94) Du, Y.; Shen, S. Z.; Cai, K.; Casey, P. S. *Prog. Polym. Sci.* **2012**, *37*, 820-841.

(95) Kroon, R.; Mengistie, D. A.; Kiefer, D.; Hynynen, J.; Ryan, J. D.; Yu, L.; Muller, C. *Chem. Soc. Rev.* **2016**, *45*, 6147-6164.

(96) Coates, N. E.; Yee, S. K.; McCulloch, B.; See, K. C.; Majumdar, A.; Segalman, R. A.; Urban, J. J. *Adv. Mater.* **2013**, *25*, 1629-1633.

(97) See, K. C.; Feser, J. P.; Chen, C. E.; Majumdar, A.; Urban, J. J.; Segalman, R. A. *Nano Lett.* **2010**, *10*, 4664-4667.

(98) He, M.; Qiu, F.; Lin, Z. *Energy Environ. Sci* **2013**, *6*, 1352-1361.

(99) Toshima, N.; Imai, M.; Ichikawa, S. *J. Electron. Mater.* **2011**, *40*, 898-902.

(100) Zaia, E. W.; Sahu, A.; Zhou, P.; Gordon, M. P.; Forster, J. D.; Aloni, S.; Liu, Y.-S.; Guo, J.; Urban, J. J. *Nano Letters* **2016**, *16*, 3352-3359.

(101) Ireland, R. M.; Liu, Y.; Guo, X.; Cheng, Y.-T.; Kola, S.; Wang, W.; Jones, T.; Yang, R.; Falk, M. L.; Katz, H. E. *Adv. Sci.* **2015**, *2*, 1500015.

(102) Du, Y.; Cai, K. F.; Chen, S.; Cizek, P.; Lin, T. *ACS Appl. Mater. Interfaces* **2014**, *6*, 5735-5743.

(103) Krishanu, C.; Mousumi, M.; Kajari, K.; Saibal, G.; Dipali, B. *Nanotechnology* **2013**, *24*, 215703.

(104) Behnia, K. *Oxford University Press* **2015**.

(105) Herrero, E.; Llorca, M. J.; Feliu, J. M.; Aldaz, A. *J. Electroanal. Chem.* **1995**, *394*, 161-167.

(106) Michaelson, H. B. *J. Appl. Phys.* **1977**, *48*, 4729-4733.

(107) Mansingh, A.; Garg, A. K. *J. Appl. Phys.* **1984**, *56*, 2315-2322.

(108) Lang, N. D.; Kohn, W. *Phys. Rev. B* **1971**, *3*, 1215-1223.

(109) Demuth, J. E.; Rhodin, T. N. *Surf. Sci.* **1974**, *45*, 249-307.

(110) Lang, N. D. *Phys. Rev. B* **1971**, *4*, 4234-4244.

(111) Sahni, V.; Perdew, J. P.; Gruenebaum, J. *Phys. Rev. B* **1981**, *23*, 6512-6523.

(112) Peng, H.; Kioussis, N.; Snyder, G. J. *Phys. Rev. B* **2014**, *89*, 195206.

(113) Dai, A.; Zhou, Y.; Shu, A. L.; Mohapatra, S. K.; Wang, H.; Fuentes-Hernandez, C.; Zhang, Y.; Barlow, S.; Loo, Y.-L.; Marder, S. R.; Kippelen, B.; Kahn, A. *Adv. Funct. Mater.* **2014**, *24*, 2197-2204.

(114) Ratcliff, E. L.; Lee, P. A.; Armstrong, N. R. *J. Mater. Chem.* **2010**, *20*, 2672-2679.

(115) Reenen, S. v.; Kemerink, M. *Org. Electron.* **2014**, *15*, 2250-2255.

(116) Zhang, Q.; Sun, Y.; Xu, W.; Zhu, D. *Energy Environ. Sci* **2012**, *5*, 9639-9644.

(117) Gelbstein, Y. *J. Appl. Phys.* **2009**, *105*, 023713.

(118) Varahramyan, K.; Verret, E. J. *Solid State Electron.* **1996**, *39*, 1601-1607.

(119) Srinivasan, V. S. S.; Inga, A. F.; Lion, A.; Anja, H.; Roman, K.; Konrad, K.; Michael, O.; Erlend, R.; Joerg, S. *Semicond. Sci. Technol.***2016**, *31*, 08LT01.

(120) Luo, L.-B.; Liang, F.-X.; Huang, X.-L.; Yan, T.-X.; Hu, J.-G.; Yu, Y.-Q.; Wu, C.-Y.; Wang, L.; Zhu, Z.-F.; Li, Q.; Jie, J.-S. *J. Nanopart. Res.* **2012**, *14*, 967.

(121) Chen, S.; Tsang, S.-W.; Lai, T.-H.; Reynolds, J. R.; So, F. *Adv. Mater.* **2014**, *26*, 6125-6131.

(122) Khelifi, S.; Decock, K.; Lauwaert, J.; Vrielinck, H.; Spoltore, D.; Piersimoni, F.; Manca, J.; Belghachi, A.; Burgelman, M. *J. Appl. Phys.* **2011**, *110*, 094509.

(123) Hodgson, J. N. *Journal of Physics and Chemistry of Solids* **1962**, *23*, 1737-1742.

(124) Young, K. F.; Frederikse, H. P. R. *J. Phys. Chem. Ref. Data* **1973**, *2*, 313-410.

(125) Sze, S.M., Ng, K.-K., *Physics of Semiconductor Devices*, Third edition, Wiley-Interscience, Hoboken, NJ, USA **2007**.

(126) Dinno, M. A.; Schwartz, M.; Giammara, B. *J. Appl. Phys.* **1974**, *45*, 3328-3331.

(127) P. Gonc¸alves, A. L., E. B.; Alves, E.; Barradas, N. P.; Franco, N.; Rouleau, O.; Godart, C. In *Springer* 2009.

(128) Feng, J.; Ellis, T. W. *Synth. Met.* **2003**, *135–136*, 55-56.

(129) Xi, G.; Liu, Y.; Wang, X.; Liu, X.; Peng, Y.; Qian, Y. *Cryst. Growth Des.* **2006**, *6*, 2567-2570.

(130) Finefrock, S. W.; Fang, H.; Yang, H.; Darsono, H.; Wu, Y. *Nanoscale* **2014**, *6*, 7872-7876.

(131) Boehm, A. M.; Wieser, J.; Butrouna, K.; Graham, K. R. *Org. Electron.* **2017**, *41*, 9-16.

(132) Rogacheva, E. I.; Grigorov, S. N.; Nashchekina, O. N.; Lyubchenko, S.; Dresselhaus, M. S. *Appl. Phys. Lett.* **2003**, *82*, 2628-2630.

(133) Das, V. D.; Soundararajan, N. *Phys. Rev. B* **1987**, *35*, 5990-5996.

(134) Rivnay, J.; Inal, S.; Salleo, A.; Owens, R. M.; Berggren, M.; Malliaras, G. G. *Nat. Rev. Mater.* **2018**, *3*, 17086.

(135) Günes, S.; Neugebauer, H.; Sariciftci, N. S. *Chem. Rev.* **2007**, *107*, 1324-1338.

(136) Li, M.; Gao, K.; Wan, X.; Zhang, Q.; Kan, B.; Xia, R.; Liu, F.; Yang, X.; Feng, H.; Ni, W.; Wang, Y.; Peng, J.; Zhang, H.; Liang, Z.; Yip, H.-L.; Peng, X.; Cao, Y.; Chen, Y. *Nat. Photonics* **2016**, *11*, 85.

(137) Gustafsson, G.; Cao, Y.; Treacy, G. M.; Klavetter, F.; Colaneri, N.; Heeger, A. J. *Nature* **1992**, *357*, 477.

(138) Walzer, K.; Maennig, B.; Pfeiffer, M.; Leo, K. *Chem. Rev.* **2007**, *107*, 1233-1271.

(139) Bubnova, O.; Khan, Z. U.; Malti, A.; Braun, S.; Fahlman, M.; Berggren, M.; Crispin, X. *Nat. Mater.* **2011**, *10*, 429.

(140) Shi, H.; Liu, C.; Jiang, Q.; Xu, J. *Adv. Electron. Mater.* **2015**, *1*, 1500017.

(141) Jacobs, I. E.; Aasen, E. W.; Oliveira, J. L.; Fonseca, T. N.; Roehling, J. D.; Li, J.; Zhang, G.; Augustine, M. P.; Mascal, M.; Moule, A. J. *J. Mater. Chem. C* **2016**, *4*, 3454-3466.

(142) Aziz, E. F.; Vollmer, A.; Eisebitt, S.; Eberhardt, W.; Pingel, P.; Neher, D.; Koch, N. *Adv. Mater.* **2007**, *19*, 3257-3260.

(143) Chang, J.-F.; Sakanoue, T.; Olivier, Y.; Uemura, T.; Dufourg-Madec, M.-B.; Yeates, S. G.; Cornil, J.; Takeya, J.; Troisi, A.; Sirringhaus, H. *Phys. Rev. Lett.* **2011**, *107*, 066601.

(144) Bolto, B. A.; McNeill, R.; Weiss, D. *Aust. J. Chem.* **1963**, *16*, 1090-1103.

(145) Bolto, B.; Weiss, D. *Aust. J. Chem.* **1963**, *16*, 1076-1089.

(146) Koizumi, H.; Dougauchi, H.; Ichikawa, T. *J. Phys. Chem. B* **2005**, *109*, 15288-15290.

(147) Qi, Y.; Sajoto, T.; Kröger, M.; Kandabarow, A. M.; Park, W.; Barlow, S.; Kim, E.-G.; Wielunski, L.; Feldman, L. C.; Bartynski, R. A.; Brédas, J.-L.; Marder, S. R.; Kahn, A. *Chem. Mater.* **2010**, *22*, 524-531.

(148) Yim, K.-H.; Whiting, G. L.; Murphy, C. E.; Halls, J. J. M.; Burroughes, J. H.; Friend, R. H.; Kim, J.-S. *Adv. Mater.* **2008**, *20*, 3319-3324.

(149) Duong, D. T.; Wang, C.; Antono, E.; Toney, M. F.; Salleo, A. *Org. Electron.* **2013**, *14*, 1330-1336.

(150) Pingel, P.; Neher, D. *Phys. Rev. B* **2013**, *87*, 115209.

(151) Méndez, H.; Heimel, G.; Winkler, S.; Frisch, J.; Opitz, A.; Sauer, K.; Wegner, B.; Oehzelt, M.; Röthel, C.; Duhm, S.; Többens, D.; Koch, N.; Salzmann, I. *Nat. Commun.* **2015**, *6*, 8560.

(152) Salzmann, I.; Heimel, G.; Oehzelt, M.; Winkler, S.; Koch, N. *Acc. Chem. Res.* **2016**, *49*, 370-378.

(153) Karpov, Y.; Erdmann, T.; Raguzin, I.; Al-Hussein, M.; Binner, M.; Lappan, U.; Stamm, M.; Gerasimov, K. L.; Beryozkina, T.; Bakulev, V.; Anokhin, D. V.; Ivanov, D. A.; Günther, F.; Gemming, S.; Seifert, G.; Voit, B.; Di Pietro, R.; Kiriy, A. *Adv. Mater.* **2016**, *28*, 6003-6010.

(154) Méndez, H.; Heimel, G.; Opitz, A.; Sauer, K.; Barkowski, P.; Oehzelt, M.; Soeda, J.; Okamoto, T.; Takeya, J.; Arlin, J.-B.; Balandier, J.-Y.; Geerts, Y.; Koch, N.; Salzmann, I. *Angew. Chem. Int. Ed.* **2013**, *52*, 7751-7755.

(155) Patel, S. N.; Glaudell, A. M.; Peterson, K. A.; Thomas, E. M.; O'Hara, K. A.; Lim, E.; Chabinyc, M. L. *Sci. Adv.* **2017**, 3(6): e1700434.

(156) Li, C.-Z.; Chueh, C.-C.; Ding, F.; Yip, H.-L.; Liang, P.-W.; Li, X.; Jen, A. K. Y. *Adv. Mater.* **2013**, *25*, 4425-4430.

(157) Schlitz, R. A.; Brunetti, F. G.; Glaudell, A. M.; Miller, P. L.; Brady, M. A.; Takacs, C. J.; Hawker, C. J.; Chabinyc, M. L. *Adv. Mater.* **2014**, *26*, 2825-2830.

(158) Kiefer, D.; Giovannitti, A.; Sun, H.; Biskup, T.; Hofmann, A.; Koopmans, M.; Cendra, C.; Weber, S.; Anton Koster, L. J.; Olsson, E.; Rivnay, J.; Fabiano, S.; McCulloch, I.; Müller, C. *ACS Energy Lett.* **2018**, *3*, 278-285.

(159) Qiu, L.; Liu, J.; Alessandri, R.; Qiu, X.; Koopmans, M.; Havenith, R. A.; Marrink, S. J.; Chiechi, R. C.; Anton Koster, L. J.; Hummelen, J. C. *J. Mater. Chem. A* **2017**, *5*, 21234-21241.

(160) Noriega, R.; Rivnay, J.; Vandewal, K.; Koch, F. P. V.; Stingelin, N.; Smith, P.; Toney, M. F.; Salleo, A. *Nat. Mater.* **2013**, *12*, 1038.

(161) Duong, D. T.; Phan, H.; Hanifi, D.; Jo, P. S.; Nguyen, T. Q.; Salleo, A. *Adv. Mater.* **2014**, *26*, 6069-6073.

(162) Winkler, S.; Amsalem, P.; Frisch, J.; Oehzelt, M.; Heimel, G.; Koch, N. *Mater. Horiz.* **2015**, *2*, 427-433.

(163) Chew, A. R.; Ghosh, R.; Shang, Z.; Spano, F. C.; Salleo, A. *J. Phys. Chem. Lett.* **2017**, *8*, 4974-4980.

(164) Salleo, A.; Kline, R. J.; DeLongchamp, D. M.; Chabinyc, M. L. *Adv. Mater.* **2010**, *22*, 3812-3838.

(165) Janata, J.; Josowicz, M. *Nat. Mater.* **2003**, *2*, 19.

(166) Wohlgenannt, M.; Jiang, X. M.; Vardeny, Z. V. *Phys. Rev.ming B* **2004**, *69*, 241204.

(167) Zhao, Y.; Zhao, X.; Roders, M.; Qu, G.; Diao, Y.; Ayzner, A. L.; Mei, J. *Chem. Mater.* **2015**, *27*, 7164-7170.

(168) Ha, J. S.; Kim, K. H.; Choi, D. H. *J. Am. Chem. Soc.* **2011**, *133*, 10364-10367.

(169) Li, Y.; Singh, S. P.; Sonar, P. *Adv. Mater.* **2010**, *22*, 4862-4866.

(170) Yoshida, H. *Chem. Phys. Lett.* **2012**, *539-540*, 180-185.

(171) Zhao, X.; Zhao, Y.; Ge, Q.; Butrouna, K.; Diao, Y.; Graham, K. R.; Mei, J. *Macromolecules* **2016**, *49*, 2601-2608.

(172) Guan, Z.-L.; Kim, J. B.; Wang, H.; Jaye, C.; Fischer, D. A.; Loo, Y.-L.; Kahn, A. *Org. Electron.* **2010**, *11*, 1779-1785.

(173) Qi, Y.; Sajoto, T.; Barlow, S.; Kim, E.-G.; Brédas, J.-L.; Marder, S. R.; Kahn, A. *J. Am. Chem. Soc.* **2009**, *131*, 12530-12531.

(174) Dai, A.; Zhou, Y.; Shu, A. L.; Mohapatra, S. K.; Wang, H.; Fuentes-Hernandez, C.; Zhang, Y.; Barlow, S.; Loo, Y. L.; Marder, S. R.; Kippelen, B.; Kahn, A. *Adv. Funct. Mater.* **2014**, *24*, 2197-2204.

(175) Cardona, C. M.; Li, W.; Kaifer, A. E.; Stockdale, D.; Bazan, G. C. *Adv. Mater.* **2011**, *23*, 2367-2371.

(176) Davison, A.; Edelstein, N.; Holm, R. H.; Maki, A. H. *J. Am. Chem. Soc.* **1964**, *86*, 2799-2805.

(177) Tietze, M. L.; Burtone, L.; Riede, M.; Lüssem, B.; Leo, K. *Phys. Rev. B* **2012**, *86*, 035320.

(178) Graham, K. R.; Cabanetos, C.; Jahnke, J. P.; Idso, M. N.; El Labban, A.; Ngongang Ndjawa, G. O.; Heumueller, T.; Vandewal, K.; Salleo, A.; Chmelka, B. F.; Amassian, A.; Beaujuge, P. M.; McGehee, M. D. *J. Am. Chem. Soc.* **2014**, *136*, 9608-9618.

(179) Bhattacharya, A.; De, A.; Bhattacharya, S. N.; Das, S. *J. Phys.: Condens. Matter* **1994**, *6*, 10499.

(180) Proń, A.; Kucharski, Z.; Budrowski, C.; Zagórska, M.; Krichene, S.; Suwalski, J.; Dehe, G.; Lefrant, S. *J. Chem. Phys.* **1985**, *83*, 5923-5927.

(181) Mohapatra, S. K.; Zhang, Y.; Sandhu, B.; Fonari, M. S.; Timofeeva, T. V.; Marder, S. R.; Barlow, S. *Polyhedron* **2016**, *116*, 88-95.

(182) Dunbar, K. R.; Quillevéré, A. *Angew. Chem. Int. Ed.* **1993**, *32*, 293-295.

(183) Louarn, G.; Trznadel, M.; Buisson, J. P.; Laska, J.; Pron, A.; Lapkowski, M.; Lefrant, S. *J. Phys. Chem.* **1996**, *100*, 12532-12539.

(184) Cutler, M.; Mott, N. F. *Phys. Rev.* **1969**, *181*, 1336-1340.

(185) Fritzsche, H. *Solid State Commun.* **1971**, *9*, 1813-1815.

VITA

Zhiming Liang was born in Xiangyang, Hubei, China. He received his bachelor degree (Chemistry) from Sichuan University, Chengdu, China. He joined in Dr. Kenneth R. Graham's group at University of Kentucky in July, 2014 for Ph.D study.

Publications

6. **Liang, Zhiming,** Graham, Kenneth. R**.** *et al*; "Crossover from positive to negative Seebeck coefficients in heavily p-doped conjugated polymers supports semi-metal character", *to be submitted,* **2018***.*
5. **Liang, Zhiming,** Yadong Zhang, Maryam Souri, Xuyi Luo, Alex M. Boehm, Ruipeng Li, Yan Zhang, Tairan Wang, Doo-Young Kim, Jianguo Mei, Seth R. Marder, Kenneth R. Graham "Influence of Dopant Size and Electron Affinity on the Electrical Conductivity and Thermoelectric Properties of Conjugated Polymers", *submitted,* **2018***.*
4. Pan Xia, **Zhiming Liang**, Melika Mahboub, Jeremiah van Baren, Chun Hung Lui, Jieying Jiao, Kenneth R. Graham and Ming Lee Tang* Surface Fluorination for Controlling PbS Quantum Dot Bandgap and Band Offset, *Chem. Mater,* **2018**. *(Under revision).*
3. So Min Park, Samuel M. Mazza, **Zhiming Liang**, Ashkan Abtahi, Alex M. Boehm, Sean R. Parkin, John E. Anthony, and Kenneth R. Graham. Processing Dependent Influence of the Hole Transport Layer Ionization Energy on Methylammonium Lead Iodide Perovskite Photovoltaics. *ACS Appl. Mater. Interfaces* **2018***,* 10(18), 15548.
2. **Liang, Zhiming**, Boland, Mathias J., Butrouna, Kamal, Strachan, Douglas R., Graham, Kenneth R**.** "Increased power factors of organic-inroganic nano-composite thermoelectric materials and the role of energy filtering", *J. Mater. Chem. A* **2017,** *5*, 15891.
1. **Liang, Zhiming,** Graham, Kenneth R. "Surface Modification of Silver Nanowires for Morphology and Processing Control in Composite Transparent Electrodes", ACS *Appl. Mater. Interfaces* **2015,** *7*, 21652.